Title
HIGH TEMPERATURE OXIDATION OF NICLEK-COBALT ALLOYS

Author
Hou, P.Y.

Publication Date
1983-03-01

Lawrence Berkeley Laboratory
UNIVERSITY OF CALIFORNIA

Materials & Molecular Research Division

HIGH TEMPERATURE OXIDATION OF NICKEL-COBALT ALLOYS

P.Y. Hou
(M.S. Thesis)

March 1983

Prepared for the U.S. Department of Energy under Contract DE-AC03-76SF00098

DISCLAIMER

LBL-16616

HIGH TEMPERATURE OXIDATION OF NICKEL-COBALT ALLOYS

Peggy Y. Hou

M.S. Thesis

March 1983

Materials and Molecular Research Division
Lawrence Berkeley Laboratory
University of California
Berkeley, CA 94720

This work was supported by the Director, Office of Energy Research, Office of Basic Energy Sciences, Materials Sciences Division of the U.S. Department of Energy under contract Number DE-AC03-76SF00098.

HIGH TEMPERATURE OXIDATION OF NICKEL-COBALT ALLOYS

Master of Science in Engineering Science | *Peggy Y. Hou* | Materials Science and Mineral Engineering

Alan W. Searcy
Chairman of Committee

ABSTRACT

The oxidation of Ni-Co alloys under two extremes of oxygen potentials at 1000°C is studied. In both cases, an external solid solution oxide scale is formed with extensive internal oxide formation in alloys oxidized under the low oxygen potential. Selective oxidation of the metal with the more stable oxide, CoO, is observed when the ambient oxidizing potential is low, and as a consequence, the oxidation rate constant increases according to the degree of selective oxidation. The growth of the external oxide scale is described using Wagner's ternary diffusion model. A more refined defect model, which includes the presence of all types of vacancy species within the scales, is adapted to obtain the diffusivities of cations in the scales as a function of oxygen potential and cation composition. In addition, correlation effects between elementary jumps of the cations are included to account for additional compositional dependence of the diffusivities. Theoretical calculations on the oxidation rate constants and the cation concentration profiles are compared with experimentally measured data.

ACKNOWLEDGEMENT

I would like to express my deepest gratitude to late Professor David P. Whittle for the support, guidance and the abundant understandings and good humor he offered througout most part of this work. I am also very grateful to Dr. John Stringer for his enlightening suggestions and guidance during the past six months, which made completion of this work much smoother.

I would also like to thank Professors Alan Searcy and Leo Brewer for reading and correcting this manuscript. I am especially thankful to Professor Searcy for the many helps he offered since Professor Whittle's death.

Special thanks are also due to my colleagues in our research group especially to Dr. Haroun Hindam, Dr. Stephen Smith and Mr. Frank Yang for their continuing support and helpful discussions, and to Mr. Han-Chuan Lung for many useful suggestions on computer programing.

Many thanks to the wonderful group of supporting staffs in building 62. Their expertise and friendlyness have made working here a pleasant experience.

Finally, I want to acknowledge the love and encouragement given to me by my parents and especially by my husband. Their love through out these years has always been my greatest support.

This work was supported by the Director, Office of Energy Research, Office of Basic Energy Sciences, Materials Sciences Division of the U.S. Department of Energy under Contract Number DE-AC03-76SF00098.

CONTENTS

I. INTRODUCTION

In its most general sense, the high temperature oxidation of a metal, or an alloy means its reaction with constituents of its gaseous environment: these can include not only oxygen, but also nitrogen, sulphur, carbon, chlorine, etc. Over the past 10-20 years, the field of alloy oxidation has widened considerably. The various monographs,[1-4] review articles[5-8] and recent conference proceedings[9-11] provide much of the detailed observations of alloy oxidation behavior. The oxidation mechanisms usually become increasingly complicated as more alloying constituents are considered, or as the oxidizing environment changes from a single oxidant to a mixed-gas environment. Although oxidation behavior in mixed-gas environments has been studied extensively in recent years, especially in coal conversion atmospheres,[12-14] the alloy systems that have been investigated have been principally limited to two or three components. These binary and ternary alloy systems are either the basis of many commercial high temperature materials, (e.g. Fe-Cr-Ni, Co-Cr) or they may represent an idealized system (e.g. Ni-Co, Pt-Ni) where quantitative studies on oxidation phenomena can be made.

The oxidation process of an alloy can generally be divided into three stages as shown in figure 1. Upon initial exposure of the alloy, the oxides of essentially every reactive component are formed in a proportion given by the composition of the bulk alloy.[15] Oxide nuclei with high intrinsic growth rates overgrow the nuclei of the slower growing oxides. The rapid kinetics of the overgrowth formation contribute to a relatively high initial rate of oxidation. While the overgrowth is forming, the underlying nuclei of the slower growing, and usually more stable, oxide grow laterally. Eventually, they may impinge and form a continuous layer, or may remain as isolated precipitates in the faster growing matrix. This depends on the various factors which determine the steady state

scale configuration.

Eventually, the transient oxidation period gives way to a steady state, which means that the morphology in the scale is independent of time. Generally, the overall oxidation rate is governed by the transport of one or more species through a particular layer in the scale and as a consequence will approximate to a parabolic rate law. Any oxidation-resistant alloy depends on this period for continued protection. It cannot last indefinitely, since ususlly selective removal of one of the alloy components takes place, and the period must end when that component has been totally removed from the alloy. Quite often, the end of the steady state period occurs before all the selectively removed element has been consumed, by some kind of mechanical disruption of the oxide scale. Then, because the underlying alloy is a different composition than originally, it does not regain its steady state oxide. The final breakdown is often related to mechanical influences such as scale adherence, void formation, thermal or mechanical stresses etc. Usually, the more severe the oxidation condition, such as a higher temperature, a rapid temperature cycle, simultaneous mechanical stress or erosion, and so on, the shorter the steady state period becomes.

The scale morphology during the steady state is determined by a complex interplay of thermodynamic and kinetic factors. The various morphologies that can form when a binary alloy is oxidized in a single oxidant gas has been classified recently by Bastow et al.[16] Basically, there are four types of binary alloy-oxygen systems:

(a) Only one stable oxide (noble metal alloys),

(b) Complete miscibility between the two oxides,

(c) Partial miscibility between the two oxides,

(d) Partial miscibility between the two oxides and formation of an additional compound oxide or oxides.

(a) and (b) represent, of course, somewhat simplified systems, but are important limiting cases: firstly, because they can be analyzed quantitatively and secondly, because many aspects of the more complex systems (c) and (d) approximate to (a) and (b) under limiting conditions.

A schematic arrangement of the different types of scales which can be produced for the simple system (b) is given in figure 2 where B is taken to be the thermodynamically more oxidizable or less noble component. Although A(X) and B(X) are completely miscible, virtually pure A(X) and B(X) scales can form on A-rich or B-rich alloys, respectively. The essential purity of the scales depends on the relative oxidation potentials of A and B and the dilution of the minor component in the A-B alloy (as in cases 1 and 3 in figure 2). Case 4 represents internal oxidation while the ambient oxidant partial pressure is lower than the dissociation pressure of the oxides, and the internal oxide formed are (A,B)X type solid solution particles.[17]

Apart from cases 1,3 and 4 discussed in the previous paragraph, case 2 in figure 2 represent the most general type within this system where both components A and B are oxidized, producing a solid solution external scale. The relative proportions of the two components in the scale are determined by the oxidation potentials of A and B and their diffusion rates in the alloy and scale. A general treatment of scale growth of these conditions has been provided by Wagner[18] who pointed out that, unless the diffusivities of A and B cations are equal, their concentration will vary across the scale, the distribution of A and B depending on their relative diffusivities. Two limiting cases can be identified, which correspond to minimum and maximum values of the scale growth rate.

(In the example used, B, the more easily oxidizable component is also the faster diffusing cation in the scale, and as a consequence, increase in the concentration of B in the scale causes faster scaling rates; the opposite situation would exist when the more easily oxidizable element was the slower diffusing cation).

(1) When diffusion in the alloy is very slow in comparison with that in the scale, the overall ratio of A to B in the scale can be shown identical with that in the alloy.[19] As a consequence, there is no selective oxidation, and the differing tendencies of the alloy components to oxidize, as expressed by $\delta(\Delta G)$ ($=\Delta G^{\circ}_{AO} - \Delta G^{\circ}_{BO} > 0$, since component B forms the more stable oxide), has negligible influence on the composition of the scale, or its growth rate.

(2) When diffusion in the alloy is much faster than in the oxide, the composition of the oxide, and hence the oxidation rate, is controlled by the degree of selective oxidation, $\delta(\Delta G)$.

Intermediate values of the ratio of diffusivities correspond to intermediate degrees of selective oxidation and rates of oxidation. Corresponding concentration profiles through binary alloys of Fe-Mn[20] and Ni-Co,[21] oxidized under most conditions of temperature and oxygen pressure, fall into this category of forming (A,B)X type external scale under case 2a (Fig. 2). The unusual dependence of cation diffusivities on oxidant activities in case 2c have been shown by Mayer and Smeltzer[22] with Co-10%Fe alloys oxidized at oxygen potentials greater than 10^{-2} atmosphere. The diffusivity of Fe^{2+} ions in the (CoFe)O was found greater than that of Co^{2+} ions at low oxygen potentials, but lower at higher oxygen potentials.

The steady state growth of these (A,B)X type of solid solution scales through the transport mechanism of cation outward diffusion has been treated quantitatively by Wagner.[18] There have been a number of recent analyses of the oxidation of this kind of alloy system using this ternary diffusion model put

forward by Wagner, and subsequently modified by Dalvi and Coates[23] and Bastow, Whittle and Wood.[24] The growth rate of the solid solution scale depends primarily on the distribution of the two cations through the scale and on the oxygen activity profile. These are calculated from Wagner's transport equations,* which in turn allows calculation of the parabolic growth rate of the scale.

A complete solution of the cation concentration profile in the scale and the rate constant k, would involve several necessary auxiliary equations and the knowledge of many diffusion properties and thermodynamic relationships. Such a calculation is a tremendous task even with the help of modern computers. Consequently, analyses have been focused on special cases which permit introduction of appropriate simplifications.

A very suitable system is Ni-Co-O at 1000° C. Nickel and cobalt are adjacent transition metals in the periodic table and have nearly equal ionic radii in corresponding valence states.[25] This fact together with the fact that NiO and CoO have almost equal free energies of formation at 1000°C[26,27] (with ΔG_f^o for CoO ~ 6 kcal/mole lower) gives rise to their observed mutual solubility across the entire phase diagram. In addition, there is indirect evidence that the solid solution, (Ni,Co)O, exhibits ideal behavior. The position of the phase boundary between the (Ni,Co)O solid solution and the two phase field (solid solution + Co_3O_4) is consistant with approximately ideal behavior,[28] and a comparison of tracer and interdiffusion data in mixed oxides shows that the thermodynamic factor $(1+\partial \ln \gamma_i / \partial N_i)$ in the Darken equation is close to unity.[29,30]

The monoxides of nickel and cobalt exhibit the rocksalt (NaCl) stucture[31] in which the oxygen ions are cubic close-packed and the cations occupy the octehedral holes. Both CoO and NiO are metal-deficient at high temperatures and in a wide range of oxygen partial pressures,[32] and the metal deficiency is

*These equations will be discussed in detail in section II.

equivalent to the formation of cation vacancy type defects. Near the metal-oxide decomposition pressure the oxides are approximately stoichiometric, while at higher partial pressures of oxygen the concentration of vacancy type defects increases. The concentration of the predominating point defects are 10-100 times smaller in NiO than in CoO. Chen and Peterson[33] have shown that addition of CoO to NiO increases the deviation from stoichiometry and consequently enhances cation diffusivities in the solid solution, (Ni,Co)O, since cation self-diffusion takes place by a vacancy mechanism in both CoO and NiO,[34-37] and the oxide scale grows by the outward movement of cations and electons.

In order to apply Wagner's analysis to practical situations similar to the Ni-Co system, a knowledge of the variation of the self diffusion coefficients of the two cations through the scale is required. Earlier investigators[38-42] have found it necessary to use data from the oxidation experiments themselves in order to establish the boundary conditions for the calculation of the theoretical cation profiles, and as a consequence, the agreement between theoretical and experimental profiles arises partly because the boundary conditions are the same. More recently, completely independently determined diffusion data and boundary conditions have been used in similar calculations[43-46] to substantiate the model. However, in the one case[43,44] these were still based on a relatively simple defect model for the oxide solid solution, while in the other[45,46] empirically based relationships were used.

There is now mounting evidence[32] especially when a wide range of oxygen potentials is considered (as in scale growth) that a simple oxide defect model, in which essentially only one type of defect predominates, is not only unjustified, but is likely to produce nontrivial errors in any calculations of transport properties. Recently, Whittle et al.[47] proposed a more refined defect model in which the concentrations of cation vacancies with all possible effective

charges in the nonstoichiometric oxides can be evaluated. This approach in turn allows for the calculation of the total cation vacancy concentrations in the scale as a function of oxygen potentials and composition. One of the purpose of this work, then, is to provide a more complete description of Wagner's original theory by including this more refined treatment of the real defect structure of the oxide solution growing on a binary alloy. Ni-Co alloys are used for the analysis because they are relatively simple systems, as described earlier. Theoretical calculations are concentrated on these alloys oxidized under high oxygen potentials where conditions are most suited for Wagner's theory. In addition, an attempt to view the applicability of the theory on alloys oxidized under low oxidizing atmospheres is also made.

Another objective of this work is to investigate the general oxidation behavior of Ni-Co alloys under a low oxygen potential (near their oxide dissociation pressures). Ni-Co alloys oxidized near 1 atm. O_2 approximate to the first limiting case discussed earlier in this section, where diffusion in the scale is much faster than that in the alloy so that the composition of the two components in the scale and in the alloy is about the same. However, as the ambient oxygen potential decreases, the degree of nonstoichiometry of the oxides also decreases, and as a consequence, diffusivities of the cations in the scale are reduced and the system may start to approach the second limiting case. Under these conditions, selective oxidation of the more stable oxide, CoO, may occur. The degree of such occurence with different Co content in the alloy, and the effect of this selective oxidation on the oxidation rate constants are examined.

II. THEORETICAL ANALYSIS

The basis for the theoretical work presented here is the ternary diffusion model first put forward by Wagner.[18] The approach for analysis is to use completely independently determined diffusion and thermodynamic data rather than to use data obtained from oxidation experiments in order to establish boundary conditions. Such an approach provides a more rigorous test to the model and has been adapted by Whittle et al.[43,44] However, in these previous works, a somewhat simplified defect model was used in order to calculate the cation diffusivities in the scale. The compositional and oxygen activity dependencies of the diffusivities were arbitrarily assigned functional forms, and only one type of defect structure with an average effective charge was assumed.

Recently, a somewhat more complete defect model was proposed by Whittle et al.[47] The model allows the concentration of cation vacancies with all possible effective charges to be determined. As a consequence, the total vacancy concentration in the scale can be calculated for any oxygen activity and cation composition. The present analysis makes use of this defect model to obtain cation diffusivities as a function of composition and oxygen activity. Furthermore, correlation effects between elementary jumps of the cations are considered using Dieckmann and Schmalzried's[48] analysis to correct, to a certain extent, for the fact that the ratio of cation diffusivities is also a function of composition.

Only the basis and development of the theoretical analysis are discussed in this section. Results of the analysis which include the cation concentration profile, the oxidation rate constant and the total vacancy concentration profile will be presented later.

List of Principal Symbols

a_i	activity of component i.
D_{all}	interdiffusion coefficient in the alloy.
D_A, D_B	self diffusion coefficients of A and B cations respectively in the scale.
D_i^T	tracer diffusivity of component i in the scale.
f_i	correlation factor of component i.
f_o	correlation factor for vacancy diffusion for a pure oxide of the rock salt B1 structure.
j_i	diffusion flux of component i in the scale.
k	parabolic rate constant in terms of scale thickness.
K_i^j	equilibrium constant for the formation of i type of vacancy in j type of oxide.
N_A, N_B	mole fractions of A and B respectively in the alloy.
N_B^o	mole fraction of B in the bulk alloy.
p	ratio of cation diffusivities in the scale.
R	gas constant.
t	time.
T	absolute temperature, K.
u	distance measured from the initial surface of the alloy.
V_{all}	molar volume of the alloy.
V_{eq}	volume per equivalent in the scale.
V_m	molar volume of the scale.
x	distance measured from the alloy-scale interface.
x_s	total thickness of the scale at time t.
y	dimensionless variable of distance in the scale($= x/x_s$).
z_i	absolute valence of ion i.
$[V^z]$	concentration of vacancies with effective charge z.
$[h\cdot]$	concentration of electron holes in the scale.
α	parabolic rate constant in terms of recession of the alloy surface.
Γ_i	elementary jump frequency of component i.
ΔG_i^o	free energy of formation of component i.
λ	parametric variable of distance in the alloy ($= u/t^{1/2}$).
λ_s	value of λ at the alloy-scale interface.
ξ	equivalent fraction of compound B(X) in the scale.
ξ_{all}	equivalent fraction of element B in the bulk alloy.
ξ_{av}	average equivalent fraction of B(X) in the scale.

A. Diffusion Processes in the Alloy and Scale

The following general description assumes that diffusion control is maintained at all stages of scale growth. The nucleation of a uniform layer of the stable oxide across the whole alloy surface is assumed to be instantaneous. The oxide is assumed to be a semi-conducting one. Scale grows solely by outward cation diffusion and that the oxidant does not diffuse into the underlying alloy.

Local thermodynamic equilibrium is supposed to prevail so interface concentrations are assumed to take their equilibrium value.

Following Wagner,[18] a system is considered in which an initially homogeneous binary alloy, A-B, is oxidized by a single oxidant, in this case, oxygen, and a single phase scale consisting of a solid-solution of the compounds A(O) and B(O) is formed. The diffusion profiles which develope in the alloy and scale, $N_B(\lambda)$ and $\xi(y)$ respectively, are shown schematically in figure 3, where N_B is the mole fraction of B in the alloy and ξ is the equivalent fraction of compound B(O) in the scale, together with the associated profile for the activity of the oxidant, $a_O(y)$, and the coordinate systems used in the description of the diffusion processes. The coordinate frames of u and λ have their origins at the original alloy surface and $\lambda = u/t^{1/2}$. The frames of x and y have their origins at the alloy-scale interface and $y = x/x_s$, where x_s is the instantaneous thickness of the scale. The use of the parametric coordinates λ and y results in profiles which are invariant with time t.

(i) *Diffusion in the scale*

The diffusion flux of cation B, j_B, through the solid solution scale is given, in equivalents per unit area per unit time by

$$j_B = -\frac{D_B \xi}{V_{eq}} \frac{\partial \ln a_B}{\partial x} \qquad (1)$$

where D_B is the self diffusivity of cation B in the scale, a_B is the activity of cation B and V_{eq} is the equivalent volume of the solid solution, and it is assumed to be independent of composition. When writing a_B in terms of the activities of the oxidant, a_O, and the compound BO, a_{BO},

$$j_B = -\frac{D_B \xi}{V_{eq}} \left(\frac{\partial \ln a_{BO}}{\partial \xi} \frac{\partial \xi}{\partial x} - \frac{z_B}{z_O} \frac{\partial \ln a_O}{\partial x} \right) \qquad (2)$$

where z_B and z_O are valencies of B and O respectively. By combining equation

(2) with the equivalent expression for the flux of A cations, j_A, in a relation describing the rate of thickening of the scale, dx_s / dt

$$(j_A + j_B) V_{eq} = \frac{dx_s}{dt} = \frac{k}{x_s} = \left(\frac{k}{2t}\right)^{1/2} \tag{3}$$

where k is the parabolic rate constant. It has been shown that

$$D_A(1-\xi)\left[\frac{-\partial \ln a_{AO}}{\partial \xi}\frac{d\xi}{dy} + \frac{z_A}{z_O}\frac{d\ln a_O}{dy}\right] + D_B\xi\left[\frac{-\partial \ln a_{BO}}{\partial \xi}\frac{d\xi}{dy} + \frac{z_B}{z_O}\frac{d\ln a_O}{dy}\right] = k \tag{4}$$

which is the first transport equation governing scale growth proposed by Wagner.[18] The second equation, which is essentially a mass balance equation for one of the components (B), reads

$$yk\frac{d\xi}{dy} = \frac{-d}{dy}\left[D_B\xi\left[\frac{\partial \ln a_{BO}}{\partial \xi}\frac{d\xi}{dy} - \frac{z_B}{z_O}\frac{d\ln a_O}{dy}\right]\right] \tag{5}$$

When systems like NiO-CoO are considered, whose oxide solutions have the simple cubic NaCl structure on which $z_A = z_B = z_O$ and in which the pseudo-binary oxide solution approximates to ideal thermodynamic behavior, $\partial(\ln a_{AO})/\partial\xi$ and $\partial(\ln a_{BO})/\partial\xi$ can be replaced by $-1/(1-\xi)$ and $1/\xi$ respectively. Thus, equation (4) becomes

$$k = (D_A - D_B)\frac{d\xi}{dy} + [D_A(1-\xi) + D_B\xi]\frac{d\ln a_O}{dy} \tag{6}$$

and equation (5) simplifies to

$$yk\frac{d\xi}{dy} = \frac{-d}{dy}\left[D_B\left[\frac{d\xi}{dy} - \xi\frac{d\ln a_O}{dy}\right]\right] \tag{7}$$

These equations contain the self-diffusion coefficients of the two cations D_A and D_B which are in general, a function of both the oxygen activity and the oxide composition. The form of the dependence is closely related to the type of defect structure present in the oxide, and it may be shown[47] that the form assumed for this function by authors who have solved these equations previ-

ously[38-44] is essentially valid if only a single type of defect predominates in the oxide solution. However, it is becoming increasingly clear (see, for example, Kofstad[32]), that one type of metal vacancy may dominate at high partial pressures of oxygen, while another type dominates at low values of P_{O_2}. For example, Fisher and Tannhauser[49] had found that the cation vacancies in CoO were singly charged tending to a doubly charged state at pressures approaching the oxide dissociation pressure. Since the oxide activity through the scale varies over a wide range, from the dissociation pressure of the oxide at the inner oxide-alloy interface to the ambient oxygen pressure ($\sim 10^{-7}$ - 1 for oxidation of Ni-Co alloys at 1000°C in 1 atmosphere oxygen, for example), the simple approximation of only a single type of defect is not adequate. A proposed, more adequate solution of the diffusion coefficients is discussed later in this section.

(ii) *Diffusion in the alloy*

During the oxidation process, a depletion zone of component B is established in the alloy, as shown in figure 3, because it is assumed that B is preferentially oxidized. The distribution of B in the zone is described by Fick's second law applied to a semi-infinite system

$$\frac{d}{d\lambda}\left[D_{all}\frac{dN_B}{d\lambda}\right] + \frac{\lambda}{2}\frac{dN_B}{d\lambda} = 0 \; ; \quad \lambda > \frac{u_s}{t^{1/2}} = (2\alpha)^{1/2} \tag{8}$$

where D_{all} is the interdiffusion coefficient in the alloy and α is a parabolic rate constant describing the recession of the alloy-scale interface,[24] $\alpha = u_s \, du_s / dt$. Hence α is related to k

$$\left[\frac{\alpha}{k}\right]^{1/2} = \frac{du_s}{dx_s} = \frac{V_{all}}{V_{aq}}\left[\frac{(1-\xi)}{z_A} + \frac{\xi_{av}}{z_B}\right] \tag{9}$$

where V_{all} is the molar volume of the alloy and ξ_{av} is the average equivalent fraction of BO in the scale. When $z_A = z_B = 2$ as in the NiO-CoO system, and if V_m is the molar volume of the solid solution, then $V_m = z_B V_{eq}$, and equation (9)

becomes

$$\left(\frac{\alpha}{k}\right)^{1/2} = \frac{V_{all}}{V_m} \qquad (10)$$

The equation describing diffusion in the alloy (eqn. 8) can be neglected if the depletion zone of B in the alloy is very narrow.[24] Otherwise, simutaneous solution of equations (6), (7) and (8) will be necessary. These relationships will be described in more detail when the solution of the diffusion equations are presented.

B. Diffusion Coefficients in Oxide Solid Solutions

Initially, it is appropriate to re-consider the assumption made in previous solutions to these equations, namely that the ratio of self-diffusion coefficients of cations A and B in the oxide solution is a constant independent of a_O and ξ. Young et al.[45] and Narita et al.[46] in recent calculations of the concentration profiles in growing (CoFe)S scales and (CoFe)O and (CoNi)O scales respectively, removed this restriction. However, they used empirical relationships for the dependence of D_A/D_B on composition. Dieckmann and Schmalzried[48] have pointed out that correlation effects between the elementary jumps occur, which make the ratio D_A/D_B dependent on the composition of the oxide solution.

According to Dieckmann and Schmalzried,[48] correlation effects are found if the elementary jump frequencies Γ_A of an A-cation into a neighboring vacancy differs from the corresponding jump frequency for a B-cation, Γ_B. Corrections can be taken into account by defining an effective jump frequency ,Γ_{eff}, to determine the cation diffusivity, and which differs from Γ_i (i=A or B) by a correlation factor which is concentration dependent. Accordingly, the self-diffusion coefficients in an oxide solution (AB)O are written as

$$D_A = \frac{2\Gamma_A f_A a^2[V]}{f_o} \quad \text{and} \quad D_B = \frac{2\Gamma_B f_B a^2[V]}{f_o} \qquad (11)$$

where Γ_i and f_i are the elementary jump frequencies and correlation factors respectively; f_o(=0.782), the correlation factor for vacancy diffusion for a pure oxide of the rock salt B1 structure;[50] a, the elementary jump distance; and [V], the atomic fraction of vacant sites. The concentration dependence of the correlation factors may be found[48] from either

$$f_A = 1-\frac{0.218}{(1-\xi)+\xi(D_B/D_A)} \; ; \quad f_B = 1-\frac{0.218}{(1-\xi)(D_A/D_B)+\xi} \tag{12}$$

or

$$f_A^2+f_A\frac{0.218-(1-\xi)-\eta_A}{(1-\xi)}+\frac{0.782\eta_A}{(1-\xi)} = 0 \; ; \quad \eta_A = \frac{\Gamma_B/\Gamma_A}{(\Gamma_B/\Gamma_A)-1} \tag{13a}$$

$$f_B^2+f_B\frac{0.218-\xi-\eta_B}{\xi}+\frac{0.782\eta_B}{\xi} = 0 \; ; \quad \eta_B = \frac{\Gamma_A/\Gamma_B}{(\Gamma_A/\Gamma_B)-1} \tag{13b}$$

According to experimental determinations of the tracer diffusivities of both Co and Ni ions in (Co,Ni)O between 1100 and 1550°C, at P_{O_2} = 0.21 atmos. by Chen and Peterson[29] and calculations by Dieckmann and Schmalzried,[48] when these correlation factors are taken into account, the ratio of elementary jump frequencies, Γ_{Co}/Γ_{Ni}, varies by only 8% over the entire composition range, as opposed to a variation of about 16% in D_{Co}/D_{Ni}. Hence it seems more appropriate to consider Γ_{Co}/Γ_{Ni} as a constant and use eqns.(13) and (11) to find diffusivities as a function of composition. This correction should only refine the theoretical calculations slightly since there is still 8% variation in the elementary jump frequencies ratio.

In addition to the concentration dependence of the cation diffusivities through the correlation factors, [V] also depends strongly on oxide composition and oxygen activity. As discussed by Whittle et al.,[47] vacancies of different effective charges are now considered to exist in these types of non-stoichiometric oxides, with the relative proportions of each depending on oxide composition and oxygen activity. All the vacancies contribute towards the

diffusivity and thus [V] in eqn.(11) really represents $\sum[V^z]$, the sum of the concentrations of the vacancies carrying effective charges z=0,1,and 2. As given by Whittle et al.,[47] the atomic fractions of the various effectively charged vacancies can be expressed by

$$[V^x] = (K_{V^x}^{AO})^{(1-\xi)}(K_{V^x}^{BO})^{\xi} a_O \tag{14a}$$

$$[V^{\cdot}] = (K_{V^x}^{AO}K_{V^{\cdot}}^{AO})^{(1-\xi)}(K_{V^x}^{BO}K_{V^{\cdot}}^{BO})^{\xi} \frac{a_O}{[h^{\cdot}]} \tag{14b}$$

$$[V^{''}] = (K_{V^x}^{AO}K_{V^{\cdot}}^{AO}K_{V^{''}}^{AO})^{(1-\xi)}(K_{V^x}^{BO}K_{V^{\cdot}}^{BO}K_{V^{''}}^{BO})^{\xi} \frac{a_O}{[h^{\cdot}]^2} \tag{14c}$$

where K_i^j (i=V^x, $V^{\cdot}$,$V^{''}$; j=AO,BO) are the equilibrium constants for formation of the three types of vacancies according to

$$\frac{1}{2}O_2 = O_O^x + V^x \;\; ; \quad V^x = V^{\cdot} + h^{\cdot} \;\; ; \quad V^{\cdot} = V^{''} + h^{\cdot} \tag{15}$$

in the two pure oxides, where V^x, $V^{\cdot}$ and $V^{''}$ represent vacancy lattice sites in the cation sub-lattice. The equilibrium constants are related to the free energies of formation of the defects in the two pure oxides by

$$(\Delta G^o)_i^j = -RT\ln K_i^j \;\; , \quad i = V^x, V^{\cdot}, V^{''} ; \quad j = AO, BO \tag{16}$$

The concentration of electron holes, $[h^{\cdot}]$, is assumed to be much larger than that of n-type electronic defects, and is given by the simplified electroneutrality condition:

$$[h^{\cdot}] = (K_{V^x}^{AO}K_{V^{\cdot}}^{AO})^{(1-\xi)}(K_{V^x}^{BO}K_{V^{\cdot}}^{BO})^{\xi} \frac{a_O}{[h^{\cdot}]} + 2(K_{V^x}^{AO}K_{V^{\cdot}}^{AO}K_{V^{''}}^{AO})^{(1-\xi)}(K_{V^x}^{BO}K_{V^{\cdot}}^{BO}K_{V^{''}}^{BO})^{\xi} \frac{a_O}{[h^{\cdot}]^2} \tag{17}$$

Through solution of eqns.(14) and (17), [V] is given as a function of a_O and ξ, and together with solution of eqn.(13), can be substituted into eqn.(11) to give D_A and D_B as a function of ξ and a_O.

C. Solution of the Diffusion Equations

The Ni-Co system falls in the category of A-B binary alloys where component B is removed selectively from the alloy during oxidation and is also the faster diffusing cation in the scale. For an alloy of bulk composition N_B^o, ξ_{av} depends on both the relative diffusion rates in the alloy and scale and the degree of selective oxidation of B. By using D_B to represent the cation diffusion rate in the scale, the minimum value ($\xi_{av}^{min} = N_B^o$) occurs when $D_{all}/D_B \to 0$ and the maximum value ($N_B^o < \xi_{av}^{max} < 1$) is attained when alloy diffusion is infinitely fast, $D_{all}/D_B \approx \infty$.

Ni-Co alloys oxidized under 1 atm O_2 approach the first limiting case, and diffusion in the alloy can be neglected. Solution of the diffusion equations only involves equations (6) and (7). Substituting for $d\ \ln a_O/\ dy$ from eqn.(6) into eqn.(7) and using $p = D_A/D_B$ where according to eqn.(11)

$$p = \frac{f_A \Gamma_A}{f_B \Gamma_B} \tag{18}$$

and is a function of composition through the term f_A/f_B, gives, after differentiation

$$\frac{d^2\xi}{dy^2} p D_B [p-(p-1)\xi] + \frac{d\xi}{dy}\left\{ yk[p-(p-1)\xi]^2 - pk \right. \tag{19}$$
$$\left. + p[p-(p-1)\xi]\frac{dD_B}{dy} + \frac{dp}{dy}[D_B\xi + k\xi(1-\xi)] \right\} + (\frac{d\xi}{dy})^2 D_B p\,(p-1) = 0$$

Using the relationships that

$$D_B = D_B(\xi, a_O) \quad \text{and} \quad p = p(\xi) \tag{20}$$

then gives

$$\frac{d^2\xi}{dy^2}[p-(p-1)\xi] + \frac{d\xi}{dy}\frac{k}{D_B}\left\{ \frac{y}{p}[p-(p-1)\xi]^2 - 1 + \frac{\partial \ln D_B}{\partial \ln a_O} \right\} \tag{21}$$
$$+ (\frac{d\xi}{dy})^2 \left\{ [p-(p-1)\xi]\frac{\partial \ln D_B}{\partial \xi} + (p-1)(1 - \frac{\partial \ln D_B}{\partial \ln a_O}) + \frac{d\ln p}{d\ln \xi}[1 + \frac{k}{D_B}(1-\xi)] \right\} = 0$$

Using the same nomenclature, eqn.(6) becomes

$$\frac{k}{D_B} = (p-1)\frac{d\xi}{dy} + [p(1-\xi)+\xi]\frac{d\ln a_O}{dy} \qquad (22)$$

Eqns.(21) and (22) are solved numerically using finite difference method, with f_A, f_B and [V] obtained from eqns.(13), (14) and (17), and hence D_B and $\partial\ln p/\partial\ln\xi$ can be obtained from eqns.(11) and (18) respectively. $\partial\ln D_B/\partial\ln\xi$ and $\partial\ln D_B/\partial\ln a_O$ are obtained assuming linear variation within one steplength of the finite difference forms of equations (21) and (22).

Additional relationships are required for the solution, as detailed in Wagner's paper.[18] These include a mass balance at the scale-gas interface:

$$y = 1 \ , \qquad \frac{k}{D_B} = p\left[\frac{d\xi}{dy}\right]\frac{1}{(p-1)(\xi-1)\xi} \qquad (23)$$

where the values of the variable p, $d\xi/dy$, D_B and ξ are those pertaining to y=1. At the inner alloy-scale interface, because the interdiffusion coefficient in the alloy is very much smaller than the growth rate of the scale, the composition of the scale at y=0 is given by[19]

$$y = 0 \ , \qquad \xi = \frac{p\,\xi_{all}}{1+\xi_{all}(p-1)} \qquad (24)$$

where again ξ and p refer to values at y=0, and ξ_{all} is the equivalent fraction of element B in the bulk alloy. The oxygen activity at y=0 is directly related to the oxide composition there, since thermodynamic equilibrium is assumed. Thus

$$y = 0 \ , \qquad a_O = (1-\xi)\exp\left[\frac{\Delta G^{\circ}_{AO}}{RT}\right] + \xi\exp\left[\frac{\Delta G^{\circ}_{BO}}{RT}\right] \qquad (25)$$

where ΔG°_{AO} and ΔG°_{BO} are the standard free energies of formation of AO and BO respectively.

The numerical technique for solution is initiated by trial values of the rate constant k and the composition of the oxide at y=1, and the equations integrated inward to y=0, the procedure being repeated using continuously

better estimates of k and $\xi_{y=1}$ until the calculated and actual values of $\xi_{y=0}$ (from eqn.(24)) and $a_{O,y=0}$ (from eqn.(25)) are within 1 and 5% respectively. The step length, Δy, in the finite difference forms of eqns.(21) and (22) is reduced until the result is independent of the step length; it is also independent of the initial estimates.

When oxidation of Ni-Co alloys are carried out under very low oxygen activities, the diffusivities in the scales are markedly reduced, and the system no longer approximates to the limiting case where $\xi_{av} \approx N_B^o$. Diffusion in the alloy needs to be considered and equations (6), (7) and (8) are solved simutaneously.

The solution of equation(8) describing diffusion from the bulk alloy towards the alloy-scale interface is given by

$$N_B = N'_B+(N_B^o-N'_B)\frac{erf\,(\lambda/2D_{all}^{\frac{1}{2}})-erf\,(\lambda_s/2D_{all}^{\frac{1}{2}})}{erfc\,(\lambda_s/2D_{all}^{\frac{1}{2}})} \qquad (26)$$

while assuming D_{all} being independent of composition. N_B is the mole fraction of B in the alloy, the single prime ' refers to values at the alloy-scale interface, and λ_s is the value of λ at the alloy-scale interface. According to equations (8) and (10)

$$\lambda_s = \sqrt{2k}\left[\frac{V_{all}}{V_m}\right] \qquad (27)$$

for the Ni-Co system.

Solutions for the transport equations in the scales (eqns.(6) and (7)) are the same as described previously. However, the boundary condition for the value of ξ at the scale-alloy interface can no longer be deduced from eqn.(24). The relationship between $\xi_{y=0}$ and $N_{B,y=0}$ are given as

$$\xi' = \frac{N'_B\gamma}{1-N'_B(1-\gamma)} \qquad (28a)$$

$$\gamma = \exp[(\Delta G^{o}_{AO} - \Delta G^{o}_{BO})/RT] \qquad (28b)$$

since thermodynamic equilibrium is assumed and the alloy is also considered to approximate to an ideal solution. The oxygen activity at y=0 is still satisfied by eqn.(25), and the mass balance equation at the scale-gas interface (eqn.(23)) also holds.

A new boundary condition is introduced by equating the relative amount of B depleted in the alloy to the relative amount of B enriched in the scale. This additional boundary condition, together with eqns.(23),(25) and (28), the bulk alloy concentraton, N^{o}_{B}, and the oxygen activity of the oxidizing atmosphere, a_O at y=1, enable eqns.(6),(7) and (8) to be solved.

As before, the numerical technique for solution is initiated by trial values of the rate constant k and the composition of the oxide at y=1, and eqn.(6) and (7) are integrated inward to y=0. Once $\xi_{y=0}$ is obtained, N'_B can be acquired from eqn.(28) and diffusion profiles in the alloy can be calculated using eqn.(26). At this point, the amount of depletion of B in the alloy and the amount of enrichment of B in the scale can be computed through integrating the diffusion profiles. The two relative amounts are compared as well as the computer calculated a'_O and the a'_O obtained from eqn.(25). The procedure is repeated until these values agree within 2 and 5% respectively, using better estimates of k and $\xi_{y=1}$.

D. Data for the NiO-CoO System

Equilibrium constants for the formation of the different ionic defects in CoO have been measured by a number of authors and summarized by Dieckmann.[51]

$$K^{CoO}_{V^{2}} = 1.6\times10^{-2}\exp[-26000(J/mole)/RT] \qquad (29a)$$

$$K^{CoO}_{V} = 2.4\exp[-51000(J/mole)/RT] \qquad (29b)$$

$$K_{V''}^{CoO} = 0.17\exp[-72000(J/mole)/RT] \qquad (29c)$$

Corresponding values from experimental measurements for NiO are not available. Theoretical estimations of these equilibrium constants calculated by Osburn and Vest[52] using a conduction band model for the pre-exponential terms and a hydrogen atom model for the ionization energies give

$$K_{V''}^{NiO} = 5.43\times10^{11}T^{-3}\exp[-187544(J/mole)/RT] \qquad (30a)$$

$$K_{V}^{NiO} = 1.61\times10^{-7}T^{3/2}\exp[-9260(J/mole)/RT] \qquad (30b)$$

$$K_{V''}^{NiO} = 4.03\times10^{-8}T^{3/2}\exp[-36998(J/mole)/RT] \qquad (30c)$$

Chen and Peterson[29] have measured tracer diffusion coefficients in CoO, NiO and in some oxide solutions, (Ni,Co)O. However, as indicated earlier, rather than fitting their somewhat limited data to an empirical expression,[46] it is more appropriate to utilize the model outlined in this section. Thus, using their measured values of the tracer diffusion coefficients of Ni and Co ions in pure CoO in air (P_{O_2}=0.21 atmos.), given as

$$D_{Co}^{T,CoO}(a_O = 0.46) = 5.0\times10^{-3}\exp[-160800(J/mole)/RT] \qquad (31a)$$

$$D_{Ni}^{T,CoO}(a_O = 0.46) = 3.3\times10^{-2}\exp[-197600(J/mole)/RT] \qquad (31b)$$

the ratio of diffusivities of the two cations in pure CoO can be obtained. Then, with a value for the correlation factor for Co diffusion in pure CoO of 0.782, and the corresponding value for Ni diffusion in the same oxide calculated from enq.(12), the ratio Γ_{Co}/Γ_{Ni} is calculated. Furthermore, using eqn.(13), $p = \Gamma_A f_A/\Gamma_B f_B$ can be calculated for other compositions. Finally, using the value of $D_{Co}^{T,CoO} = D_{Co}^{CoO}/f_o$ and eqn.(11) with the total vacancy concentation, $\sum[V]$, obtained from eqns.(14) and (17) enables the constant $2\Gamma_{Co}a^2/f_o$ to be found. Thus, D_{Co} and similarly D_{Ni} can be calculated as functions of oxide composition, oxygen activity and temperature.

Figure 4 shows a typical variation of D_{Co} and D_{Ni} with oxide composition, ξ, at different oxygen activities. Both diffusivities increase with Co content of the oxide and the oxygen activity, primarily due to the concomitant increase in vacancy concentration. However, unlike in the simple defect model used earlier,[43,44] $\log D_{Co}$ (or $\log D_{Ni}$) is not exactly a linear function of composition. This is shown more clearly in figure 5 which presents $\partial \ln D_{Co}/\partial \xi$ and $\partial \ln D_{Co}/\partial \ln a_O$ as functions of ξ and a_O; p, the ratio of diffusivities, and which depends only on composition, is also shown.

As a final point in this section, it is perhaps appropriate to examine how the diffusivities calculated according to this model compare with the experimental data of Chen and Peterson.[29] This comparison is shown in figure 6 where the solid curves represent values calculated from eqns.(11), (13), (14) and (17) using equilibrium constants according to eqns.(29) and (30), and eqn.(31) in conjunction with eqns.(12) and (11) to obtain Γ_{Ni}/Γ_{Co} and $2\Gamma_{Co}a^2/f_o$. The calculated self-diffusion coefficients are converted to tracer diffusion coefficients using the correlation factor (f_o) of 0.782. The agreement falls off rapidly as the NiO content of the solid solution increases, and this is presumably due to the variation in defect concentration with composition, not being adequately expressed by the constants given in eqn.(30). When these equilibrium constants calculated for T=1573°K are reduced in order to obtain a best fit to the experimental results, much better agreement can be obtained. A comparison between experimentally measured tracer diffusivities and the diffusivities calculated using K_{Vz}^{NiO}, K_V^{NiO} and $K_{V'}^{NiO}$ values reduced by 40% is shown in figure 7. Although the reduced equilibrium constants give better agreement to experimentally measured D^T data, those values given by Osburn and Vest[52] in eqn.(30) are still used in the actual calculations. Calculated results will be presented and discussed in later sections.

III. EXPERIMENTAL PROCEDURES

A. Experimental Apparatus

The experimental rig was constructed so that oxidation kinetics can be monitored continuously using the thermogravemetric method. A schematic diagram of the rig can be seen in figure 8 and a photograph in fig. 9. The whole system was leak checked using a high vacuum He leak detector before it was put into operation.

The microbalance used is a Cahn 2000 model, which has a maximum accuracy of 0.1 μg when operated under room temperatures with a total sample weight of less than one gram. This accuracy was reduced to 10 μg at the oxidation temperature (1000°C) due to convection flows within the reaction tube. The microbalance is supported on an air-cushioned platform to minimize vibration. A constant small flow of Ar was introduced into the balance chamber to keep the microbalance in an inert atmosphere.

Specimen and tare weight pan are both suspended by means of a very fine quartz fiber with a diameter of 0.1-0.5 mm. The tare weight pan is isolated in a pyrex chamber, on the inside of which was coated a thin film of Au to avoid static charge build-up. The suspended specimen can be centered using the leveling screws so that the quartz fiber is not touching any part of the apparatus, and a truly free suspension can be achieved.

The furnace tube assembly was designed so that gas entering the reaction tube reaches a state of equilibrium before coming into contact with the specimen. It is important that fully equilibrated gas mixtures are used in laboratory studies of high-temperature oxidation of this kind. Equilibrium is important because the equilibrium partial pressure of oxygen (P_{O_2}) determines the reactive potential of the gas from a thermodynamic point of view. A detailed sketch

of the furnace tube assembly and the path of gas flow is shown in fig. 10. The assembly consists of three parts, a gas mixing chamber, an inner guiding tube and an outer reaction tube. Both the inner and outer tube material is mullite, and their demensions are 1/3 inch OD, 1/4 inch ID, and 1-1/4 inch OD, 1 inch ID respectively.

Reactant gas enters the assembly through the gas inlet (i), fig. 10; it then passes down between the outer and inner tubes into the furnace, where it should come to equilibrium at the furnace temperature. The equilibrated gas, on reaching the specimen, enters the inner tube through its opening at (ii). The gas then travels up the inner tube and exits via the gas outlet at (iii). The pressure of Ar for the balance chamber was always kept below the reactant gas pressure to prevent Ar from flowing into the reaction tube. The flow rate of the reactant gases was controlled via a model FC-1P Hasting mass flowmeter and flow transducer, and flow rate fluctuation could be minimized to ±1 cc/min for an experimental run of 360 hours.

The furnace used is a Quad Elliptical radiant heating furnace which can heat up to 1000°C in 5 minutes. Temperature inside the furnace was controlled using Pt-PtRh thermocouples located in sheaths next to the reaction tube. (Fig. 9.) Both the control and read-out thermocouples are connected to a Research Inc. model 640UD process controller in connection with a Diarac model 402A trandicator, and the temperature could be controlled within ±1 degree. Temperature inside the reaction tube at the position of the specimen was calibrated using another thermocouple replacing the length and position of the quartz fiber used to suspend the specimen. This calibration was done frequently (after every 15-20 experimental runs), and the variation of these calibrations was within ±5 degrees.

B. Materials and Material Preparation

A series of nickel-cobalt alloys was obtained from International Nickel Company Ltd., containing 1, 5, 10, 20, 40, 60 and 80 weight % cobalt. Chemical analysis results showed that these alloy compositions were actually 1.2, 5.1, 10.9, 20.7, 38.2, 60.5 and 80.0 wt.% respectively.

The alloys were prepared by vacuum melting using 99.97% nickel and 99.6% cobalt. The manufacturer's analysis for impurities in wt.% was as follows:

NICKEL	COBALT
C=0.008	C=0.011
S<0.002	S=0.001
Fe<0.03	Fe<0.05
Pb<0.002	Ni<0.34
B<0.001	Cu<0.005
Cr,Co,Mo,Ti,Al,<0.01	Zr,Al,Si,Cr,Mn,Tl,Mg,<0.01
Si,Mn,Zr,Mg,Cu,<0.002	

Since nickel was the major impurity in the cobalt, the overall purity of the alloys was better than 99.95%.

Specimens 1.5cm x 0.6cm were cut from a sheet 0.063cm thick. A 2mm diameter bore was drilled on the face of each specimen for suspension purposes. The specimens were thoroughly degreased in acetone, then annealed in a quartz tube at 950°C for 24 hours under 5 millitorrs of argon pressure (measured at room temperatures). Prior to each experimental run, the specimen surface was polished with silicon carbide grit papers from 240, 320, 400, to 600 grit, using water as the lubricant. After the polishing procedure, the specimen was ultrasonically cleaned with soap and water, and subsequently rinsed with

water. Dimensions of the polished specimen were measured down to 0.001mm using a micrometer. The specimen was finally rinsed with ethyl alcohol before it was put on the microbalance for an oxidation experiment.

The reactant gas used to obtain a high oxygen potential was high purity oxygen from Matheson. This gas was used without further purification. A mixture of research grade 0.1% carbon monoxide in carbon dioxide, also from Matheson, was used to obtain a low oxygen potential atmosphere. The equilibrium P_{O_2} value for this CO/CO_2 mixture at 1000°C is 6.0×10^{-9} atm., according to the reaction

$$CO + \frac{1}{2}O_2 \rightarrow CO_2 \qquad \Delta G = -42459\ cal/mole$$

This oxygen partial pressure is about two orders of magnitude higher than the dissociation pressure of NiO at 1000°C, and three orders of magnitude higher than that of CoO.

C. Methods of Investigation

All oxidation experiments were carried out at 1000°C using the microbalance apparatus described previously. Specimens were put in the system immediately after polishing and cleaning, then the reaction tube was flushed with Ar to remove any residual air in the system. After the Ar flush, the reaction tube was equilibrated with a steady flow of the reactant gas; at the same time, balance stability was observed on a strip chart recorder. Oxidation was initiated by switching on the furnace, and weight gain was monitored continuously on the recorder. After about 24 hours of oxidation under high oxygen potential or 70 hours under low oxygen potential, reaction was stopped by turning off the furnace and the specimen was cooled in a continuous flow of the reactant gas. The cooling process from 1000°C to < 100°C usually took about half an hour, and the reaction tube was flushed with Ar before specimens were

taken out and stored in a dessicator for further analysis. Total weight gain obtained from the microbalance recording was often compared with the difference in initial and final weights of the specimen, measured independently on a model SEA-1 Torsion balance (with 0.1mg accuracy). Such comparison acted as a test to the microbalance's calibration.

The oxidized specimen was observed under scanning electron microscope (SEM) for its surface morphologies. Before examination using the SEM, all specimens were coated with gold using a gold-sputtering unit. This was done to compensate for the non-conductive properties of the oxide. Specimen cross sections were obtained by mounting the specimen in a clear epoxy and polished with succesively finer silicon carbide grits and diamond pastes to one micron. The cross section was then examined under an optical microscope or an electron probe microanalyzer.

The microanalyzer used in this research was a MCA-Model 5 analyzer. It was used principally to determine elemental concentration profiles on cross-sectioned samples across the oxide scale into the alloy. Spot analysis was carried out to establish the concentrations of Ni and Co, using a 1μm spot size with a 15KeV excitation voltage. One major drawback of this particular instrument is the inability to detect oxygen. Therefore, analysis of Ni and Co content in the oxide scale was done by an oxygen subtraction method on a microcomputer. All samples had to be carbon-coated to prevent excessive charging under the electron beam.

IV. RESULTS

A. Kinetics

Oxidation kinetics were obtained using the thermogravemetric method on the apparatus described in section III. Ni-Co alloys in the composition range of 1-80wt% Co were oxidized under two different oxygen potentials: high oxygen potential with P_{O_2} = 1 atm. and low oxygen potential with P_{O_2} = 6×10^{-9} atm. attained from 0.1% CO/CO_2 mixture. Figure 11 shows typical kinetic curves obtained during exposure of these alloy specimens to the two environments at 1000°C. In both cases, oxidation kinetics seem to be parabolic with the rate constant much slower at the lower oxygen potential, as expected.

A comparison of the parabolic kinetics of alloys with different compositions oxidized under 1 atm. O_2 at 1000°C is shown in figure 12. The data were analyzed by plotting $(\Delta m / A_o)^2$ vs. time, where Δm is the weight gain and A_o is the initial specimen surface area, assuming negligible change in total surface area during oxidation since the oxide formed was relatively thin compared to the bulk alloy. Good parabolic behavior was observed for all the Ni-Co alloys. A short non-parabolic transient stage was seen with the slower oxidizing alloys (those with less Co content), but parabolic kinetics soon took over after no more than five hours. The parabolic rate constant (k_p) for each alloy can be obtained from the slope of the corresponding straight line in figure 12. Usually, more than one specimen of each alloy was tested and independent k_p values were measured. Results were quite reproducible and fell within 5%. These parabolic rate constants are summarized in Table 1 where each column contains k_p values obtained from different oxidation experiments, and the rate of scale growth is seen to go up concomitantly with Co content in the alloy.

TABLE 1

Parabolic Rate Constants of Alloys Oxidized Under 1 atm. O_2

Alloy Composition (wt% Co)	1	5	10	20	40	60	80
Rate Constant	1.26	1.76	1.95	3.44	9.02	20.8	50.2
$\times 10^{-10}$	1.35	1.71	2.38	3.44	9.13	20.7	-
$(g^2 cm^{-4} sec^{-1})$	-	-	-	3.19	-	-	-

Oxidation kinetics of these Ni-Co alloys oxidized under low oxygen potentials also showed parabolic behavior (figure 13), although there was a much longer non-parabolic transient stage during the first hours of exposure to the oxidizing atmosphere. Parabolic rate constants were obtained from the straight line portion of the curves. Table 2 summarizes the kinetic results of alloys oxidized under the low oxygen potential.

TABLE 2

Parabolic Rate Constants of Alloys Oxidized Under 6×10^{-9} atm. O_2

Alloy Composition (wt% Co)	5	10	20	40	60	80
Rate Constant	8.37	8.62	8.65	11.8	17.5	44.4
$\times 10^{-12}$	7.01	-	-	13.5	-	47.5
$(g^2 cm^{-4} sec^{-1})$	6.60	-	-	14.1	-	-

The rate constants shown in Table 2 tend to scatter more than those obtained for alloys oxidized under high oxygen potentials, probably because total weight gain was much smaller and higher balance sensitivity was required. Nevertheless, good reproducibility was still achieved and the data scattered

within 10%. A comparison of the variation of k_p with alloy composition between alloys oxidized under both high and low oxygen potentials is shown in figure 14. In both cases, the rate constants increase with Co content in the alloy. The relationship is near logarithmic with alloys oxidized under high oxygen potentials. At low P_{O_2}, the oxidation rates vary only slightly with composition as the alloys become richer in Ni.

B. Oxide Morphologies and Compositions

All compositions of Ni-Co alloys oxidized under both high and low oxygen potentials formed a uniform external scale and some internal oxide particles beneath the external scale. Figure 15 shows a polished cross section of a Ni-60%Co alloy oxidized under the two oxygen potentials. In both cases, there were coherent external scales with oxide particles formed under the scale-alloy interface. The pores in the scale may well be artifacts, since it is difficult to polish these scales without a certain degree of pullout. The number and size of the internal oxide particles increased with oxidation time, and the precipitation zone deepened as shown in figure 15a and b. The width of the precipitation zone within the alloy relative to the total thickness of the external scale greatly increased as the ambient oxidizing potential was lowered from P_{O_2} = 1 atm. to $P_{O_2} = 6 \times 10^{-9}$ atm., and the internal oxide particles were larger and more widely spread. (compare figure 15b and c)

Surfaces of the external scales revealed by SEM exhibited very uniform and crystallographic oxide grains as shown in figure 16 where SEM top views of the oxides formed on Ni-20%Co specimens oxidized under 0.1% CO/CO_2 for 17 hours and 70 hours are compared. It is seen that a uniform morphology of the scale was established within the first hours of oxidation. Further oxidation time resulted in an increase in the average size of the oxide grains and a reduction

in their number: this may have resulted from a growth selection process. Larger grains developed near the scale-gas interface while smaller grains near the scale-alloy interface as demonstrated in figure 17. The scale shown in figure 17 was partially fractured and the broken pieces removed. Because the scale was highly adhesive, its complete seperation from the alloy surface was not achieved. A thin layer of the fractured scale still attached to the alloy surface is seen on the upper right part of figure 17. Although it is often difficult to analyze fracture surfaces, the oxide grains observed in this section are definitely smaller than those near the lower left of the micrograph, which are part of the unbroken scale external surface.

Typical morphology of the internal oxide particles formed beneath the scale-alloy interface is shown in figure 18. The internal oxides are distributed randomly within an internal oxidation zone. However, no sharp delineation of an internal oxidation front is observed. The fraction of internal oxide precipitates within the internal oxidation zone falls off with distance into the alloy.

The depth of internal oxide formation zone relative to external scale thickness increased with decreasing Co content in the alloy. This effect was not so obvious for alloys oxidized under high oxygen potentials, because the internal oxidation zones in these cases were very narrow. However, the effect becomes more obvious for oxidation carried out under low oxygen potentials since the internal oxidation zones were much wider, and larger internal oxide particles were formed. Figure 19 compares the depth of internal oxide formation on a Ni-40%Co and a Ni-80%Co specimens both oxidized under low oxygen potentials. The internal oxides are seen penetrated deeper into the underlying alloy for the 40%Co specimen.

The rough front of the internal oxidation zone corresponds to the Co depletion profile in the alloy as demonstrated in figure 18 where the electron

micrograph of a Ni-40%Co specimen taken inside the chamber of an electroprobe microanalyzer was compared with its corresponding microprobe analysis. The path of the electron beam through the external scale into the alloy cutting through an internal oxide particle was outlined on the micrograph by the arrow. The microprobe trace of the internal oxide particle in figure 20 indicates that the particle is also a solid solution of Ni-Co oxide.

Composition of these internal oxide particles was examined using the electron microprobe analyzer. A spot size of 1 μm with 15 KeV accelerating voltage was used to minimize beam penetration through the oxide particle into the underlying alloy. Only large particles with approximately 10 μm diameter were chosen for analysis. The electron beam was centered on the particle and the penetration depth measured from this centered point to the scale-alloy interface. Figure 21 shows the composition of these internal oxide particles as a function of distance away from the scale-alloy interface for three different alloys oxidized under 0.1% CO/CO_2 for 360 hours. Scattering of the data points may be due to possible thin sectioning of the particle and penetration into the underlying alloy, or to the irregularity of the scale-alloy interface as well as the irregular shapes of the particles. The general trend of these results shows that the internal particles are solid solutions of Ni-Co oxides with an enriched Co content. The Co enrichment increases for particles farther away from the scale-alloy interface. Alloys with lower Co content tend to form internal oxides richer in Co with a longer internal oxidation zone.

Distribution of the cations, Co and Ni, within the solid solution oxide scales as well as in the underlying alloys was also observed using an electronprobe microanalyzer. Since the scale growth kinetics is parabolic, parametric variables λ and y can be used so that all concentration profiles can be made invariant with time, t. λ and y were defined in section II as

$$\lambda = x / \sqrt{t} \quad ; \quad y = x / x_s$$

where x is the distance coordinate and x_s is the total thickness of the scale.

Figure 22 shows the Co concentration profile of Ni-60%Co specimens oxidized under high and low oxygen potentials. In both cases, Co is enriched near the scale-gas interface. A much wider Co depletion zone in the alloy is observed for oxidation under low P_{O_2}, and the concentration profile within the scale appears flatter with a higher degree of Co enrichment. (This is seen through the average Co content in the scale). A comparison of the cation concentration profile for four different alloys oxidized under 0.1% CO/CO_2 is shown in figure 23. All of these profiles show a wide Co depletion zone in the alloy and the zone becomes wider as the Co content in the bulk alloy decreases. Concentration profiles within the scale all have similar shapes and the Co content increases from the scale-alloy interface towards the scale-gas interface. The average Co content in the oxide and the degree of Co enrichment, taken as the ratio of the average Co concentration in the scale over the bulk Co content, of each alloy is summarized in Table 3.

TABLE 3

Degree of Co Enrichment in the Scale

bulk Co content in the alloy	average Co content in the scale	degree of Co enrichment
$[Co]_{bulk}$	$[Co]_{ave}$	$\frac{[Co]_{ave}}{[Co]_{bulk}}$
10	25	2.5
20	36	1.8
40	52	1.3
60	67	1.1

These result indicates that the degree of Co enrichment in the scale gets higher as the bulk Co content in the alloy becomes lower. The relationship is not linear, but goes up almost logarithmically.

C. Theoretical Analysis

Results of the theoretical calculations followed the theories treated in section II. The outcome of the computer simulation includes the cation concentration profile, the parabolic rate constant and the cation vacancy concentrations across the scale. Those calculated for oxidation under 1 atm. O_2 will be presented first and compared with available experimental data.

(i) *Oxidation Under High Oxygen Potentials*

As discussed earlier, Ni-Co alloys oxidized under 1 atm. O_2 approach the limiting case where diffusion in the alloy can be neglected. Therefore, the cation concentration profile was only considered within the scale. Figure 24 shows the calculated cation profiles across the scales formed on four Ni-Co alloys oxidized under 1 atm. oxygen, and compares them with the corresponding profiles determined by electron microprobe analysis.[53] The agreement between theoretical calculations and experimental data is very good considering the various approximations made in the theories and the scatter of the cation concentrations obtained by microprobe analysis.

The value of the parabolic rate constant k is obtained as a direct result of the iteration procedure of the computer simulation. k is converted to the gravemetric rate constant, k_p, using the expression

$$k = \tfrac{1}{2}\left(\frac{M_{(Ni,Co)O}}{\rho_{(Ni,Co)O} M_O}\right)^2 k_p$$

where M_O is the atomic weight of oxygen, $M_{(Ni,Co)O}$ is the average molecular weight of (Ni,Co)O of metal ratio equal to that in the specific alloy, and $\rho_{(Ni,Co)O}$

is the (Ni,Co)O density (g/cm^3) calculated from room temperature densities of pure metal oxides[54] assuming a linear dependence between these oxides with composition. These calculated k_p values are compared with experimentally obtained data from this work and some other workers[53,55-57] as shown in figure 25. The agreement between theoretical and experimental values of k_p is good in both magnitude and compositional variation.

An additional result of the theoretical calculations is the vacancy concentration through the growing scale. Figure 26 shows the total vacancy concentration through the scales of the four alloys. The overall vacancy gradient across the scales increases with increasing Co content of the alloy, and vacancy concentration increases towards the scale-gas interface where the scale is most rich in Co.

(ii) *Oxidation Under Low Oxygen Potentials*

When oxidation of Ni-Co alloys is carried out under very low oxygen activities, the diffusivities in the scales are markedly reduced and diffusion within the alloy needs to be included in the calculation of the cation concentration profile. The method of calculation was discussed in section II. A theoretical profile across the scale and within the alloy was calculated for a Ni-38%Co alloy oxidized under 6×10^{-9} atm. O_2. This result is compared with the corresponding cation profile determined by electron microprobe analysis as shown in figure 27. The theoretically calculated profile across the scale is seen to be steeper than that obtained experimentally, but the total Co content in the scale for both cases is about the same. The two profiles within the alloy agree better as they recede away from the scale-alloy interface.

Although the calculated and experimental cation profiles determined for the Ni-38%Co alloy oxidized under low oxygen activities do not agree very well, the corresponding scale growth rate come close to one another. The computed

and experimentally measured rate constants expressed in $g^2\ cm^{-4}\ s^{-1}$ are 1.06 $\times\ 10^{-11}$ and 1.20 $\times\ 10^{-11}$ respectively.

The calculated total vacancy concentration across the scale is shown in figure 28, where similar calculations for the same alloy oxidized under 1 atm. O_2 is included for comparison. In both cases, the vacancy concentration increases towards the scale-gas interface. Larger vacancy concentration gradients are observed for higher ambient oxygen potentials, and the average amount of vacancies present in the scale is about 1.5 orders of magnitude lower when the oxygen activity (a_O) is lowered from 1 to 7.8 $\times\ 10^{-5}$.

V. DISCUSSION

A. Kinetics

The oxidation kinetics of Ni-Co alloys oxidized under both high and low oxygen potentials appeared to be parabolic, which suggests that scale growth is diffusion controlled. Many previous workers[57,58] who studied the oxidation behavior of Ni and Co had pointed out that the rate limiting process for scale formation is outward diffusion of metal cations through the cation vacancies in the scale. Because of this outward flux of materials, most grain growth occurs near the scale surface, and as a consequence, larger oxide grains were observed near the scale-gas interface relative to those grains near the scale-alloy interface as shown in figure 21.

The parabolic rate law was not always followed as soon as oxidation had started. This was especially so with slower reaction rates, such as those resulting from oxidation under low oxygen potentials where a long initial stage was observed with a faster rate before parabolic kinetics took over (see fig. 13). In its most general description, the initial stage is the time needed for a uniform and relatively thick and large-grained scale to develop in order for steady state lattice diffusion to be established. Therefore, the slower the oxidation rate, the longer the initial stage. Rapid oxidation during the initial stage is often believed to be caused by the presence of rapid diffusion paths through the very thin oxides. These diffusion paths could be dislocations and sub-grain boundaries,[59] especially when the oxide grains at this stage are very small with relatively high grain boundary areas. The presence of large electric fields across thin oxide films can also contribute to the faster rate until the oxide film exceeds about 50 A as pointed out by Graham et al.[60] Presence of impurities, such as sulfur,[61] can impede the recrystallization process which is known to

occur during the early stages of oxidation,[62] thereby extending the period of rapid non-parabolic kinetics.

The variation of the parabolic rate constant, k_p, with alloy composition is shown in figure 14. The rate constant is seen to increase logarithmically with increasing Co content in the alloy when the ambient oxygen pressure is 1 atm. Chen and Peterson[29] had studied the diffusion, semiconductivity and non-stoichiometry in (Ni,Co)O crystals and found that the tracer diffusivities of Ni and Co in (Ni,Co)O crystals at 1445 and 1300°C in air both increased with increasing Co content in the oxide. The relationship is approximately logarithmic, decreasing towards pure NiO as shown in figure 29. Since the mechanism of scale growth of Ni-Co alloys is cation outward diffusion through the oxide, as discussed earlier, the major deciding factor for the rate constant will be the diffusion coefficients of the cations within the oxide. When the oxide has the same composition as the alloy, that is, there is no selective oxidation of the less noble component, the oxidation rate will be expected to increase with alloy composition in similar fashions as cation diffusivities are increased with Co content in the oxide. This is indeed the case with alloys oxidized under 1 atm. O_2. Very little Co enrichment was observed in their oxide scales (see figure 24), and the composition of the oxide is similar to that of the bulk alloy. The variation of k_p with alloy composition is near logarithmic as Chen and Peterson's observations on the variation of the cation diffusivities with Co content in the oxides. The major contributing effect to the increase in cation diffusivities in (Ni,Co)O with Co content could be an increase in the total cation vacancy concentrations in the oxides. Since CoO is 10-100 times less stoichiometric than NiO,[32] an increase in Co content in the oxide would naturally increase the available vacancies for diffusion.

Although cation diffusivities within the oxide scale are the major factor in

deciding the actual oxidation rate, the shape of the diffusion path as well as the degree of Co enrichment in the oxide scale are all contributing factors. When Ni-Co alloys are oxidized under low oxygen potentials, selective oxidation of Co takes place. This effect is manifested through the enrichment of Co content in the external oxide scales, and as a consequence, leaves a Co depletion zone in the underlying alloys. Table 3 in section IV compares the degree of Co enrichment in the scale of four different alloys. As a result of the enrichment, diffusivity of cations through the scale will increase and a higher rate constant than if there were no selective oxidation will be observed. Since the degree of Co enrichment in the scale increases drastically with alloys poorer in their bulk Co content, but not so much with alloys richer in Co, the relationship between oxidation rate constants and alloy compositions is no longer near logarithmic like those oxidized under high oxygen potentials (see figure 14). To better illustrate this phenomenon, the rate constant for the alloys oxidized under 6×10^{-9} atm. P_{O_2} is lowered according to its degree of selective oxidation which is taken from the degree of Co enrichment listed in Table 3. The resultant relationship is the dashed line shown in figure 30, which is again logarithmic. Therefore, the increase of the rate constants towards the Ni rich end of the alloy composition is mainly, if not solely, due to the increase in Co content in the scale.

B. Selective Oxidation

As discussed in section I, binary alloys which form completely miscible solid solution oxides upon oxidation, such as Ni-Co alloys above 950°C, can have scales with varying overall composition. The relative proportions of the alloying components A and B in the scale are determined by the oxidation potentials of A and B and their diffusion rates in the scale and alloy. Two limiting cases can be identified:

(1) When diffusion in the alloy is very slow in comparison with that in the scale, the average amount of cation A or B in the scale will be the same as that of the bulk alloy. As a consequence, there is no selective oxidation, and the differing tendencies of the alloy components to oxidize, as expressed by $\delta(\Delta G)$ ($= \Delta G^{o}_{AO} - \Delta G^{o}_{BO} > 0$, since B forms the more stable oxide), has no influence on the composition of the scale.

(2) When diffusion in the alloy is much faster than that in the scale, selective oxidation of the more stable oxide takes place. Composition of the resulting oxide scale depends on the degree of $\delta(\Delta G)$. If $\delta(\Delta G)$ were sufficiently large, the scale can be virtually pure BO.

Ni-Co alloys oxidized under 1 atm. O_2 approximate to the first limiting case. The cation concentration profiles across the scale show very little Co enrichment (see figure 24). As a consequence, there is little selective oxidation and Co depletion within the alloy is only a very narrow zone beneath the oxide scale as shown in figure 22. The slight depletion of cobalt in the alloy immediately beneath the scale is due to the fact that Co has a marginally greater affinity for oxygen than Ni and is consequently slightly enriched in the steady-state scale. Also, since Co diffuses out through the scale faster than Ni,[29] Co enrichment at the scale outer surface is observed.

When the ambient oxygen partial pressure is lowered from 1 atm. to 6×10^{-9} atm., the solid solution oxide scales formed become more stoichiometric, since the degree of nonstoichiometry in both NiO and CoO decreases towards their dissociation pressures.[32] This increase in stoichiometry is also demonstrated by the theoretical calculation of total vacancy concentrations within the scale as shown in figure 28. As a result of this increase in stoichiometry, a "denser" oxide scale is formed in terms of its available vacancies for diffusion, and diffusivities of cations in the scale will drop considerably. This is more so

for scales formed on alloys poorer in Co content because the cation diffusivities in the scale are very concentration dependent. They are usually two orders of magnitude lower in NiO than in CoO at 1000°C in air.[29] On the other hand, diffusivities in the alloy do not change with changing oxidizing potentials and there is relatively slight dependence on alloy composition. Therefore, the difference between diffusivities in the alloy and in the scale decreases with decreasing ambient oxidizing potential, and the difference is less for alloys poorer in Co content. The situation here no longer approximates to the first limiting case but begins to approach the second one, and selective oxidation of the more stable oxide (CoO) is observed (see figure 23) with a higher degree for alloys poorer in Co content due to a smaller difference in diffusivities in the alloy and in the scale. Since the difference in oxidation potential, expressed by $\delta(\Delta G)$, for Ni and Co is relatively low,[26] the oxide scales formed with selective oxidation is still a solid solution of NiO and CoO rather than pure CoO. A larger Co depletion zone is observed in the alloy as a result of the enrichment of Co into the scale, and within this depletion zone, discrete internal oxide particles of (Ni,Co)O are formed.

C. Internal Oxide Formation

Internal oxidation in the Ni-Co system is somewhat different from that classically reviewed by Rapp,[63] Swisher[64] and Meijering.[65] They considered the formation of internal oxide in dilute alloys for the situation where the internal oxide is a different phase from the surface scale. It has been pointed out by Wagner[66] that in certain circumstances it is possible to have the same oxide formed both as an external scale and as an internal oxide precipitate within the alloy. Growth of an external scale enriched with the less noble component produces a depletion of that component in the alloy beneath the scale. If diffusion of oxygen into the alloy occurs, at some depth into the alloy the solubility

product for oxide formation could well be exceeded. Thus, formation of internal oxide in these systems stems from the depleted zone of the less noble component of the alloy below the surface scale.

It was first suggested by Rhines[67] in studying the oxidation of copper alloys that metal oxides at the scale-alloy interface can dissociate into metal atoms and oxygen atoms which are dissolved in the alloy. Suppose that the oxygen activity in the two phase region alloy+(Ni,Co)O is determined by the equilibrium $(Ni,Co)O_{(s)} \rightarrow (Ni,Co)_{alloy} + O_{(dissolved\ in\ alloy)}$. Then, at the interface between the external scale and the alloy where the Co activity is low (as in fig. 23), the concentration of dissolved oxygen atoms is greater than in the interior of the alloy where the Co activity is high. Thus there is an oxygen concentration gradient in the alloy resulting in inward diffusion of oxygen and precipitation of small internal oxide particles in the alloy. Quantitative analysis by Wagner[66] showed that the internal oxidation process would be favored if the diffusivity of oxygen in the alloy (D_O) is relatively high compared to the interdiffusion coefficient of the alloy (D_{AB}). Few data are available for the diffusivity of oxidant in Ni, Co alloys. Typical values for oxygen lie in the range 10^{-8} - 10^{-6} cm^2/s at 1273°K,[17] and D_{AB} for Ni-Co alloys at the same temperature is about 10^{-12} cm^2/s .[68] This large difference in diffusivities enhances the internal oxidation process and internal oxide particles are formed within the entire Co depletion zone as shown in fig. 20.

The reasons why the internal oxide precipitates observed are solid solution (Ni,Co)O are because Ni, Co alloys form solid solution oxides over their entire composition range above 950°C, and that the difference in the affinity for oxygen is slight. Therefore, although Co is the less noble component in the alloy, the precipitates still have a substantial amount of Ni dissolved in them. As the Co concentration increases towards the bulk alloy and consequently the con-

centration of dissolved oxygen decreases, the internal oxide particles will become richer with the less noble component, Co. This is indeed the case observed experimentally as shown in figure 21.

The Co content in the internal oxide particles shown in figure 21 can be compared with the Co concentration profile of their corresponding alloy within the internal oxidation zone as in figure 31. The solid line in figure 31 is the Co concentration profile within the internal oxide precipitation zone, and the points represent Co concentration in the internal oxide particles. The activity of Co in the oxide particles should be the same as that in their surrounding alloy, since the system is essentially at thermodynamic equilibrium. Table 4 summarizes the relationship between Co content in the oxide precipitates and in their surrounding alloys for the three alloys oxidized under 6 $\times 10^{-9}$ atm. O_2.

TABLE 4

Co Concentration (in wt%) in Internal Oxide Particles and in Their Surrounding Alloys

Ni-60%Co		Ni-40%Co		Ni-20%Co	
$[Co]_{alloy}$	$[Co]_{oxide}$	$[Co]_{alloy}$	$[Co]_{oxide}$	$[Co]_{alloy}$	$[Co]_{oxide}$
39.0	57.6	24.7	48.4	12.5	30.1
41.7	61.4	26.5	45.0	12.9	25.5
46.2	63.6	28.3	50.0	13.9	30.0
47.5	61.1	34.0	54.4	17.4	37.2
57.6	64.0	34.5	57.2	17.8	40.0
-	-	38.7	58.2	-	-

These results are plotted as $[Co]_{oxide}$ vs $[Co]_{alloy}$ in figure 32. Although the data points in figure 32 are confined within 10-60wt% Co in the alloy, the general trend still shows that the solid solution oxides in equilibrium with the alloys

have a relatively higher Co content when the alloy is low in Co. This behavior seems to indicate that the activity of Co in the NiO-CoO system exhibits a negative deviation from Raoult's law as shown schematically in figure 33(b).

The activity of cobalt in the Ni-Co system shows Raoultian behavior (fig. 33(a)), since the Ni-Co system at 1273°K forms an ideal solid solution.[69] Under thermodynamic equilibrium, a_{Co} (in the alloy) = a_{Co} (in the oxide). Therefore, an alloy with 20% Co would correspond to an oxide with ~38% Co following abcd on figure 33, and similarly, following efgh, an alloy with 60% Co will be in equilibrium with an oxide of ~65% Co. These relationships correspond with those observed experimentally as shown in figure 32, and explains why a relatively higher Co content is observed in internal oxides formed within alloys poorer in Co.

D. Theoretical Analysis

(i) *Oxidation Under High Oxygen Potentials*

A comparison between theoretically calculated and experimentally measured cation concentration profiles across the oxide scales formed under 1 atm. O_2 is shown in fig. 24. The agreement is not only good but shows an improvement over earlier calculations[43] where a relatively simple defect model was used as discussed in section II. Figure 31 compares the cation profiles calculated in this work and in the previous work with experimentally determined profiles by electron microprobe analysis. Although the improvement is not tremendous, because those calculated from the previous work have already achieved fair agreement with experimental data, there is still a better overall fit with each experimentally determined profile. Furthermore, the dip in the previously obtained theoretical profile for Ni-80%Co and Ni-38%Co alloys near the scale-alloy interface cannot be justified by diffusion theories, but such a dip is no longer present in this calculation.

Although the theoretical analysis presented in this work has brought better agreement between calculated and experimentally determined profiles, the fit is still not perfect. This can be due to the various assumptions made in the calculations and the scatter in the cation concentrations obtained by microprobe analysis as mentioned earlier. In addition, the lack of a very complete defect model for the nonstoichiometric oxide, the limited experimental defect equilibrium constants and the lack of any theory accounting for the variation of the elementary jump frequencies of the cations (Γ_A and Γ_B) as a function of composition, are all possible contributing factors toward the imperfect fit.

Additional results of the theoretical calculations include the oxidation rate constants and the variation in total vacancy concentration through the scale. They are presented in figures 25 and 26. The good agreement between calculated rate constants and those measured experimentally arises mainly because there is a good agreement in the cation concentration profiles across the scales. This is so because the growth rate of this type of solid solution scale is greatly dependent upon the distribution and concentration of the cations in the scale.

The total vacancy gradient through the scale is, of course, related to the growth rate of the oxide. Thus, the overall vacancy gradient across the scale, and the growth rate, increases with increasing Co content of the alloy. The vacancy concentration profile has a stronge dependence on the oxygen activities across the scale as shown in figure 35. The oxygen partial pressure varied from 1 atm. at the scale-gas interface to the dissociation pressure of the oxides at the scale-alloy interface, and as a consequence, the scale has the highest degree of nonstoichiometry at the scale-gas interface and the lowest degree at the scale-alloy interface. Co enrichment near the scale surface, due to its

higher affinity for oxygen and faster diffusion rate in the scale, also enhances higher vacancy concentration near the scale-gas interface since CoO is the less stoichiometric oxide. This compositional effect on the variation of the vacancy profiles through the scale coincides with the oxygen activity effect and therefore, is not as obvious.

(ii) *Oxidation Under Low Oxygen Potentials*

It is not the purpose of this work to extensively study the applicability of the theory described here to the oxidation behavior under very low oxygen potentials, although an attempt has been made with the Ni-38%Co alloy to see how the calculation would agree with experimental data. This comparison is shown in fig. 27. The poor agreement resulted, in general, from the lack of consideration of the dissociation of the oxides at the scale-alloy interface, followed by inward diffusion of the oxygen atom to form internal oxide particles. From the depth of internal oxidation zone found on these alloys oxidized under low oxygen potentials, it is clear that the inward oxygen diffusion process is no longer a negligible one. This process will cause the scale-alloy interface to move towards the original alloy surface and counterbalance the effect of a receding interface which results from the external scale growth. The moving boundary diffusion problem then, would have to involve not only outward cation diffusion through the scale, but also inward anion diffusion from the scale-alloy interface. Furthermore, the constant dissociation process of the oxides at the scale-alloy interface may upset the local thermodynamic equilibrium there. As oxygen at the scale-alloy interface dissociates from the scale and diffuses into the alloy, a new interface is created. The oxygen activity at this new interface would be higher, especially when the oxygen activity gradient near the scale-alloy interface is the steepest (see fig. 35), and a long diffusional process is necessary to bring it back to its equilibrium value again. Figure 36 shows the

comparison between experimental cation profile on the Ni-38%Co specimen oxidized under 6×10^{-9} atm. oxygen and a theoretically calculated profile allowing for the oxygen activity at the scale-alloy interface to be one order of magnitude higher than its equilibrium value. The agreement proves to be much better although it will not be right to say that this is the only factor preventing the theory and experiments from agreeing with one another.

The steeper theoretical cation profile in the scale shown on fig. 27 can also suggest that higher cation diffusivities (D_A and D_B) are being calculated, which could be due to a higher calculated vacancy concentration across the scale. Since there has been very little study of the defect structure of these oxides near their dissociation pressures, it is plausible that the defect model used in the analysis does not adequately describe the actual defect concentrations under these low oxygen partial pressures. Another reason for the difference in steepness of the two profiles in the scale could be due to an experimental error. Namely, the experimental oxygen potential in the oxidizing atmosphere (0.1% CO/CO_2) is actually lower than that predicted from thermodynamic equilibrium of the reaction $CO + 1/2\ O_2 \rightarrow CO_2$. If this were the case, the vacancy concentration gradient across the scale would be smaller and the experimentally measured cation profile would be flatter.

Values of the theoretical and experimental scale growth rate for this Ni-38%Co specimen are quite close regardless of the discrepancy between the cation profiles. These rate constants are, $k_{p(cal)} = 1.06 \times 10^{-11}\ g^2\ cm^{-4}\ s^{-1}$ and $k_{g(expt)} = 1.20 \times 10^{-11}\ g^2\ cm^{-4}\ s^{-1}$. This agreement is due to the fact that one of the boundary conditions set for the theoretical calculations is to make the enrichment of Co in the scale equal to the depletion of Co in the alloy. Since the theoretical and experimental profiles in the alloy agree somewhat better, the calculated average Co concentration in the scale is quite close to the

experimental value. As mentioned before, the growth rate of this type of oxide scale depends greatly on the average cation composition across the scale; therefore, the two growth rates agree fairly well.

VI. CONCLUSIONS

Ni-Co alloys in the composition range of 1-80 wt%Co oxidized at 1000°C under 1 atm. O_2 or 6×10^{-9} atm. O_2 all formed a solid solution external scale. The scale growth rate was found to be parabolic. When the ambient oxidizing potential was high, the parabolic rate constant increased nearly logarithmically with Co content in the alloy. This relationship arose from the increase in cation diffusivities within the scale which was caused by a concomitant increase in vacancy concentrations. The rate constants for alloys oxidized under the low oxygen potential behaved differently, with similar values for alloys low in Co content and increasing gradually towards the Co rich end of the composition. This effect was caused by the increasing degree of selective oxidation of the more stable oxide, in this case also the more nonstoichiometric oxide, in the external scale for alloys that are poorer in Co content. The difference in the degree of selective oxidation between alloys of different compositions and between alloys oxidized under the two extremes of oxygen potentials could be explained by considering the different diffusion rates in the alloys and in the scales.

A subscale of solid solution internal oxide precipitates was found beneath the external scale. The depth of the subscale was very narrow for alloys oxidized under the high oxygen potential, but became extensive for alloys oxidized under the low oxygen potential. All of these internal oxide particles were enriched in Co as compared to their bulk alloy compositon, and alloys with lower Co content formed precipitates that were relatively richer in Co. The fraction of internal oxide precipitates within the internal oxidation zone fell off with distance into the alloy and there was no sharp delineation of the front of internal oxidation. The depth of the internal oxidation zone corresponded to the depth of depletion of the less noble component in the alloy. In addition, the

composition of the oxide precipitates varied throughout the internal oxidaiton zone, with an increasing concentration of the more stable oxide component at increasing depths below the scale-alloy interface.

The theoretical analysis made use of Wagner's ternary diffusion model with a more refined defect model to express the compositional and oxygen activity dependence of the cation diffusivities. Calculated cation concentration profile and scale growth rate for alloys oxidized under the high oxygen potential showed very good agreement with experimental data. This good agreement demostrated that correct interpretation of the growth of these solid solution types of scales really requires as accurate as possible a model for the point defect structure of the oxide.

Similar calculations considering diffusion processes in the alloy as well as those in the scale for alloys oxidized under the low oxygen potential showed rather poor agreement with experimental data. A more complete theory was called for, where extensive oxygen dissociation at the scale-alloy interface and its subsequent inward diffusion causing internal oxide formation need to be included.

VII. REFERENCES

1. K. Hauffe, *Oxidation of Metals and Alloys*, Springer-Verlag, (1967)

2. O. Kubaschewski and B. E. Hopkins, *Oxidation of Metals and Alloys*, 2nd ed. Butterworth, London, (1967)

3. J. Benard, ed., *L'Oxydation des Metaux*, Vols. 1 and 2, Gauthier-Villars, Paris, (1963-4)

4. D. L. Douglass, ed., *Oxidation of Metals and Alloys*, American Society for Metals, Metals Park, Ohio, (1971)

5. J. Stringer, *Metall. Reviews* **11**, 113 (1966)

6. G. C. Wood, *Oxid. of Metals* **2**, 11 (1971)

7. J. Stringer and D. P. Whittle, *Rev. Int. Hautes. Temp. et Refrac.* **14**, 6 (1976)

8. G. R. Wallwork, *Repts. in Prog. in Physics* **39**, 401 (1976)

9. "*Oxidation of Metals and Alloys*", ASM Monograph, Cleaveland (1971)

10. "*Properties of High Temperature Alloys*", ed. Z. A. Foroulis and F. S. Pettit, Electrochem. Soc. Inc., New York, N. Y. (1977)

11. "*High Temperature Corrosion*", Commission of European Communities, Brussels (1979)

12. F. S. Pettit, J. A. Goebel and G. W. Goward, *Corrosion Science* **9**, 903 (1969)

13. P. Singh and N. Birks, *Oxid. of Metals* **13**, 457 (1978)

14. R. A. Perkins, "*Environmental Degradation of High Temperature Materials*" Proc. of the Institude of Metallurgists Conference, Douglas, Isle of Man. **2**, 511, (1980)

15. D. P. Whittle and G. C. Wood, *J. Inst. Met.* **96** , 115 (1968)

16. B. D. Bastow, G. C. Wood and D. P. Whittle, *Oxid. of Metels* **16**, 1 (1981)

17. D. P. Whittle, F. Gesmundo, B. D. Bastow and G. C. Wood, *Phil. Mag. A* **44**, 43 (1981)

18. C. Wagner, *Corros. Sci.* **9**, 91 (1969)

19. D. P. Whittle, B. D. Bastow and G. C. Wood, *Oxid. of Metals* **9**, 215 (1975)

20. P. Mayer and W. W. Smeltzer, *J. Electrochem. Soc.* **119**, 626 (1972)

21. G. C. Wood and I. G. Wright, *Corros. Sci.* **7** , 841 (1967)

22. P. Mayer and W. W. Smeltzer, *Oxid. of Metals* **10** , 329 (1976)

23. A. D. Dalvi and D. E. Coates, *Oxid. of Metals* **2**, 331 (1970)

24. B. D. Bastow, D. P. Whittle and G. C. Wood, *Proc. Roy. Soc. London* **A356**, 177 (1977)

25. N. N. Greenwood, *Ionic Crystals, Lattice Defects and Nonstoichiometry*, Butterworths, London, (1968)

26. J. F. Elliot and M. Gleiser, *Thermodynamics for Steelmaking*, Addision-Wesley, Reading, Mass., (1960)

27. K. Kiukkola and C. Wagner, *J. Electrochem. Soc.* **104**, 379 (1957)

28. R. J. Moore and J. White, *J. Mater. Sci.* **9**, 1393 (1974)

29. W. K. Chen and N. L. Peterson, *J. Phys. Chem. Solids* **34**, 1093 (1973)

30. J. J. Stiglich, J. B. Cohen and D. H. Whitmore, *J. Am. Ceram. Soc.* **56**, 119 (1973)

31. A. F. Wells, *Structural Inorganic Chemistry*, 3rd ed., Oxford University Press, (1962)

32. P. Kofstad, *Nonstoichiometry, Diffusion and Electrical Conductivity in Binary Metal Oxides*, Wiley-Interscience, (1972)

33. W. K. Chen and N. L. Peterson, *J. Phys. Chem. Solids* **33**, 881 (1972)

34. R. E. Carter and F. D. Richardson, *J. Metals* **6**, 1244 (1954)

35. W. K. Chen, N. L. Peterson and W. T. Reeves, *Phys. Rev.* **186**, 887 (1969)

36. M. L. Volpe and J. F. Reddy, *J. Chem. Phys.* **53**, 1117 (1970)

37. M. L. Volpe, N. L. Peterson and J. F. Reddy, *Phys. Rev.* **B3**, 1417 (1971)

38. A. D. Dalvi and D. E. Coates, *Oxid. of Metals* **3**, 203 (1971)

39. T. Narita and K. Nishida, *J. Japan Inst. Metals* **39**, 1152 (1975)

40. P. Mayer and W. W. Smeltzer, *J. Electrochem. Soc.* **121**, 538 (1974); **123**, 661 (1976)

41. A. D. Dalvi and W. W. Smeltzer, *J. Electrochem. Soc.* **121**, 386 (1974)

42. T. Narita and K. Nishida, *Denki. Kagaku* **43**, 443 (1975); **44**, 159 (1976)

43. B. D. Bastow, D. P. Whittle and G. C. Wood, *Corros. Sci.* **16**, 57 (1976)

44. D. P. Whittle, B. D. Bastow and G. C. Wood, *Trans. Japan Inst. Metals* **18**, 257 (1977)

45 D. J. Young, T. Narita and W. W. Smeltzer, *J. Electrochem. Soc.* **127**, 679 (1980)

46. T. Narita, K. Nishida and W. W. Smeltzer, *J. Electrochem. Soc.* **129**, 209 (1982)

47. D. P. Whittle, F. Gesmundo and F. Viani, *Oxid. of Metals* **16**, 81 (1981)

48. R. Dieckmann and H. Schmalzried, *Ber. Bunsen-Gesellschaft* **79**, 1109 (1975)

49. B. Fisher and D. S. Tannhauser, *J. Chem. Phys.* **44**, 1663 (1966)

50. K. Compaan and Y. Haven, *Trans. Faraday Soc.* **52**, 786 (1956)

51. R. Diechmann, *Z. Phys. Chem.* **105**, 47 (1977)

52. C. M. Osburn and R. W. Vest, *J. Phys. Chem. Solids* **32**, 1343 (1971)

53. J. M. Ferguson, Ph. D. Thesis, University of Manchester (1976)

54. "*The Oxide Handbook*", 2ed ed., G. V. Samsonov, IFI/Plenum, (1982)

55. R. E. Carter and F. D. Richardson, *J. Metals* **2**, 336 (1955)

56. S. Mrowec and K. Przybylski, *Rev. int. Htes. Temp. et Refract.* **14**, 243 (1977)

57. K. Fueki and J. B. Wagner Jr., *J. Electrochem Soc.* **112**, 384 (1965)

58. S. Mrowec, T. Walec and T. Werber, *Corro. Sci.* **6**, 287 (1966)

59. R. Hales, C.E.G.B. Report RD/B/N2165 (1971)

60. M. J. Graham and M. Cohen, *J. Electrochem Soc.* **119**, 879 (1972)

61. R. Hales and A. C. Hill, C.E.G.B. Report RE/B/N2341 (1972)

62. J. H. Perrow, W. W. Smeltzer and J. D. Embury, *Acta Met.* **16**, 1209 (1968)

63. R. A. Rapp, *Corrosion* **21**, 382 (1965)

64. J. H. Swisher, *Oxidation of Metals and Alloys*, ed. D. L. Douglass, Metals Park, Ohio (1971)

65. J. L. Meijering, *Adv. Mater. Sci.* **5**, 1 (1971)

66. C. Wagner, *Corros. Sci.* **8**, 889 (1968)

67. F. N. Rhines, *Trans. AIME* **137**, 246 (1940); *Corrosion* **4**, 15 (1947)

68. M. Badia, Doctoral Diss., Univ. Nancy, France (1969)

69. F. H. Hayes, Franz Muller and O. Kubaschewski, *J. Inst. Metals* **98**, 20 (1970)

VIII. FIGURE CAPTIONS

Figure 1 - Schematic alloy oxidation kinetics showing different stages in alloy oxidation.

Figure 2 - Schematic presentation of the relationship between scale morphologies on binary alloys which form completely misible oxides.

Figure 3 - Schematic diffusion profiles in the alloy and scale, illustrating the relevant coordinate systems and boundary conditions.

Figure 4 - Variation of D_{Co} and D_{Ni} with oxide composition, ξ, at different oxygen activities.

Figure 5 - Variation of $\partial \ln D_{Co}/\partial \xi$ and $\partial \ln D_{Co}/\partial \ln a_O$ as functions of ξ and a_O, and p as a function of ξ.

Figure 6 - A comparison between values of D^T_{Co}, D^T_{Ni} and p calculated from theory and those obtained experimentally by Chen and Peterson.[29]

Figure 7 - A comparison between experimentally measured D^T_{Co}, D^T_{Ni} and p values and those calculated using reduced equilibrium constants for the formation of vacancies in NiO.

Figure 8 - Schematic presentation of the experimental rig showing the balance and furnace assembly with indications of gas flows.

Figure 9 - Photograph of the experimental rig.

Figure 10 - Detailed schematic presentation of the furnace tube assembly showing the path of gas flow within the system.

Figure 11 - Kinetic curves obtained during oxidation of Ni-20%Co specimens under 1 atm. P_{O_2} and 6×10^{-9} atm. P_{O_2} at 1000°C.

Figure 12 - Parabolic plot of the kinetics of various Ni-Co alloys at 1 atm. P_{O_2} for 1000°C.

Figure 13 - Parabolic plot of the kinetics of various Ni-Co alloys at 6×10^{-9} atm. P_{O_2} for 1000°C.

Figure 14 - Variation of the parabolic rate constant, k_p, with composition for Ni-Co alloys oxidized under 1 atm. P_{O_2} and 6×10^{-9} atm. P_{O_2} at 1000°C.

Figure 15 - Optical micrograph of Ni-60%Co alloy which was oxidized at (a) P_{O_2} = 1 atm. for 100 minutes (b) P_{O_2} = 1 atm. for 15.5 hours (c) P_{O_2} = 6×10^{-9} atm. for 18 hours.

Figure 16 - SEM image of oxide surfaces on two Ni-20%Co alloys oxidized at 6×10^{-9} atm. P_{O_2} for (a), (c) 70 hours and (b), (d) 17 hours.

Figure 17 - SEM image showing difference in scale grain size near the scale-alloy interface and at the scale surface on a Ni-60%Co alloy oxidized at 6×10^{-9} atm. P_{O_2} for 360 hours.

Figure 18 - Optical micrograph of a cross-sectioned Ni-60%Co specimen oxidized at 6×10^{-9} atm. P_{O_2} for 18 hours showing typical morphology of internal oxide particles.

Figure 19 - Optical micrographs comparing depth of internal oxidation zone on two different alloys oxidized at 6×10^{-9} atm. P_{O_2} for 360 hours (a) Ni-40%Co (b) Ni-80%Co.

Figure 20 - Trace of electron beam during a microprobe analysis on a Ni-40%Co alloy oxidized at 6×10^{-9} atm. P_{O_2} for 360 hours.

Figure 21 - Composition of internal oxide precipitates as a function of penetration distance into the alloy obtained from microprobe analysis on Ni-20%Co, Ni-40%Co and Ni-60%Co alloys oxidized at 6×10^{-9} atm. P_{O_2} for 360 hours.

Figure 22 - Comparison between Co concentration profiles through Ni-60%Co alloys oxidized at 1 atm. P_{O_2} and at 6×10^{-9} atm. P_{O_2}.

Figure 23 - Co concentration profiles in y and λ space through Ni-10,20,40,60%Co alloys oxidized at 6×10^{-9} atm. P_{O_2} for 360 hours.

Figure 24 - Comparison between experimental and theoretical cation profiles in oxide scales formed at 1000°C on Ni-Co alloys contining 10.9%, 20.6%,38.4% and 80% Co respectively.

Figure 25 - Comparison between the parabolic rate constants, k_p, obtained experimentally and theoretically on alloys oxidized under 1 atm. O_2.

Figure 26 - Calculated total vacancy concentrations across the scales formed on four different Ni-Co alloys oxidized at 1 atm. P_{O_2}.

Figure 27 - Comparison between experimental and theoretical Co profiles through a Ni-38%Co alloy oxidized under 6×10^{-9} atm. oxygen.

Figure 28 - Comparison between the calculated total vacancy concentrations across the scales formed on Ni-38%Co alloys oxidized at 1 atm. P_{O_2} and at 6×10^{-9} atm. P_{O_2}.

Figure 29 - Diffusion coefficients of Co^{60} and Ni^{57} in $(Co_c Ni_{1-c})\ O$ crystals at 1445 and 1300°C in air. Plotted as log D vs c.

Figure 30 - Variation of the parabolic rate constant with composition for alloys oxidized at 6×10^{-9} atm. P_{O_2}. The dashed line represents the variation after the degree of Co enrichment in the scale has been corrected.

Figure 31 - Comparison between Co concentration in the alloy within the internal oxidation zone (solid line) and the Co concentration in the internal oxide precipitates (points) on a Ni-40%Co alloy oxidized at $P_{O_2}=6\times10^{-9}$ atm. for 360 hours.

Figure 32 - Relationship between Co concentration in the internal oxides and their surrounding alloys.

Figure 33 - Schematic illustration of the activity of cobalt in (a) the Ni-Co system and (b) the NiO-CoO system.

Figure 34 - A comparison between experimental cation profiles and theoretical profiles calculated in this work and in a previous paper[43] in oxide scales formed at 1000°C on Ni-Co alloys containing 10.9%, 38.4% and 80.0% Co respectively.

Figure 35 - Calculated oxygen activities and total vacancy concentrations across the scale formed on a Ni-38%Co alloy oxidized under 1 atm. O_2 at 1000°C.

Figure 36 - Comparison between experimental and theoretical Co concentration profiles through a Ni-38%Co alloy oxidized at 6×10^{-9} atm. P_{O_2}, while allowing for the calculated oxygen activity at the scale-alloy interface to be one order of magnitude higher than its equilibrium value.

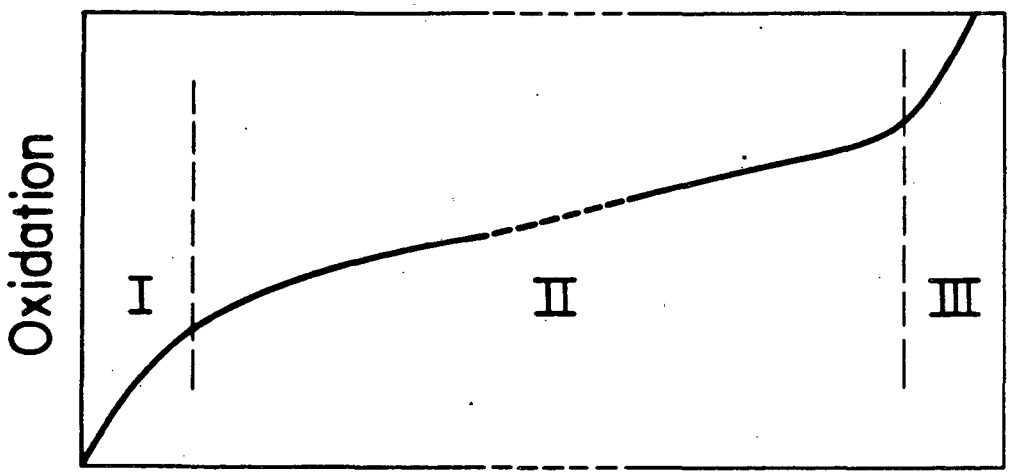

I: Transient stage: Ratio of cations in scale approximately same as that in alloy

II: Steady state: Oxide morphology and composition determined by diffusion and thermodynamics of oxide/alloy system

III: Breakaway: Initiated by mechanical factors: eventually scale contains alloying components in original alloy ratio

XBL 833-1410

Figure 1 - Schematic alloy oxidation kinetics showing different stages in alloy oxidation.

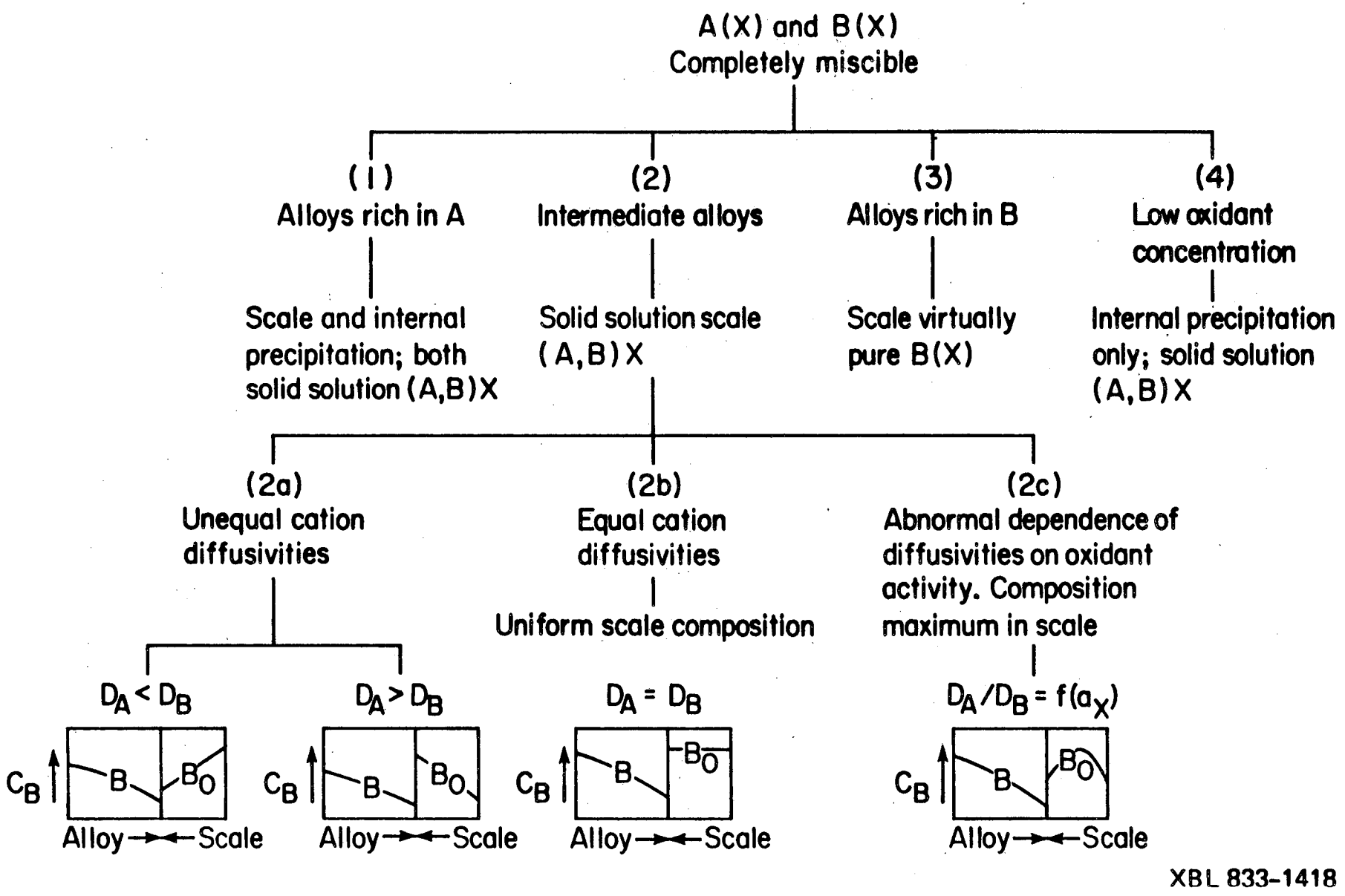

Figure 2 - Schematic presentation of the relationship between scale morphologies on binary alloys which form completely misible oxides.

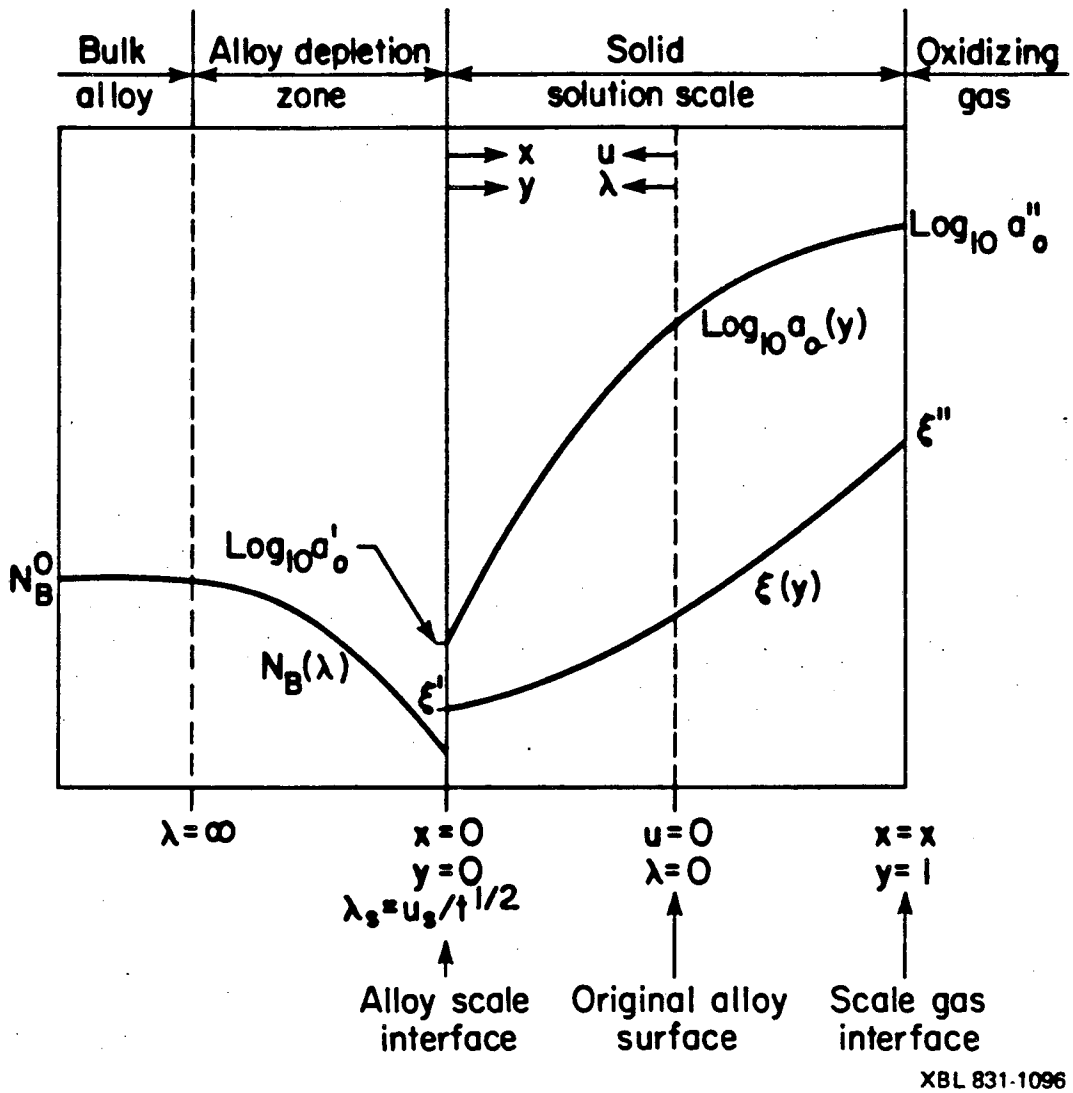

Figure 3 - Schematic diffusion profiles in the alloy and scale, illustrating the relevant coordinate systems and boundary conditions.

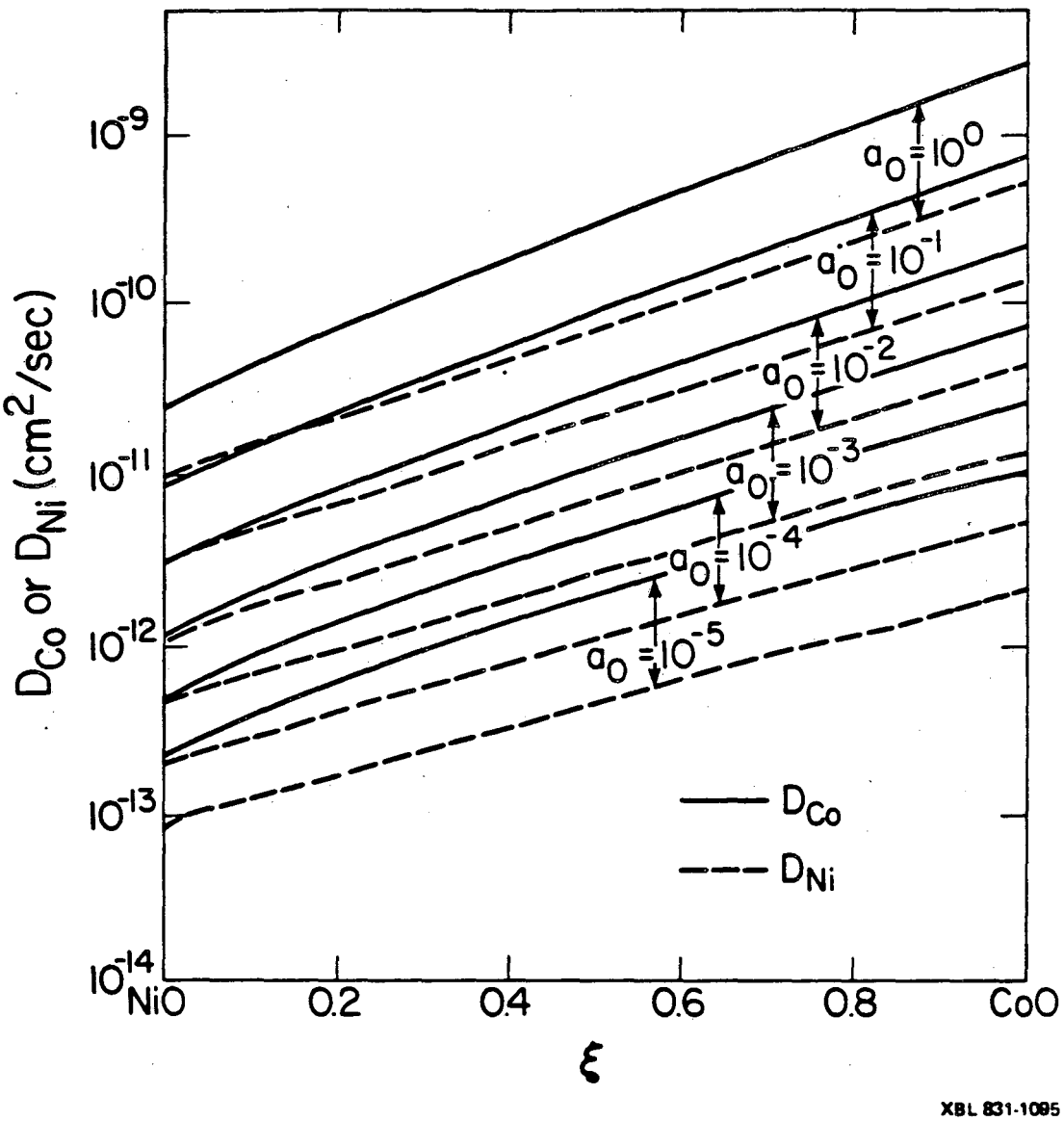

Figure 4 - Variation of D_{Co} and D_{Ni} with oxide composition, ξ, at different oxygen activities.

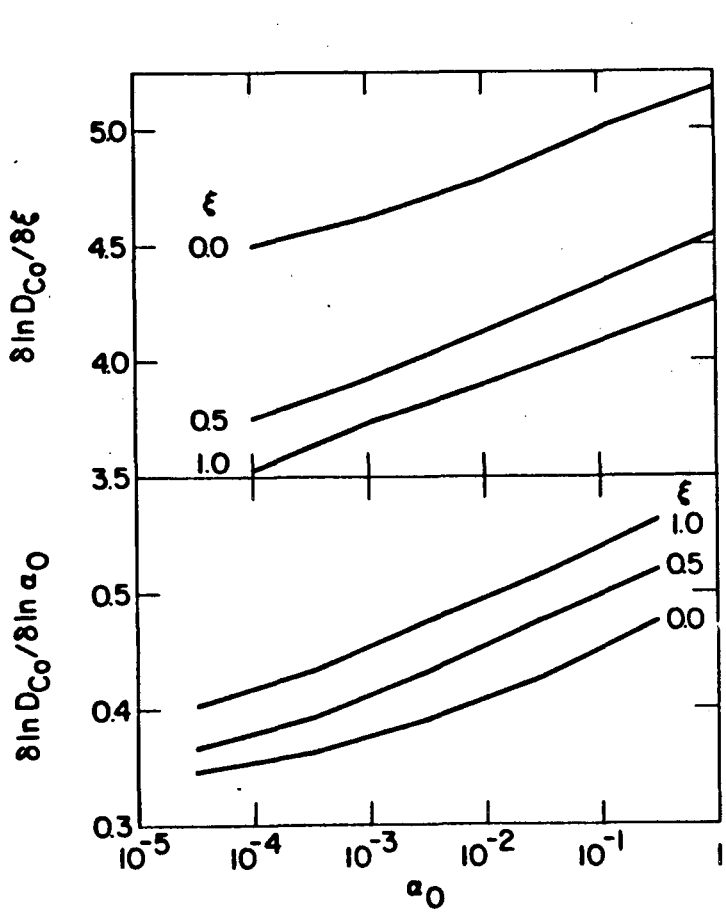

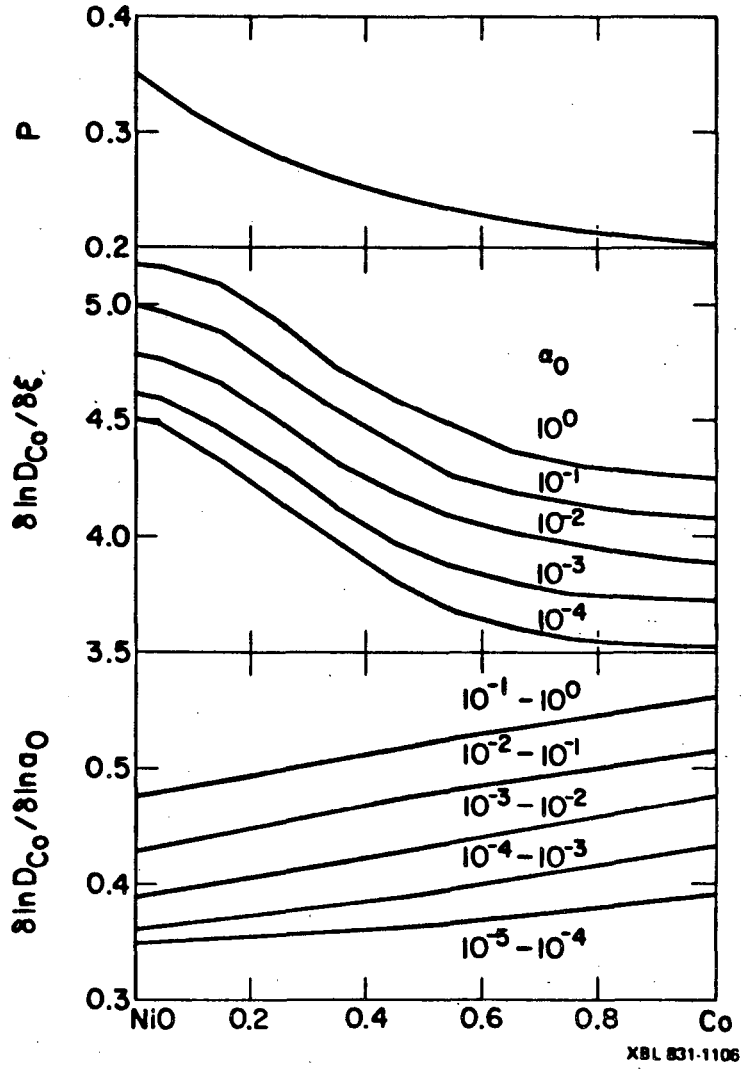

Figure 5 - Variation of $\partial \ln D_{Co}/\partial \xi$ and $\partial \ln D_{Co}/\partial \ln a_O$ as functions of ξ and a_O, and p as a function of ξ.

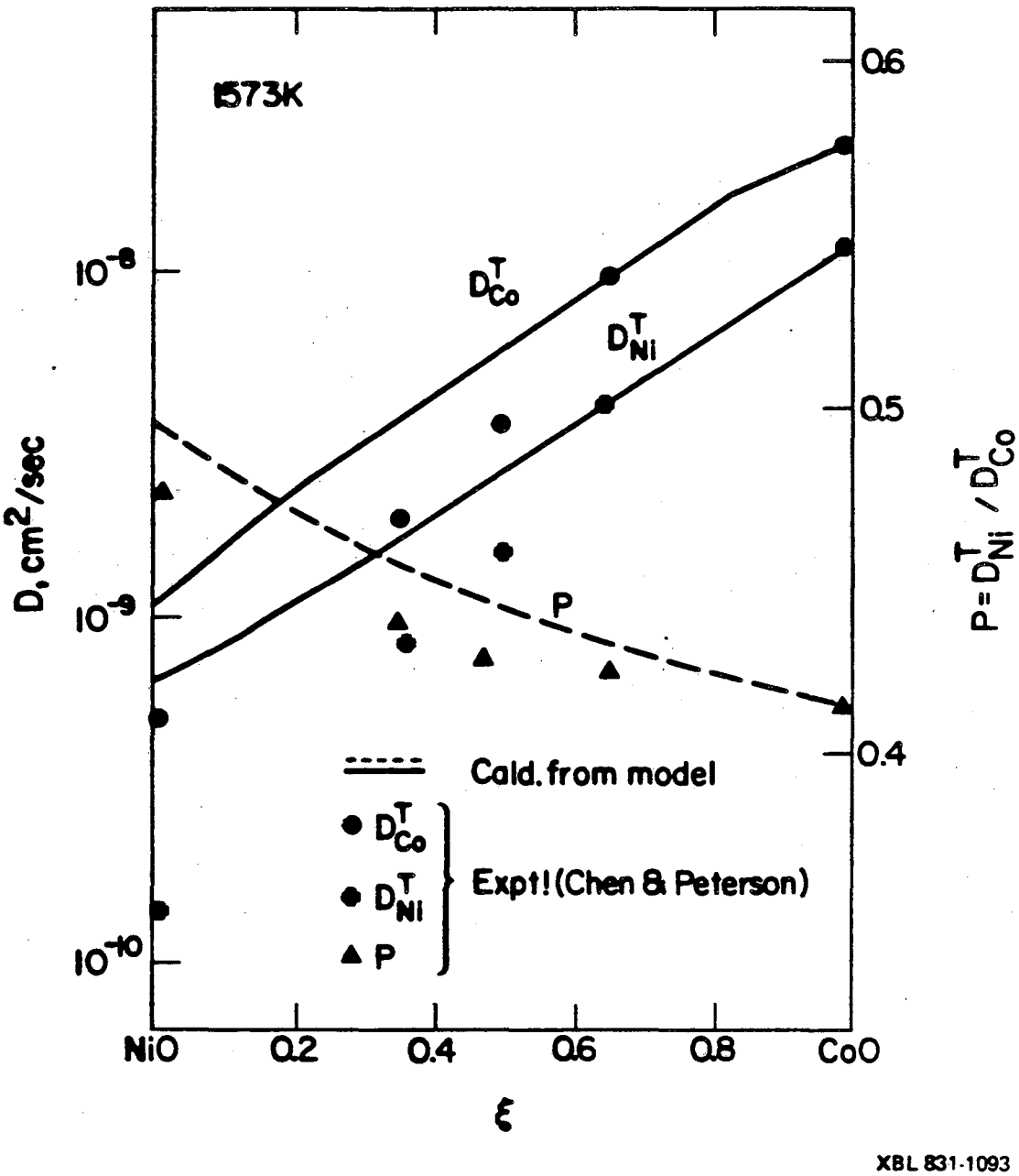

Figure 6 - A comparison between values of D_{α}^{T}, D_{M}^{T} and p calculated from theory and those obtained experimentally by Chen and Peterson.[29]

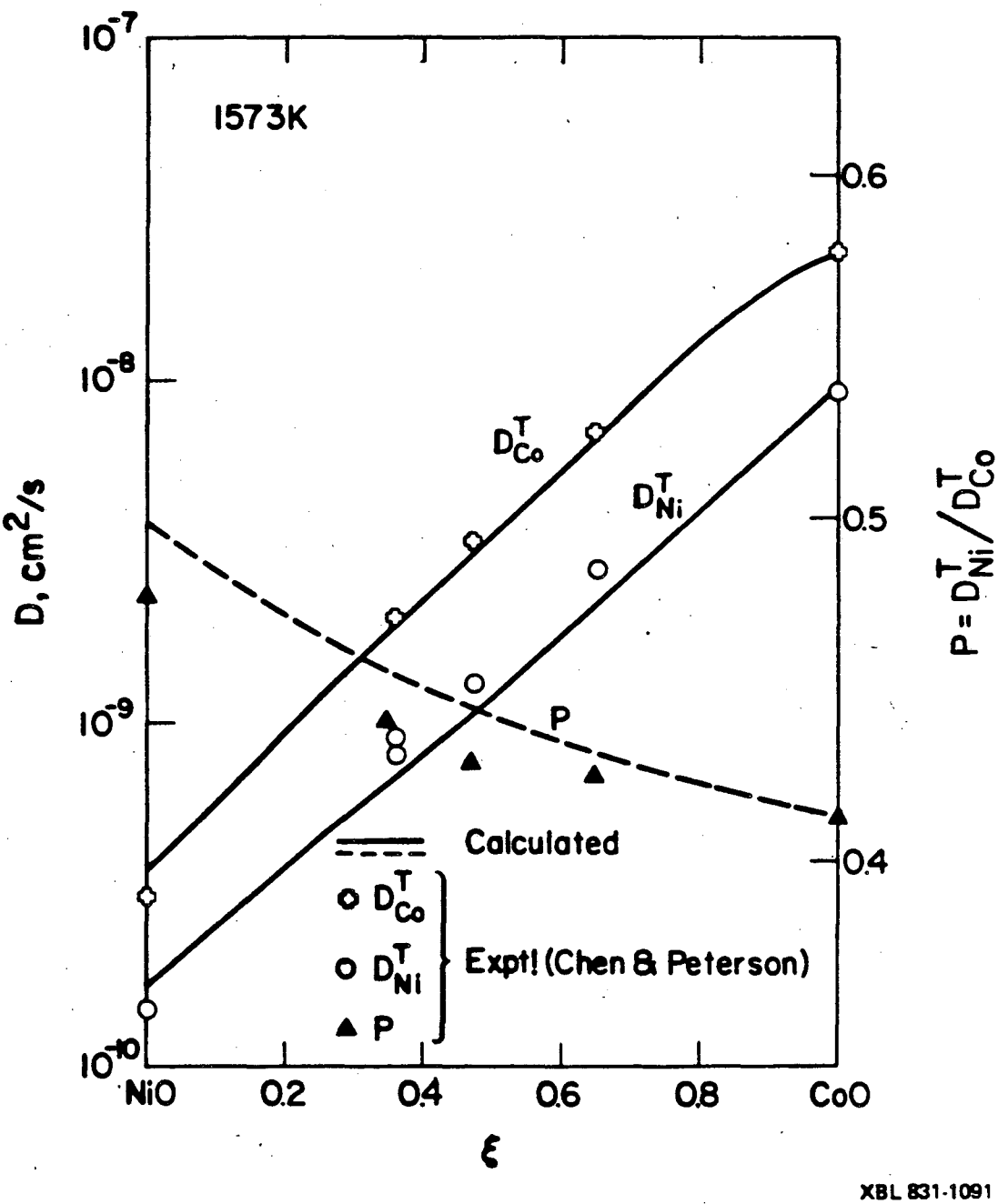

Figure 7 - A comparison between experimentally measured D^T_{Co}, D^T_{Ni} and p values and those calculated using reduced equilibrium constants for the formation of vacancies in NiO.

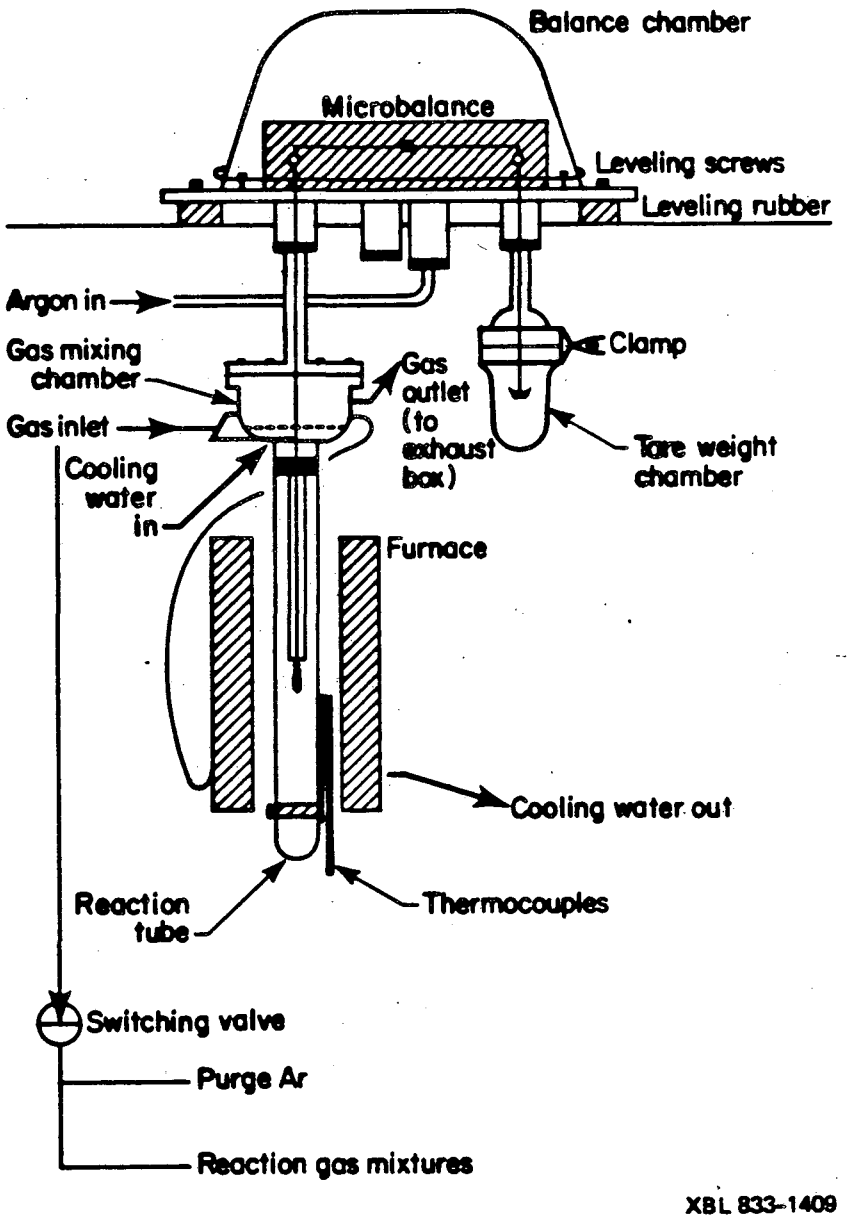

Figure 8 - Schematic presentation of the experimental rig showing the balance and furnace assembly with indications of gas flows.

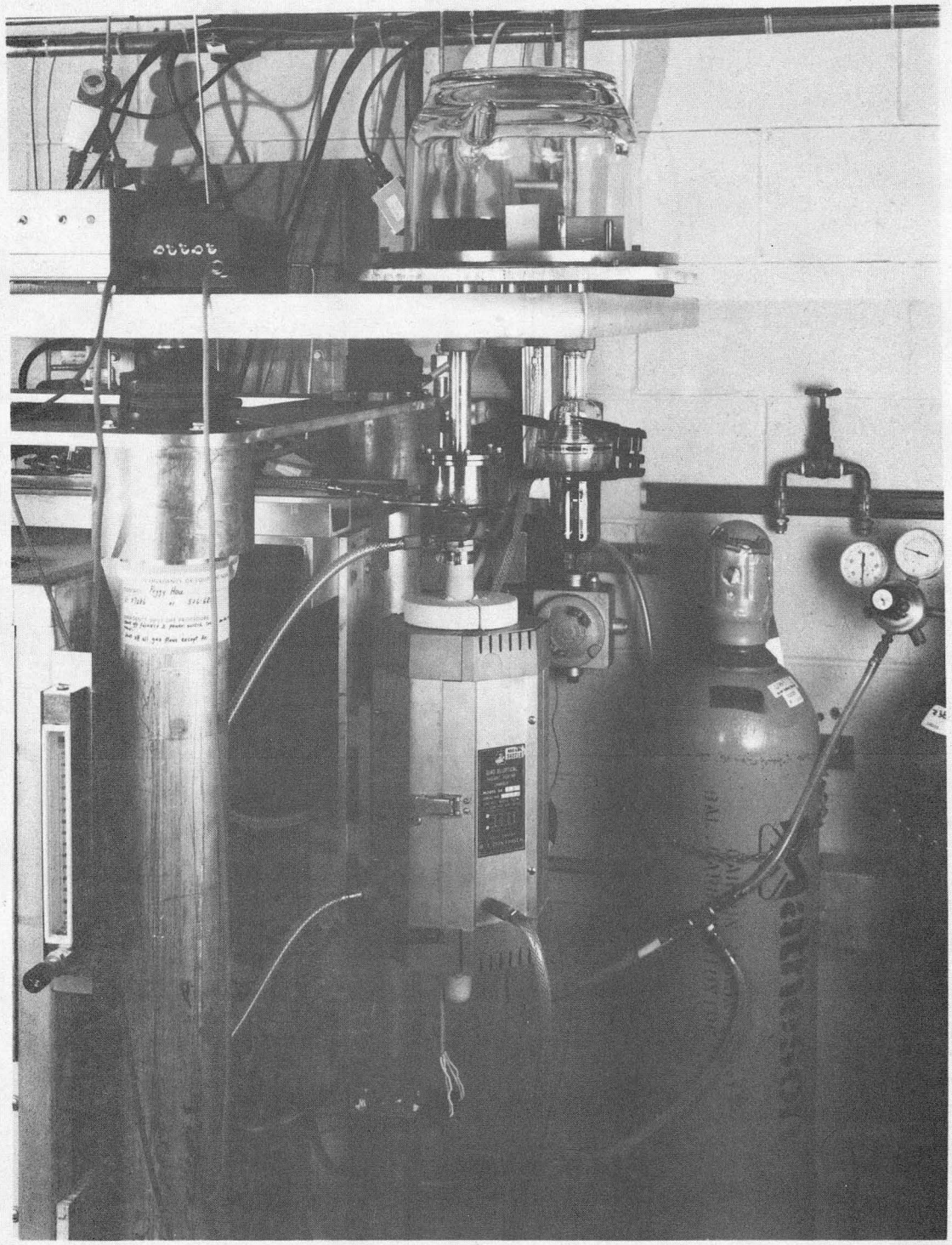

XBB 831-656

Figure 9

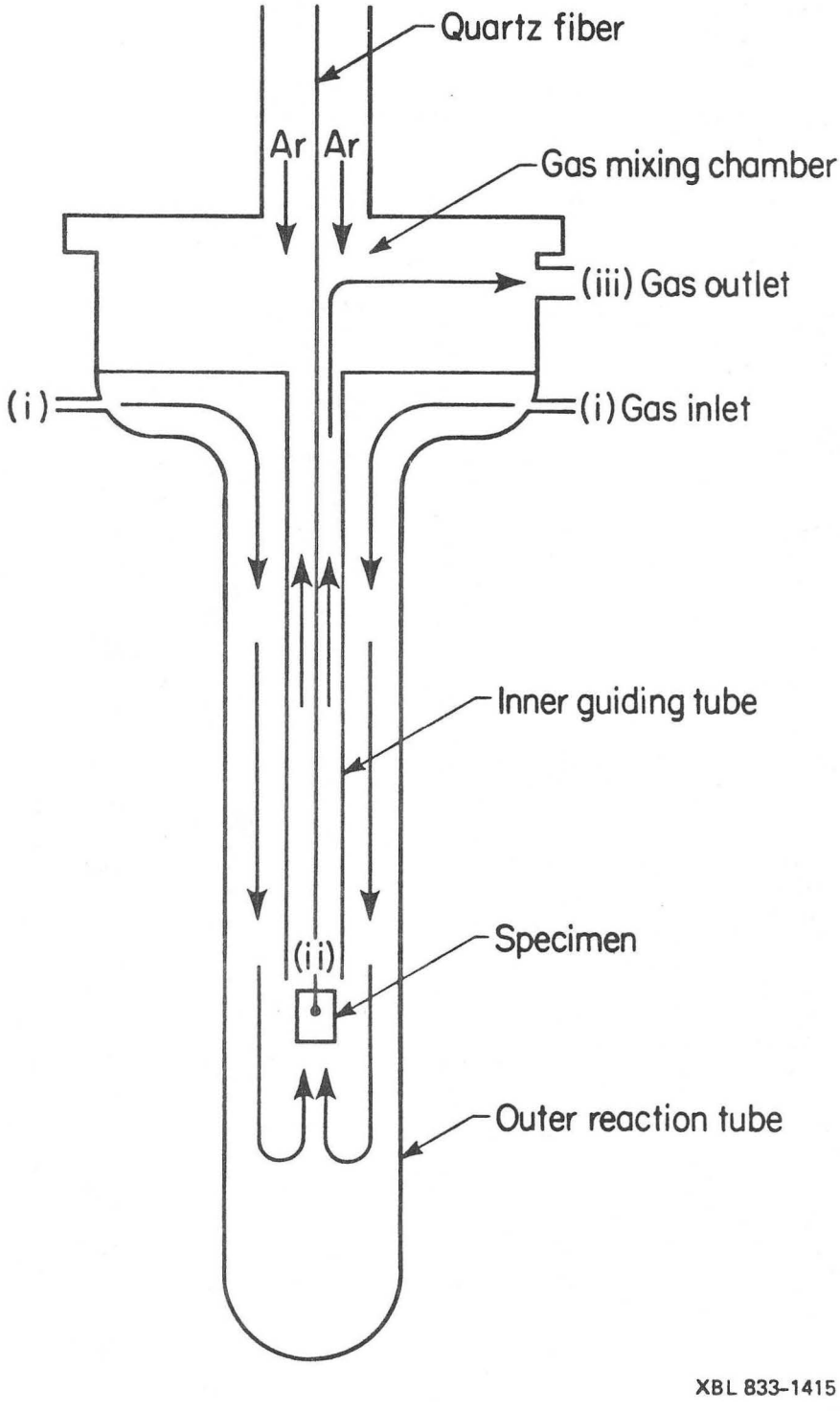

Figure 10 - Detailed schematic presentation of the furnace tube assembly showing the path of gas flow within the system.

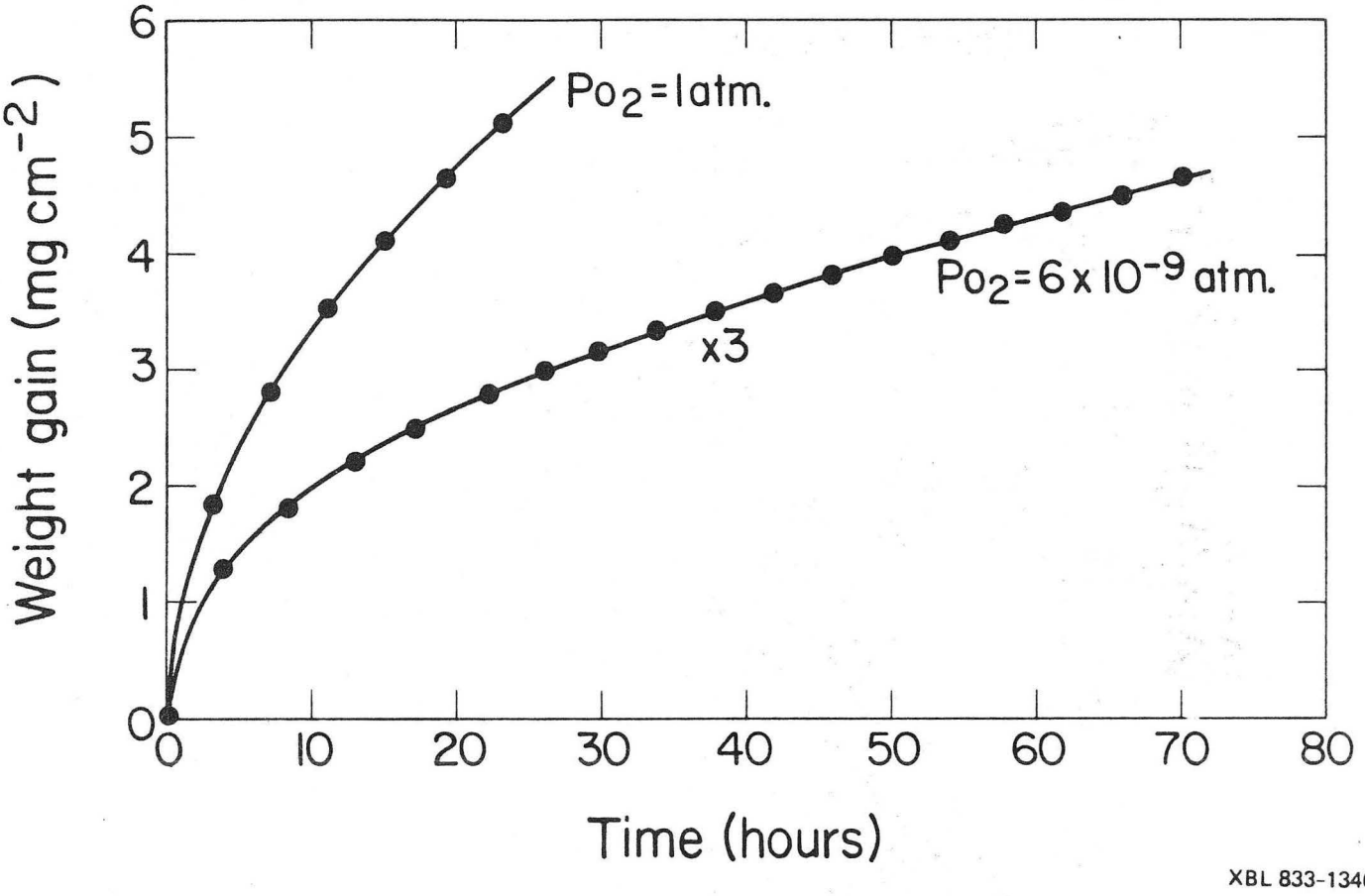

Figure 11 - Kinetic curves obtained during oxidation of Ni-20%Co specimens under 1 atm. P_{O_2} and 6×10^{-9} atm. P_{O_2} at 1000°C.

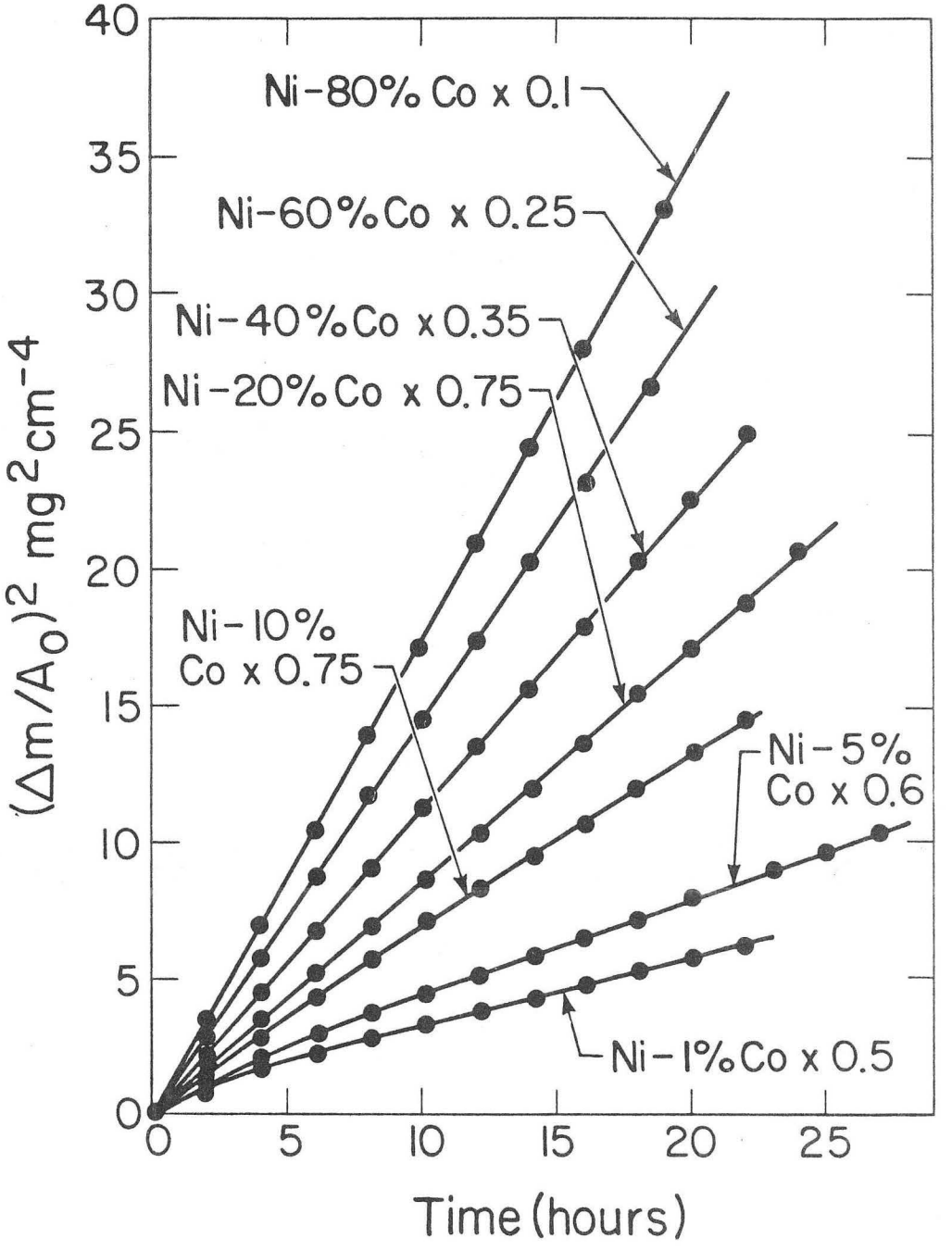

Figure 12 - Parabolic plot of the kinetics of various Ni-Co alloys at 1 atm. P_{O_2} for 1000°C.

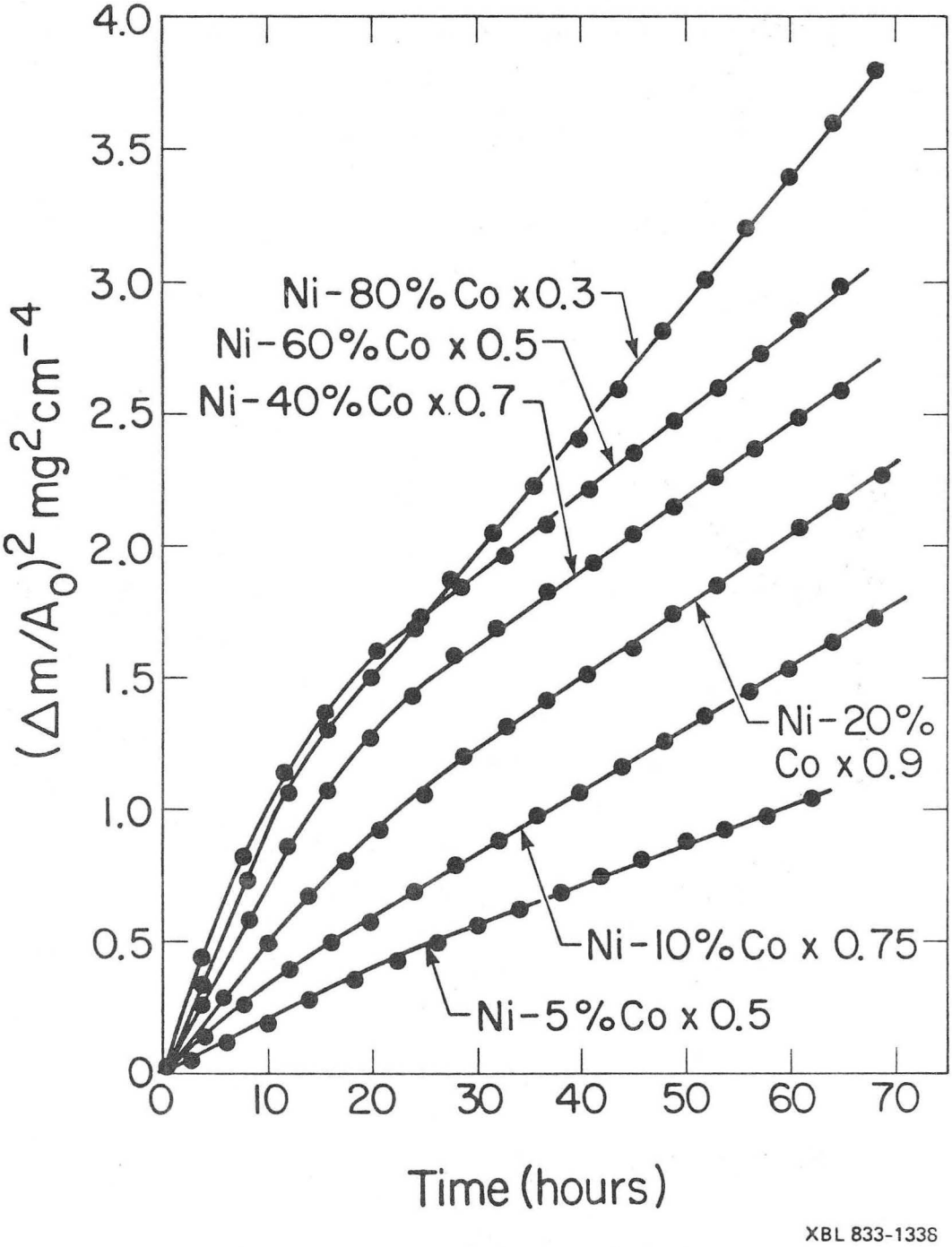

Figure 13 - Parabolic plot of the kinetics of various Ni-Co alloys at 6×10^{-9} atm. P_{O_2} for 1000°C.

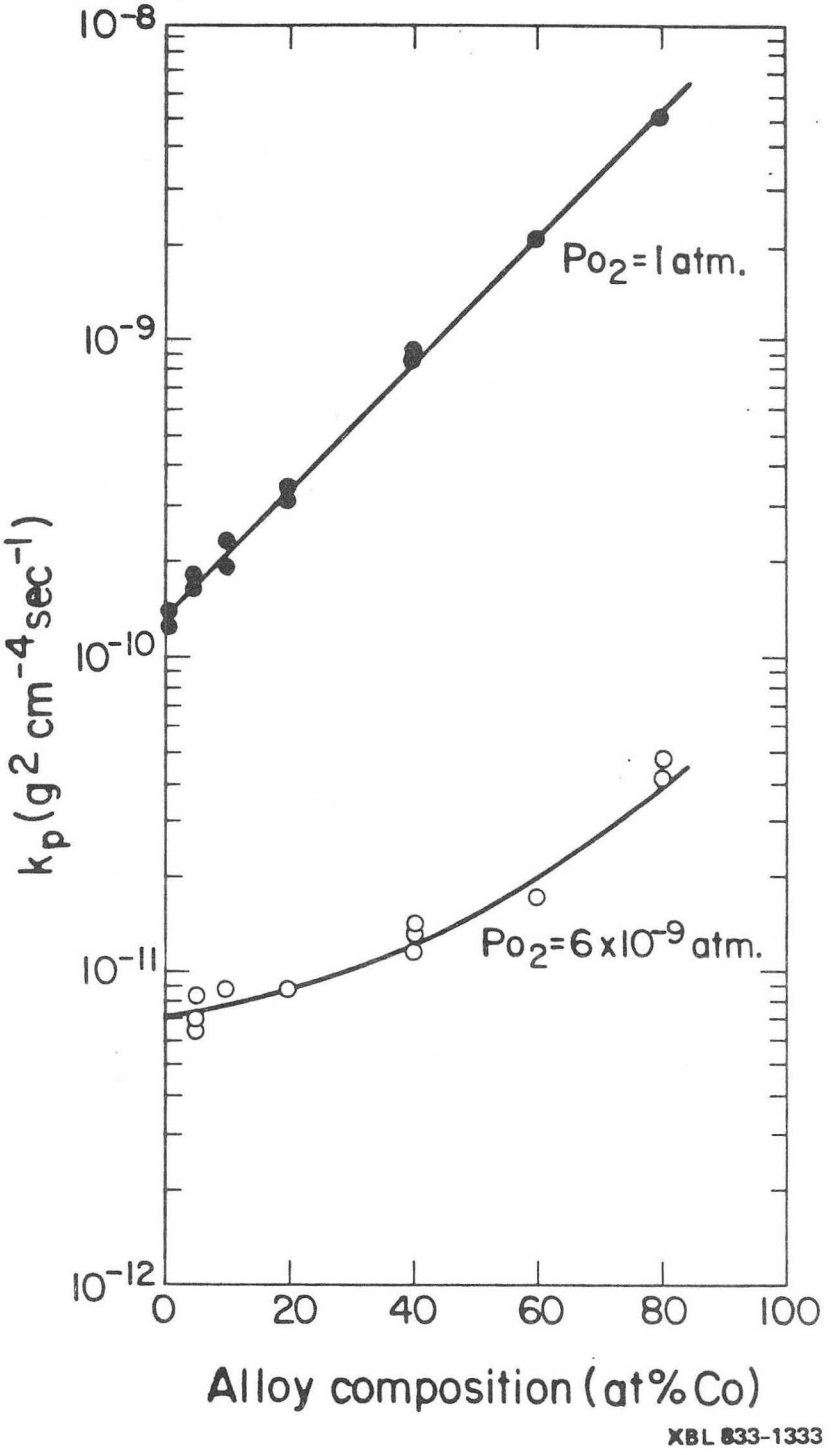

Figure 14 - Variation of the parabolic rate constant, k_p, with composition for Ni-Co alloys oxidized under 1 atm. P_{O_2} and 6×10^{-9} atm. P_{O_2} at 1000° C.

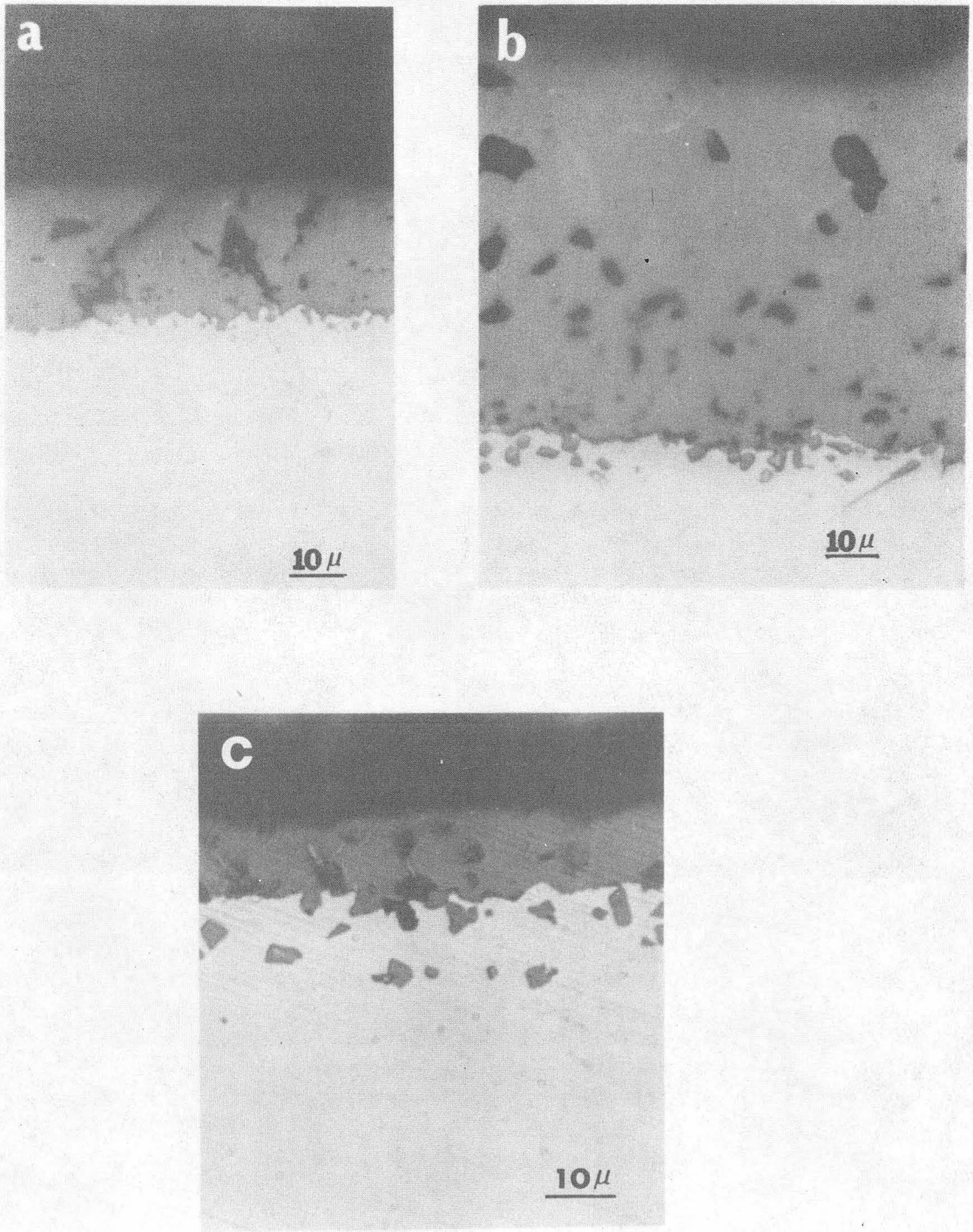

Figure 15

XBB 834-3295

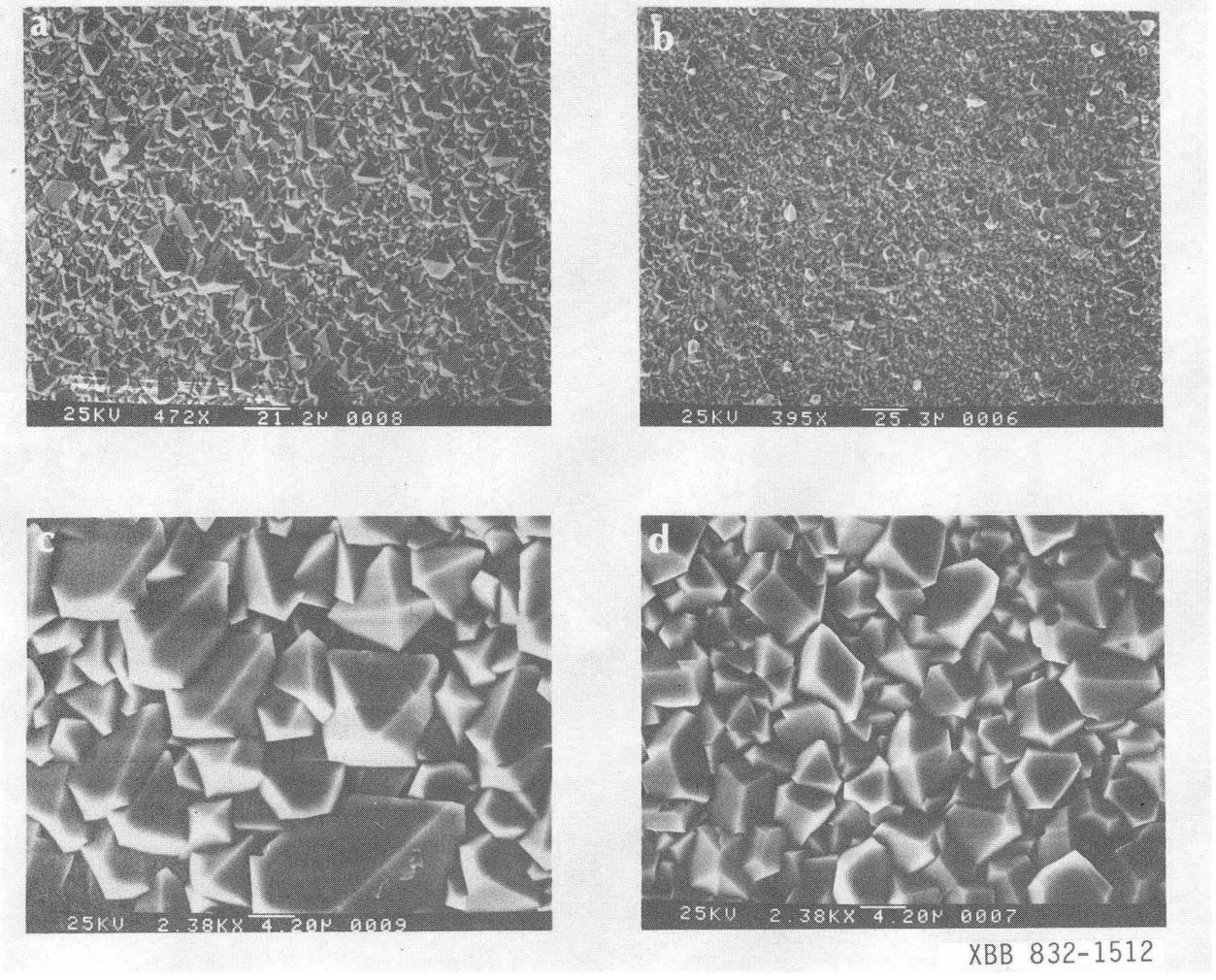

XBB 832-1512

Figure 16

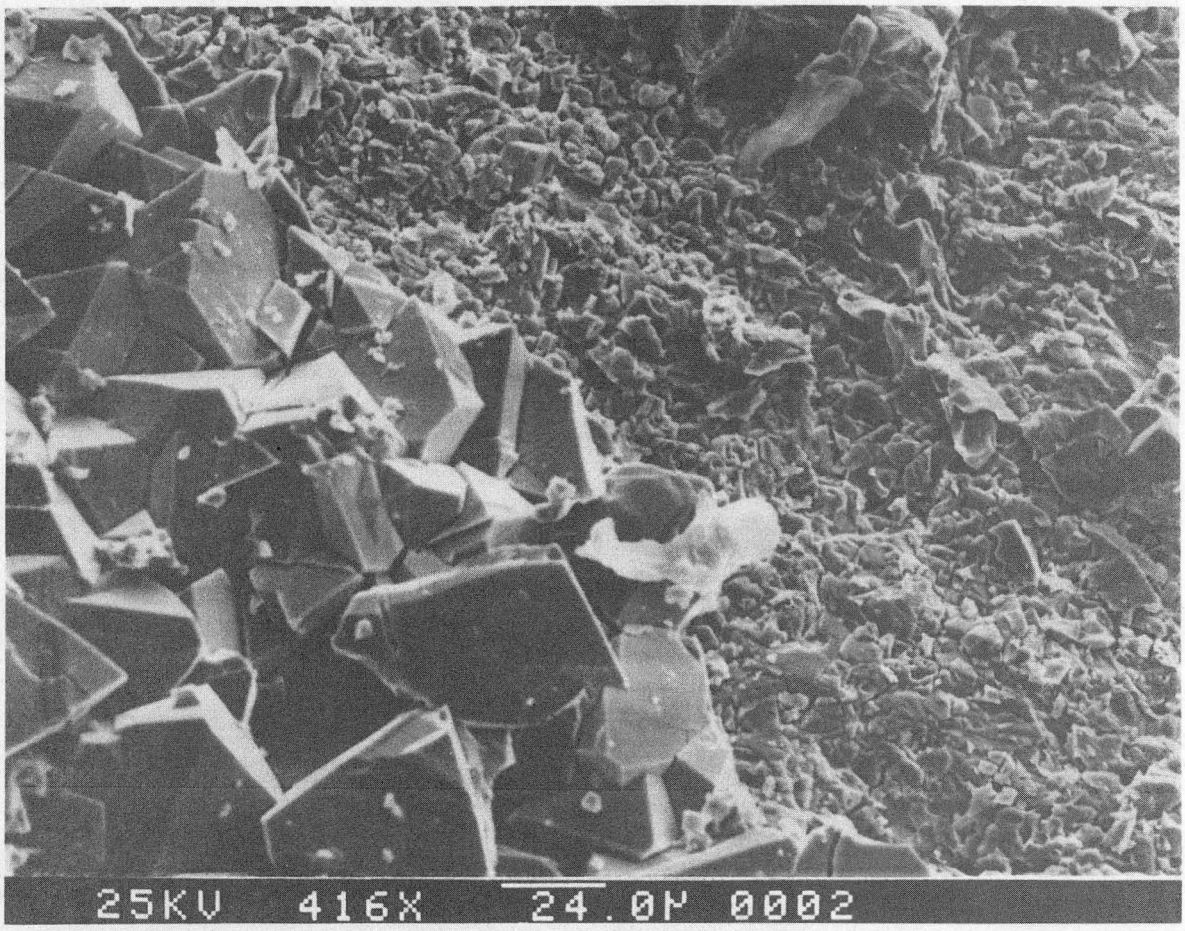

XBB 832-1510

Figure 17

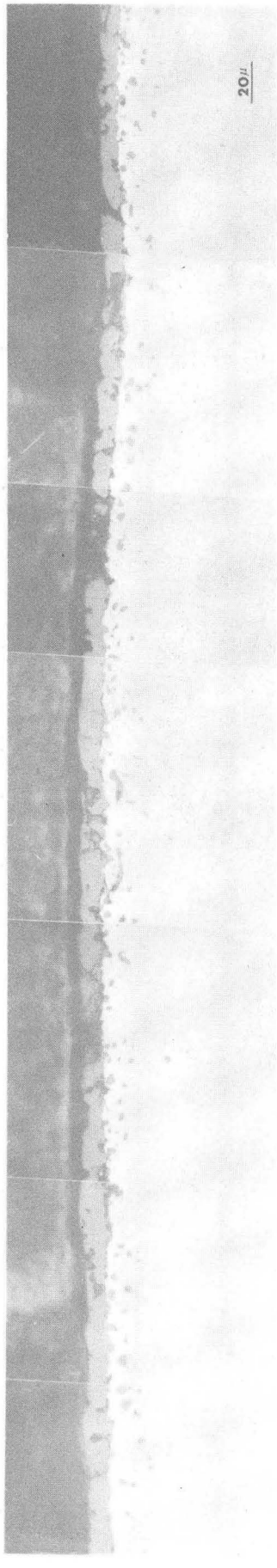

XBB 834-3296

Figure 18

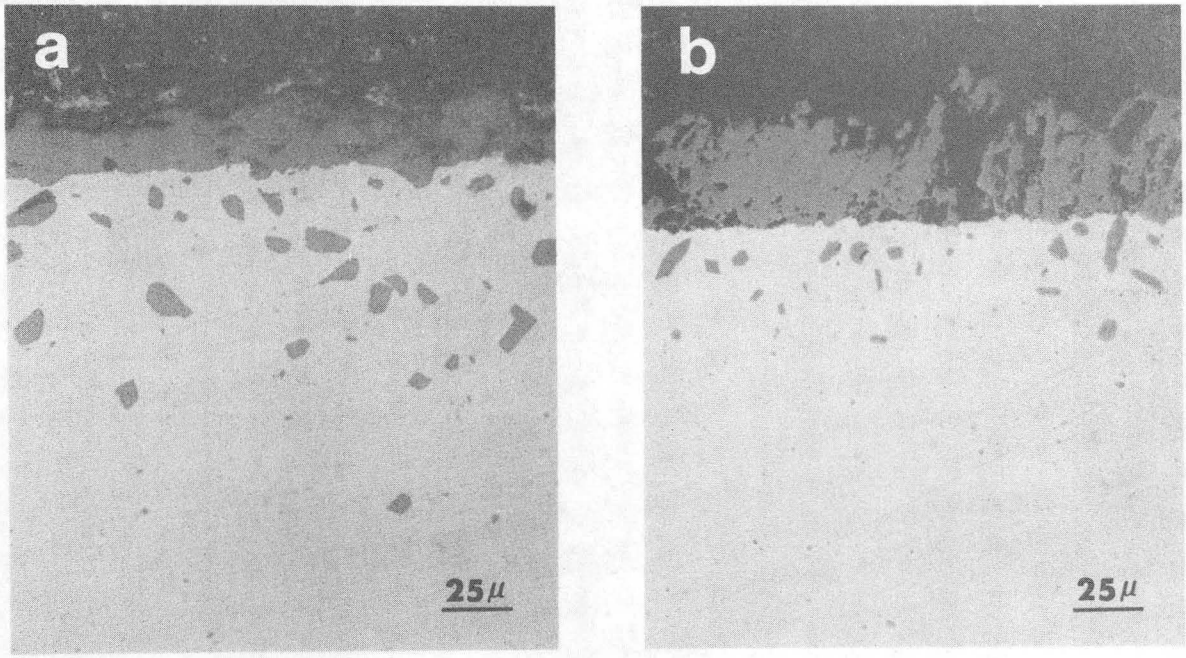

XBB 834-3294

Figure 19

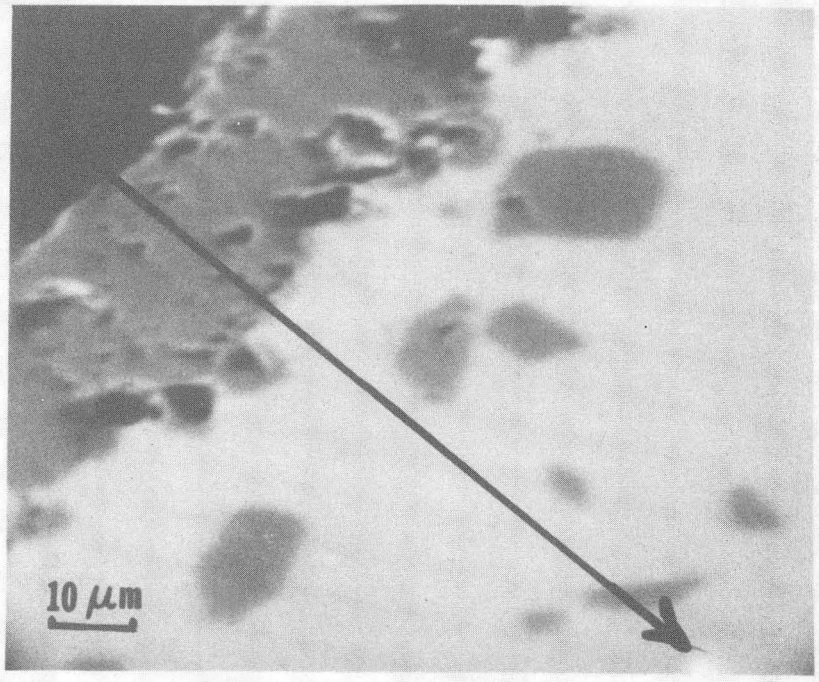

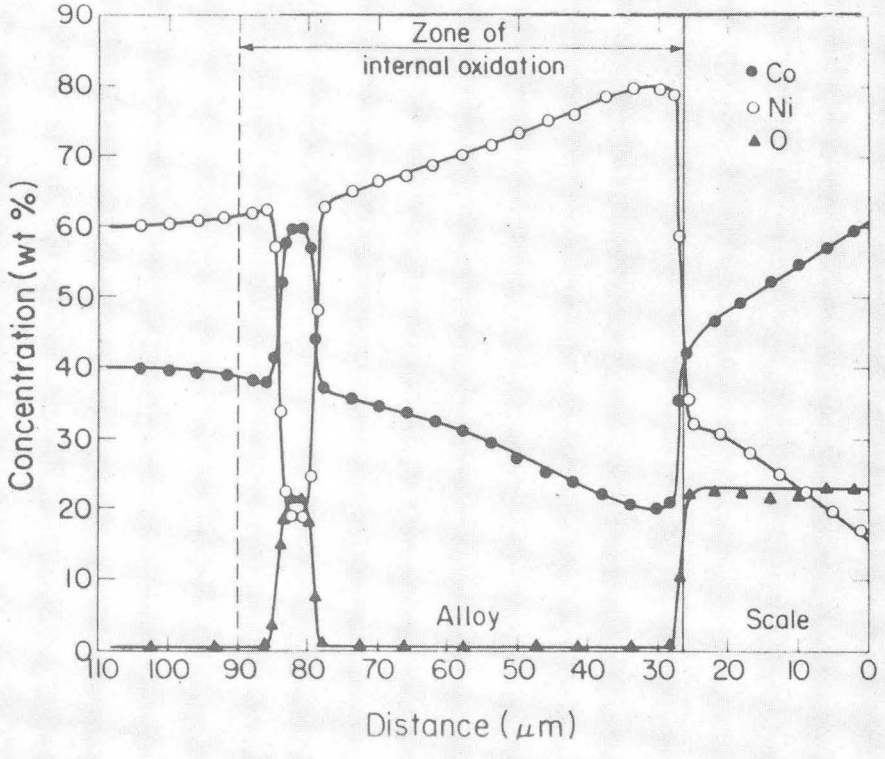

Figure 20

XBB 833-2209

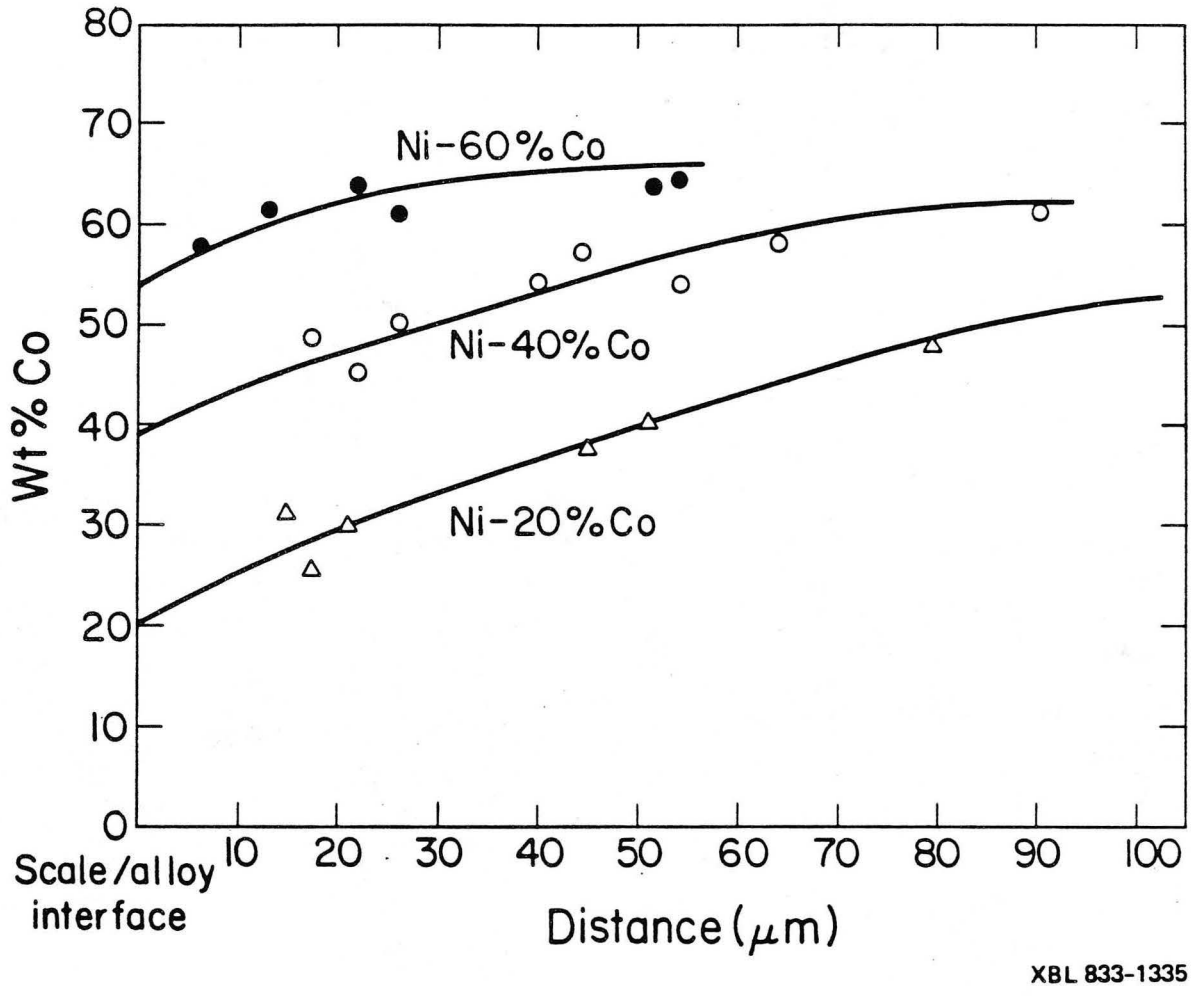

XBL 833-1335

Figure 21 - Composition of internal oxide precipitates as a function of penetration distance into the alloy obtained from microprobe analysis on Ni-20%Co, Ni-40%Co and Ni-60%Co alloys oxidized at 6×10^{-9} atm. P_{O_2} for 360 hours.

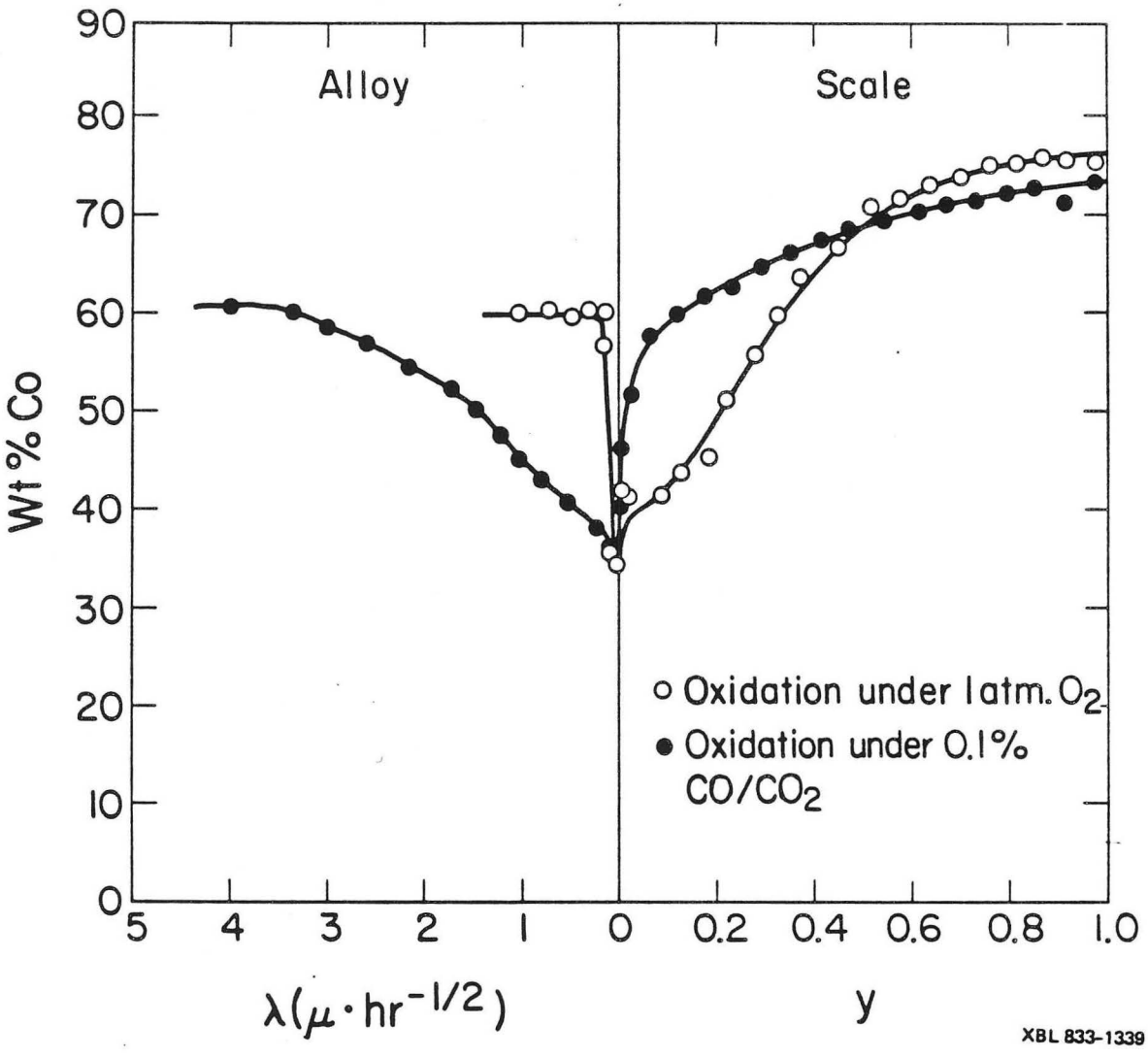

Figure 22 - Comparison between Co concentration profiles through Ni-60%Co alloys oxidized at 1 atm. P_{O_2} and at 6×10^{-9} atm. P_{O_2}.

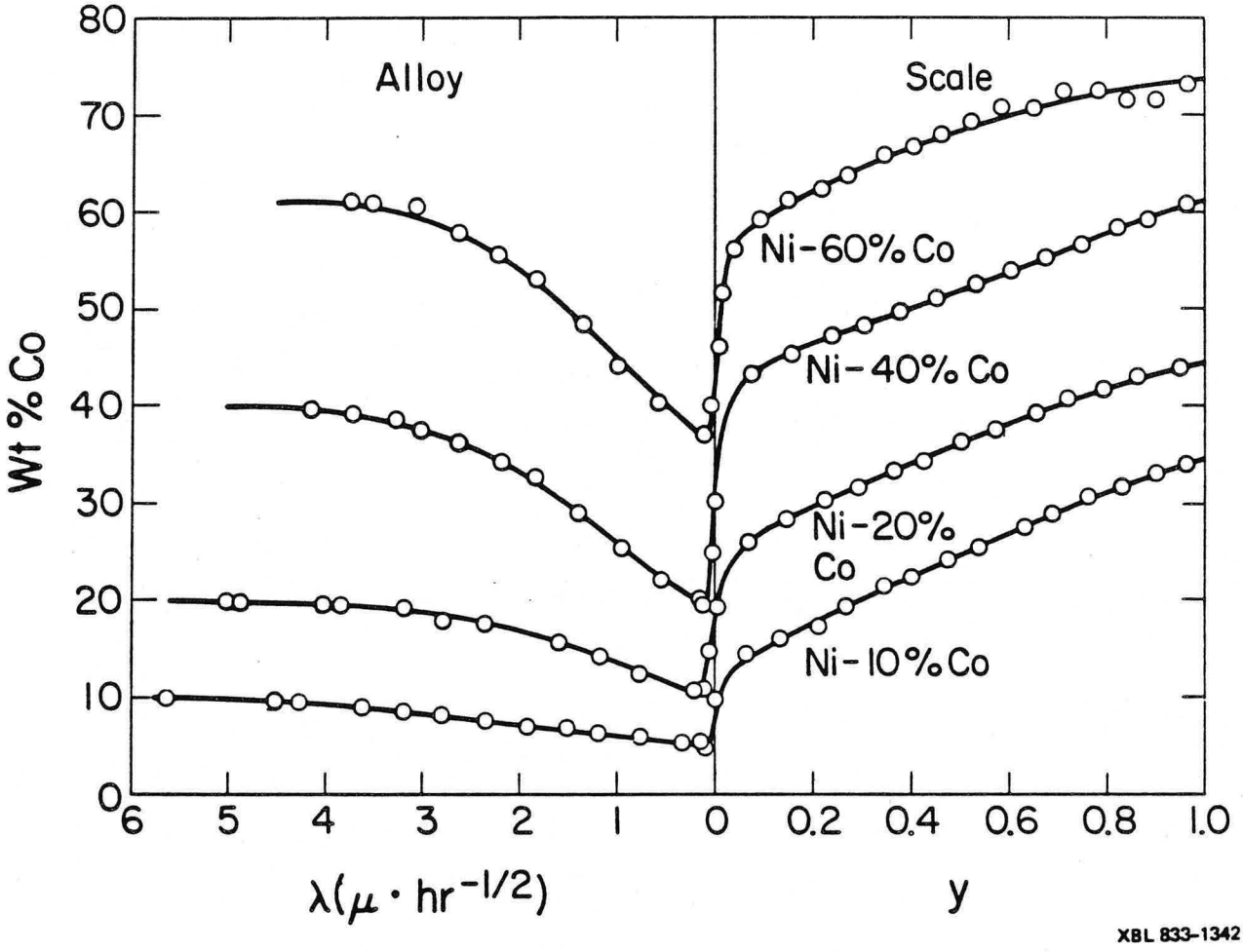

Figure 23 - Co concentration profiles in y and λ space through Ni-10,20,40,60%Co alloys oxidized at 6×10^{-9} atm. P_{O_2} for 360 hours.

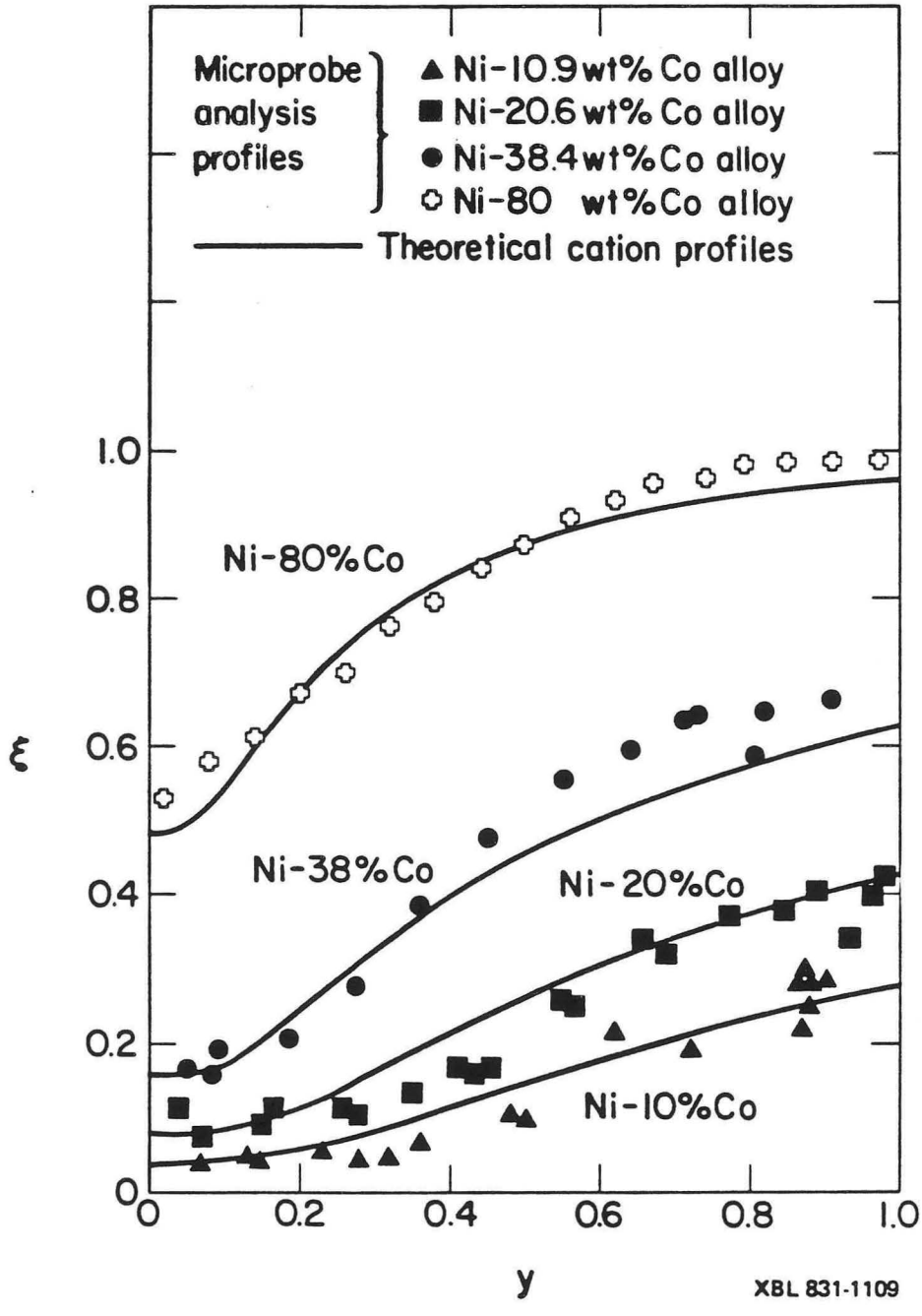

Figure 24 - Comparison between experimental and theoretical cation profiles in oxide scales formed at 1000°C on Ni-Co alloys contining 10.9%, 20.6%,38.4% and 80% Co respectively.

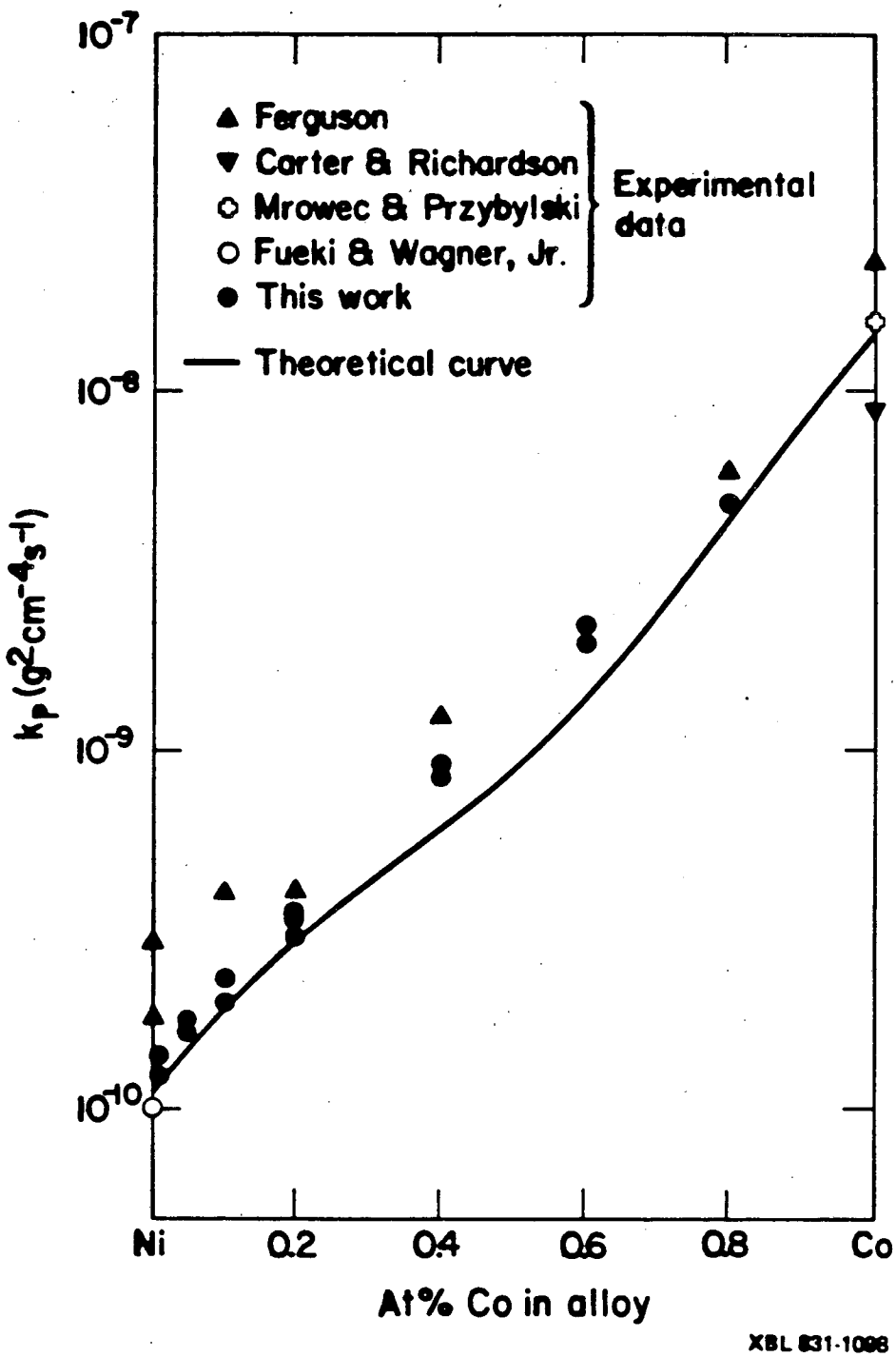

Figure 25 - Comparison between the parabolic rate constants, k_p, obtained experimentally and theoretically on alloys oxidized under 1 atm. O_2.

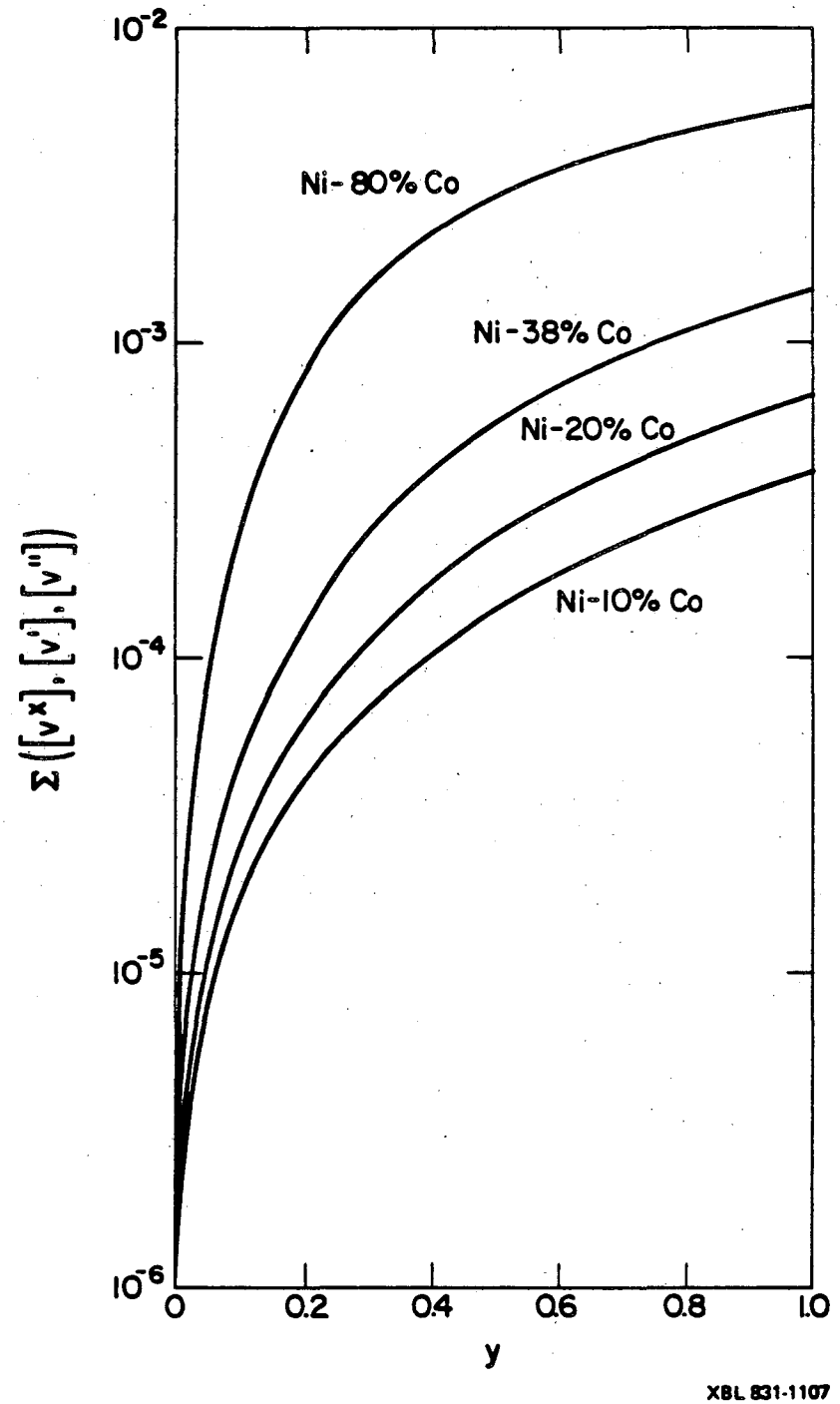

Figure 26 - Calculated total vacancy concentrations across the scales formed on four different Ni-Co alloys oxidized at 1 atm. P_{O_2}.

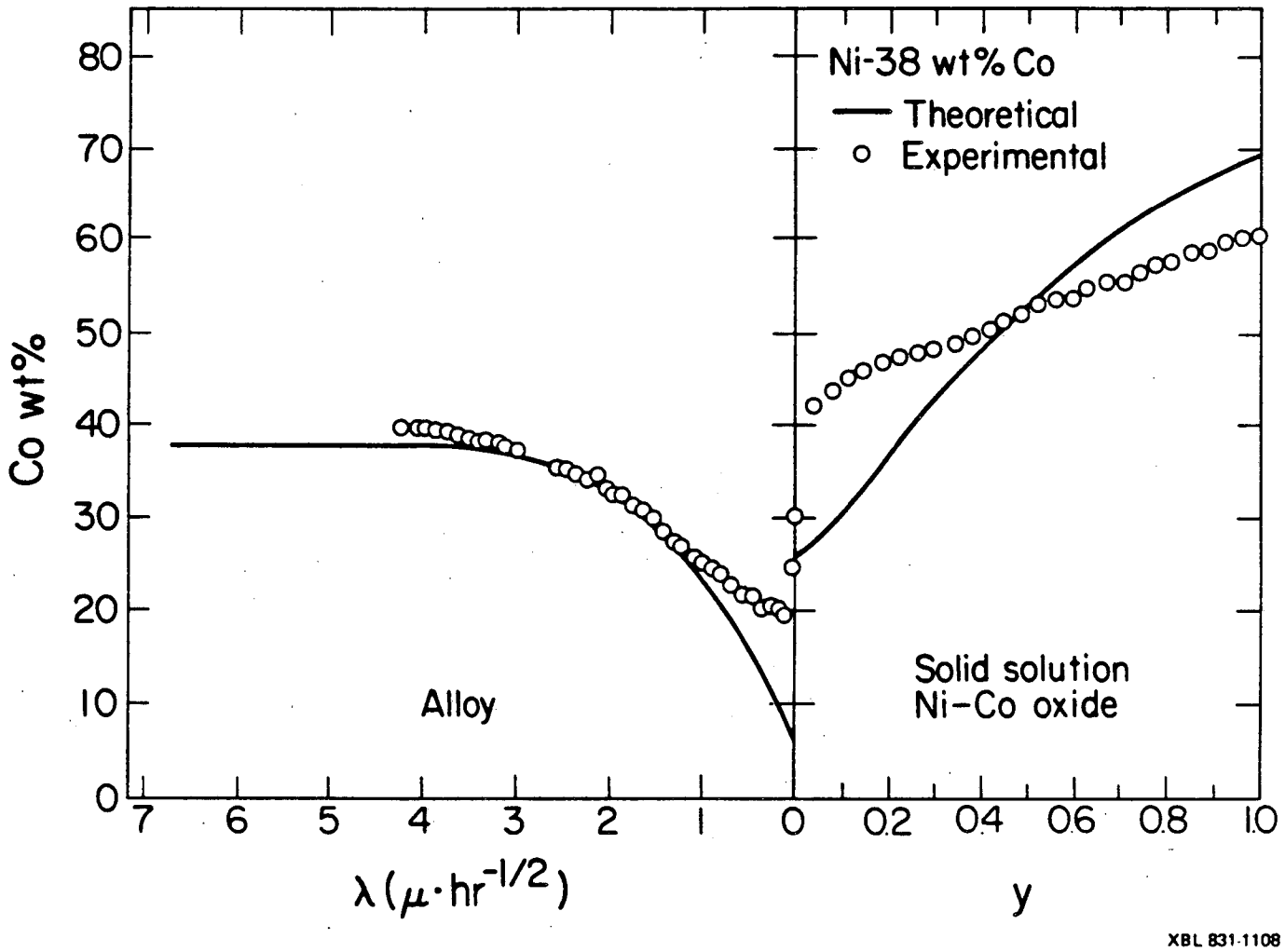

Figure 27 - Comparison between experimental and theoretical Co profiles through a Ni-38%Co alloy oxidized under 6×10^{-9} atm. oxygen.

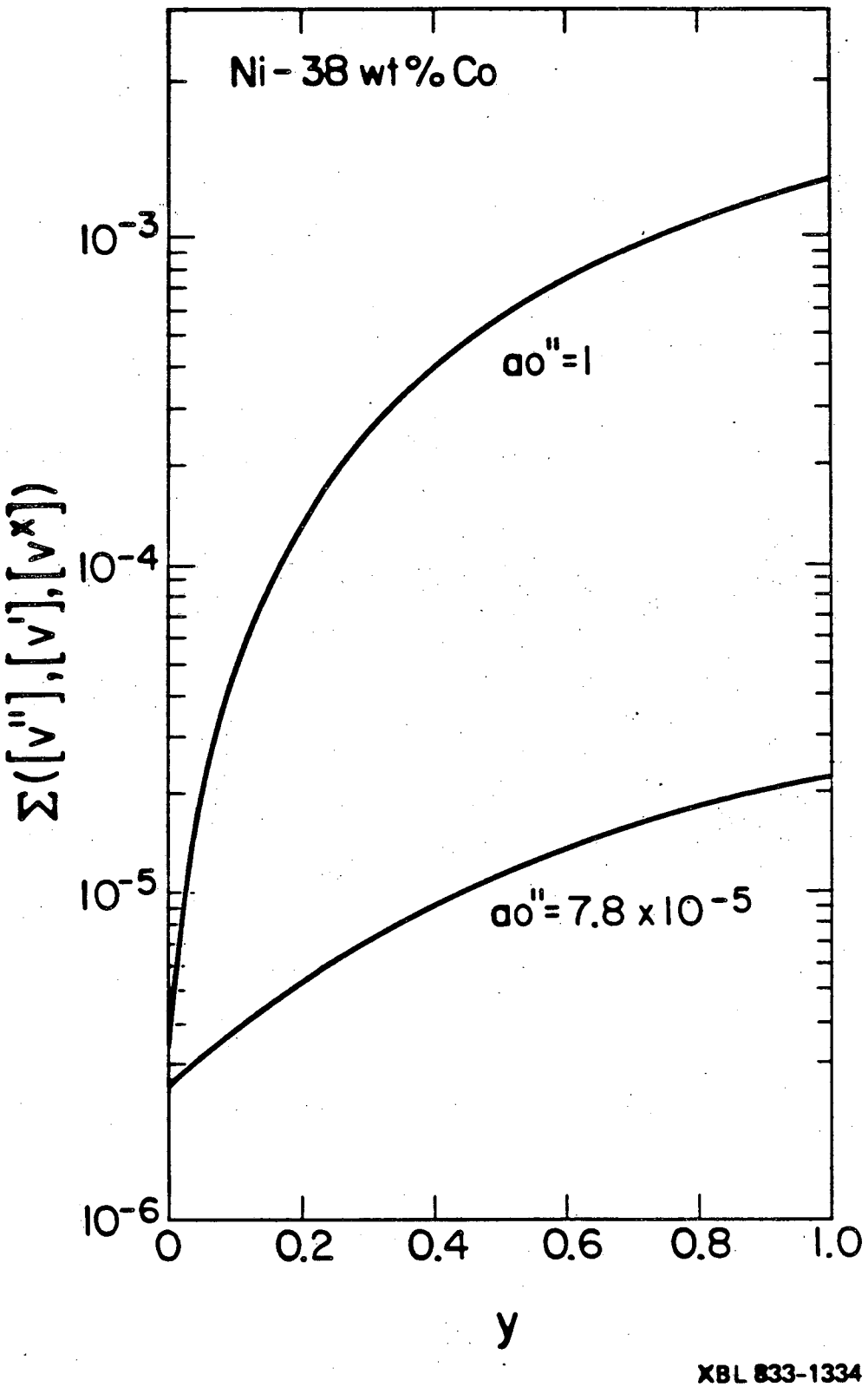

Figure 28 - Comparison between the calculated total vacancy concentrations across the scales formed on Ni-38%Co alloys oxidized at 1 atm. P_{O_2} and at 6×10^{-9} atm. P_{O_2}.

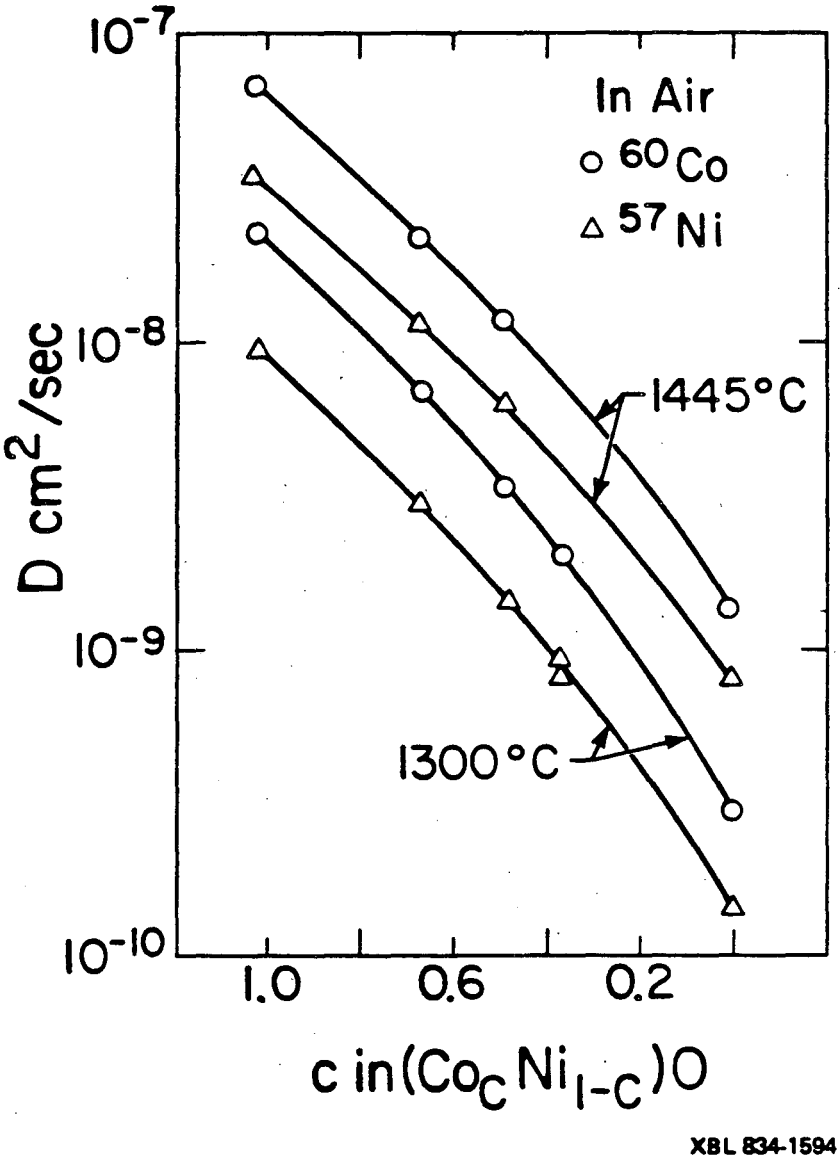

Figure 29 - Diffusion coefficients of Co^{60} and Ni^{57} in $(Co_c Ni_{1-c})\ O$ crystals at 1445 and 1300°C in air. Plotted as log D vs c.

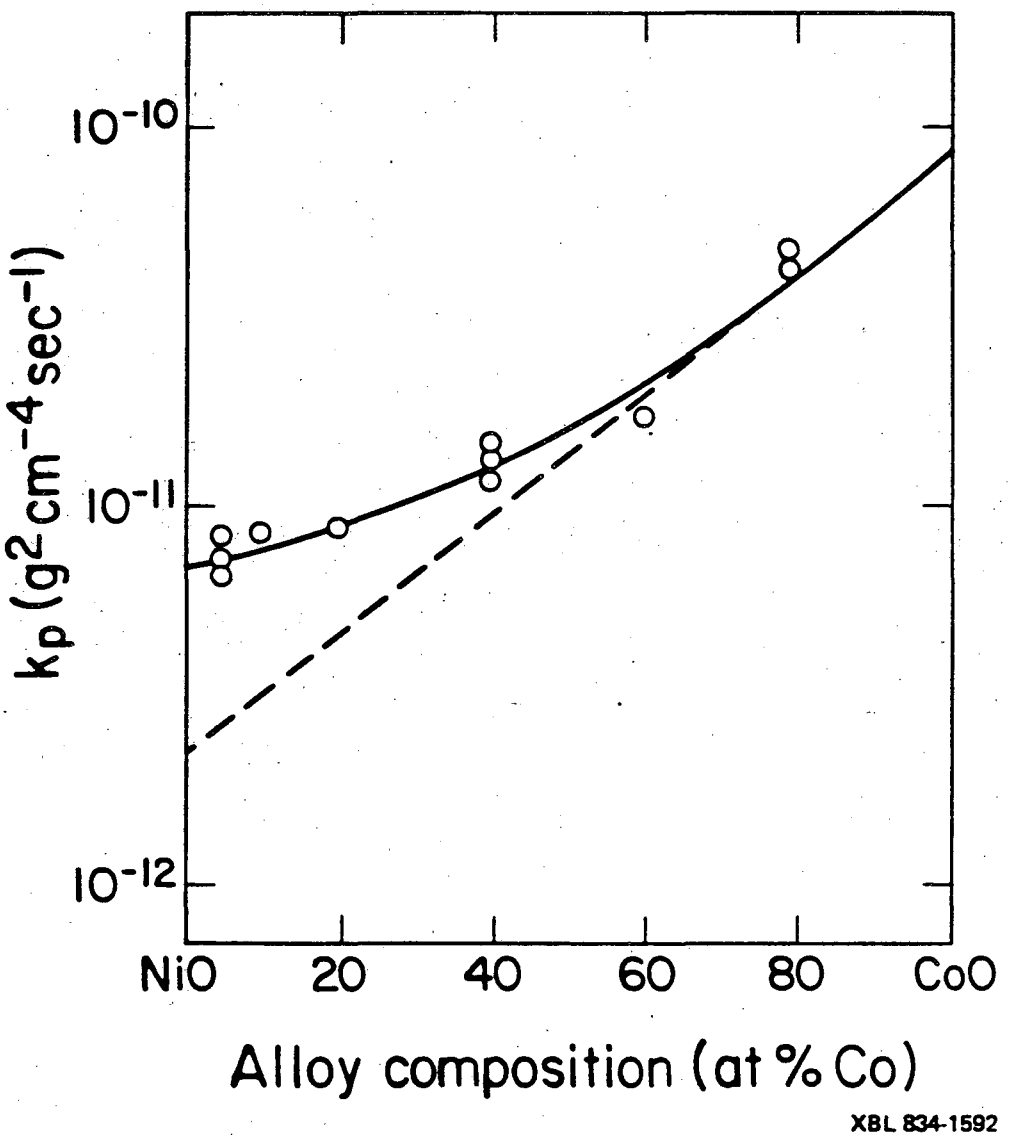

Figure 30 - Variation of the parabolic rate constant with composition for alloys oxidized at 6×10^{-9} atm. P_{O_2}. The dashed line represents the variation after the degree of Co enrichment in the scale has been corrected.

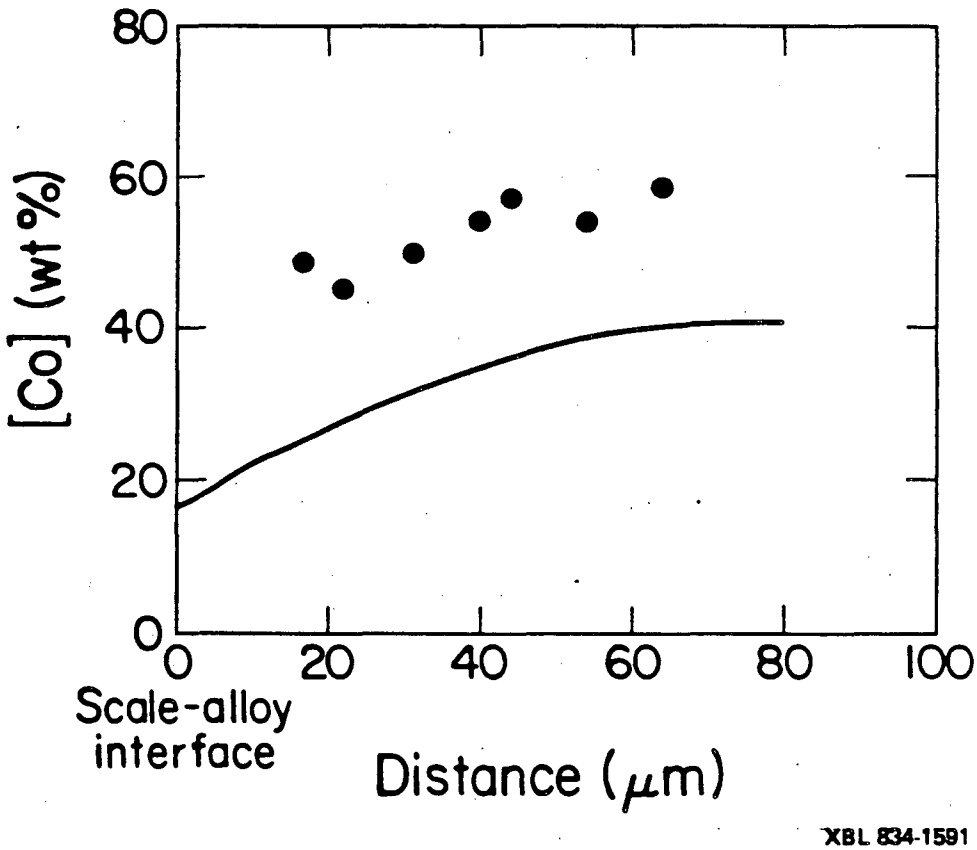

Figure 31 - Comparison between Co concentration in the alloy within the internal oxidation zone (solid line) and the Co concentration in the internal oxide precipitates (points) on a Ni-40%Co alloy oxidized at $P_{O_2}=6\times10^{-9}$ atm. for 360 hours.

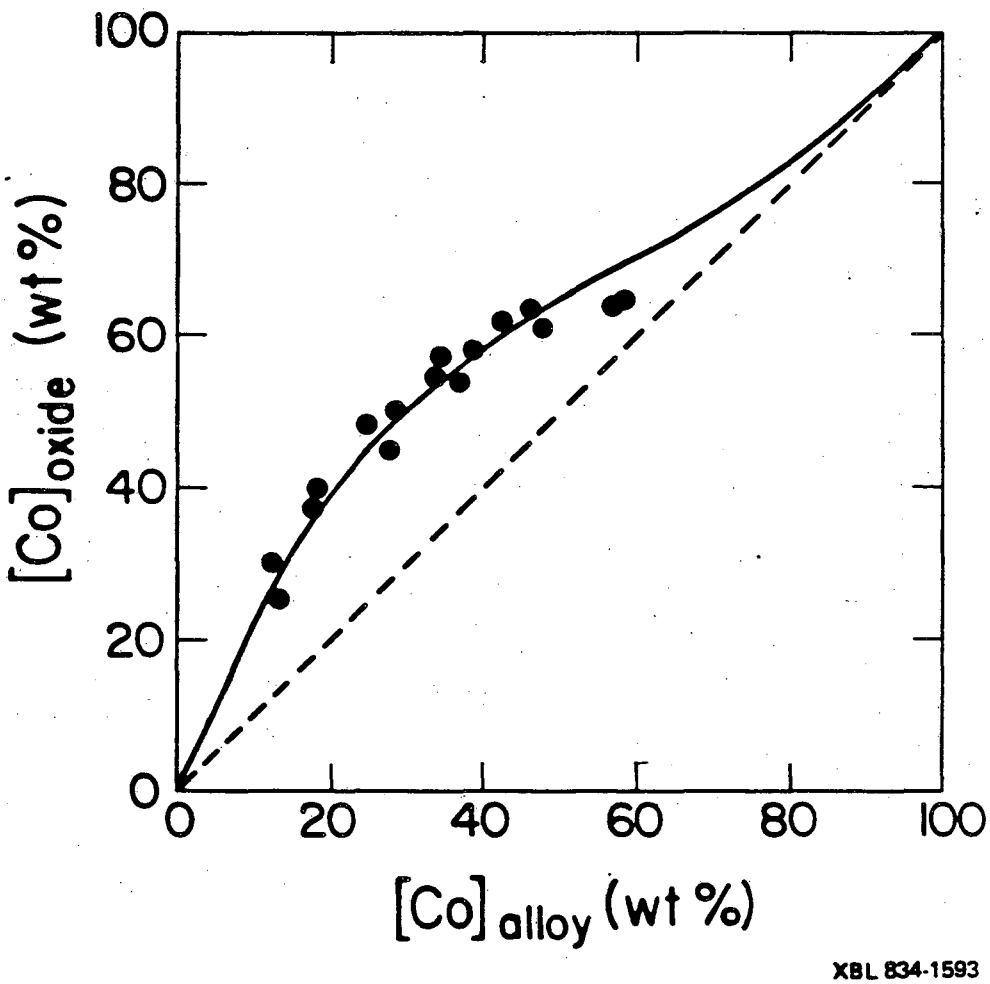

Figure 32 - Relationship between Co concentration in the internal oxides and their surrounding alloys.

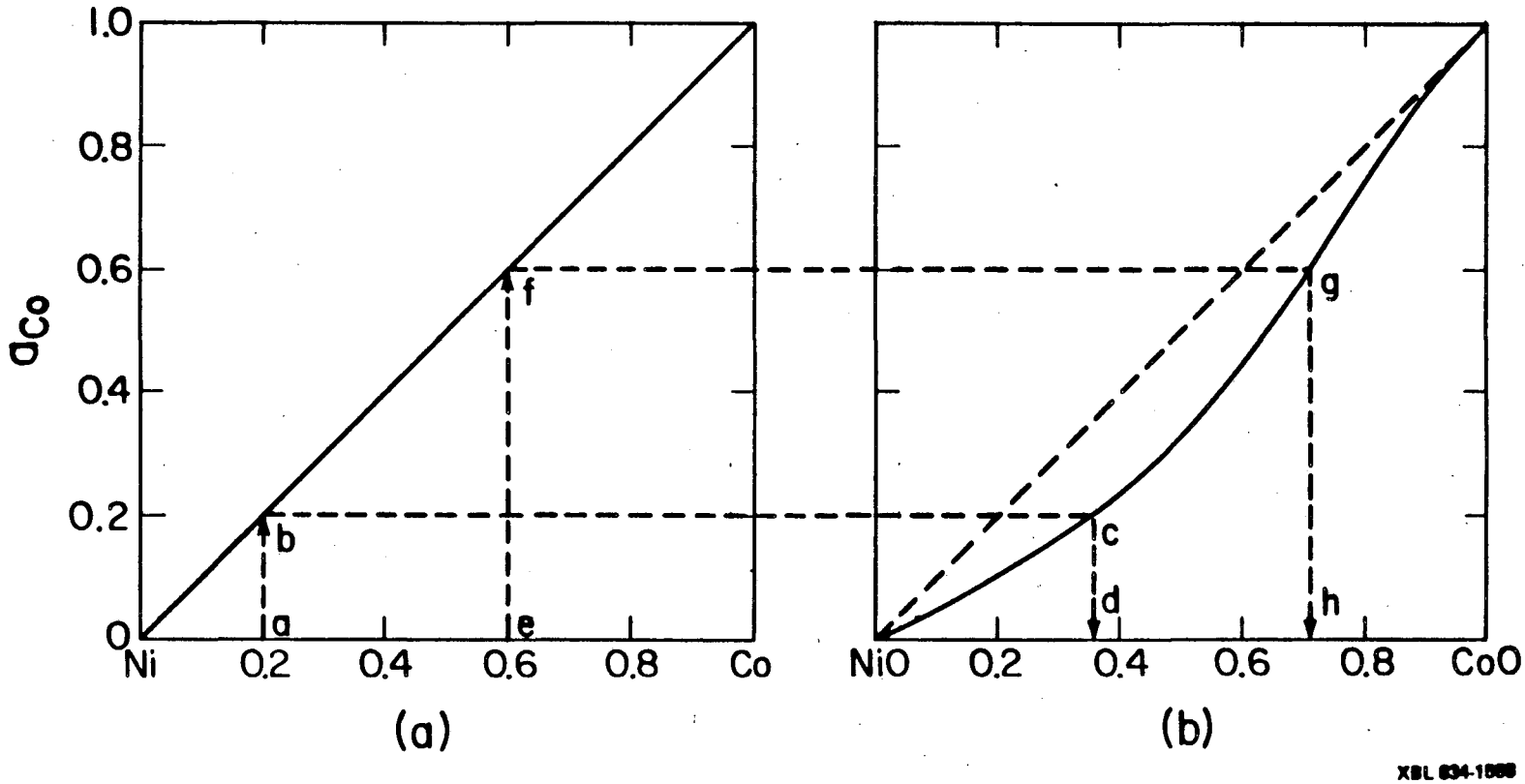

Figure 33 - Schematic illustration of the activity of cobalt in (a) the Ni-Co system and (b) the NiO-CoO system.

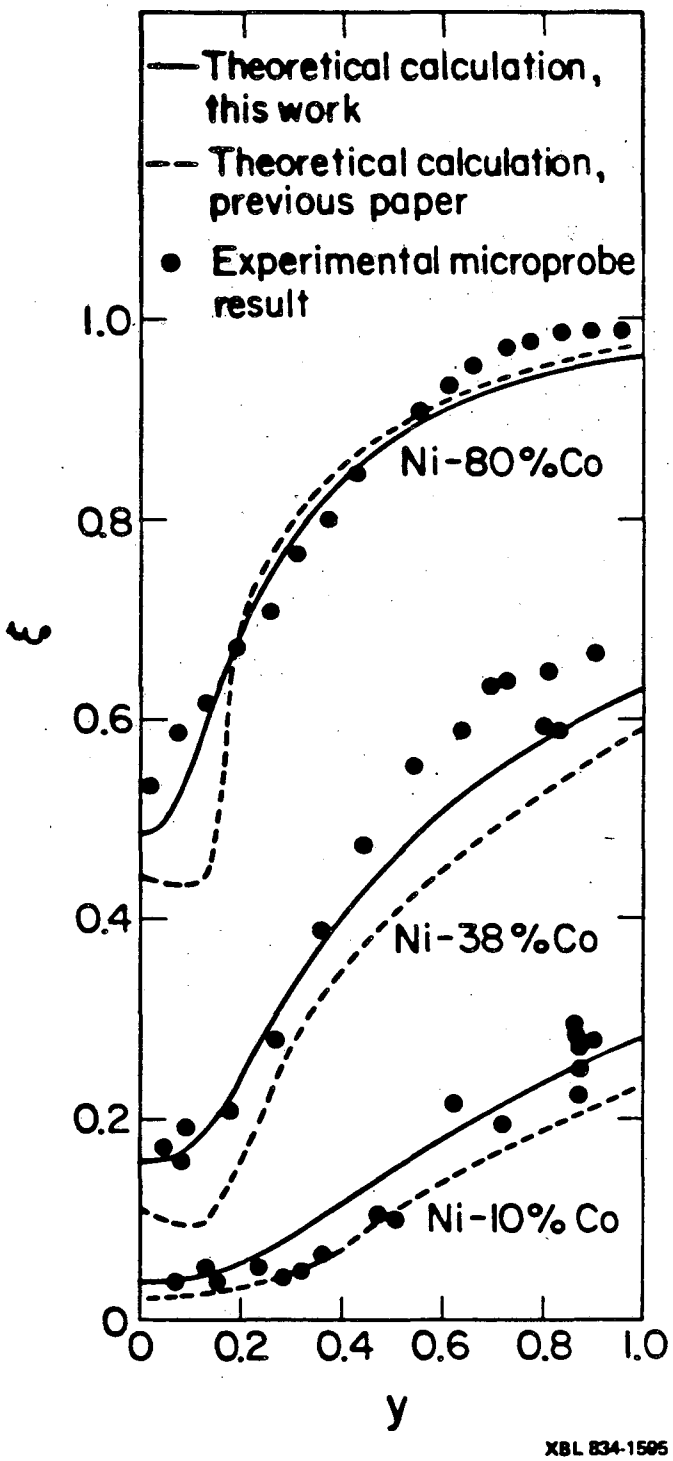

Figure 34 - A comparison between experimental cation profiles and theoretical profiles calculated in this work and in a previous paper[43] in oxide scales formed at 1000°C on Ni-Co alloys containing 10.9%, 38.4% and 80.0% Co respectively.

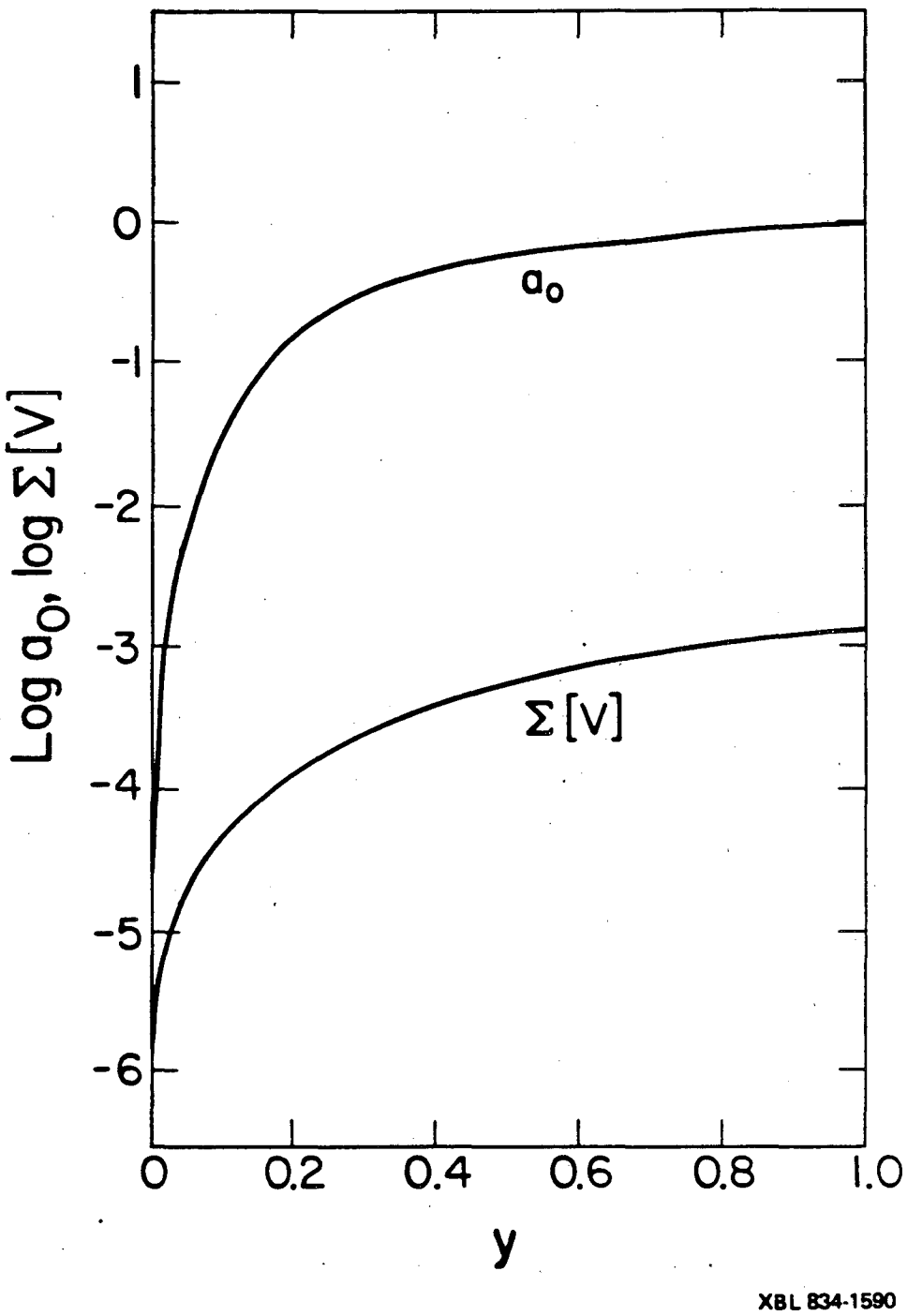

Figure 35 - Calculated oxygen activities and total vacancy concentrations across the scale formed on a Ni-38%Co alloy oxidized under 1 atm. O_2 at 1000°C.

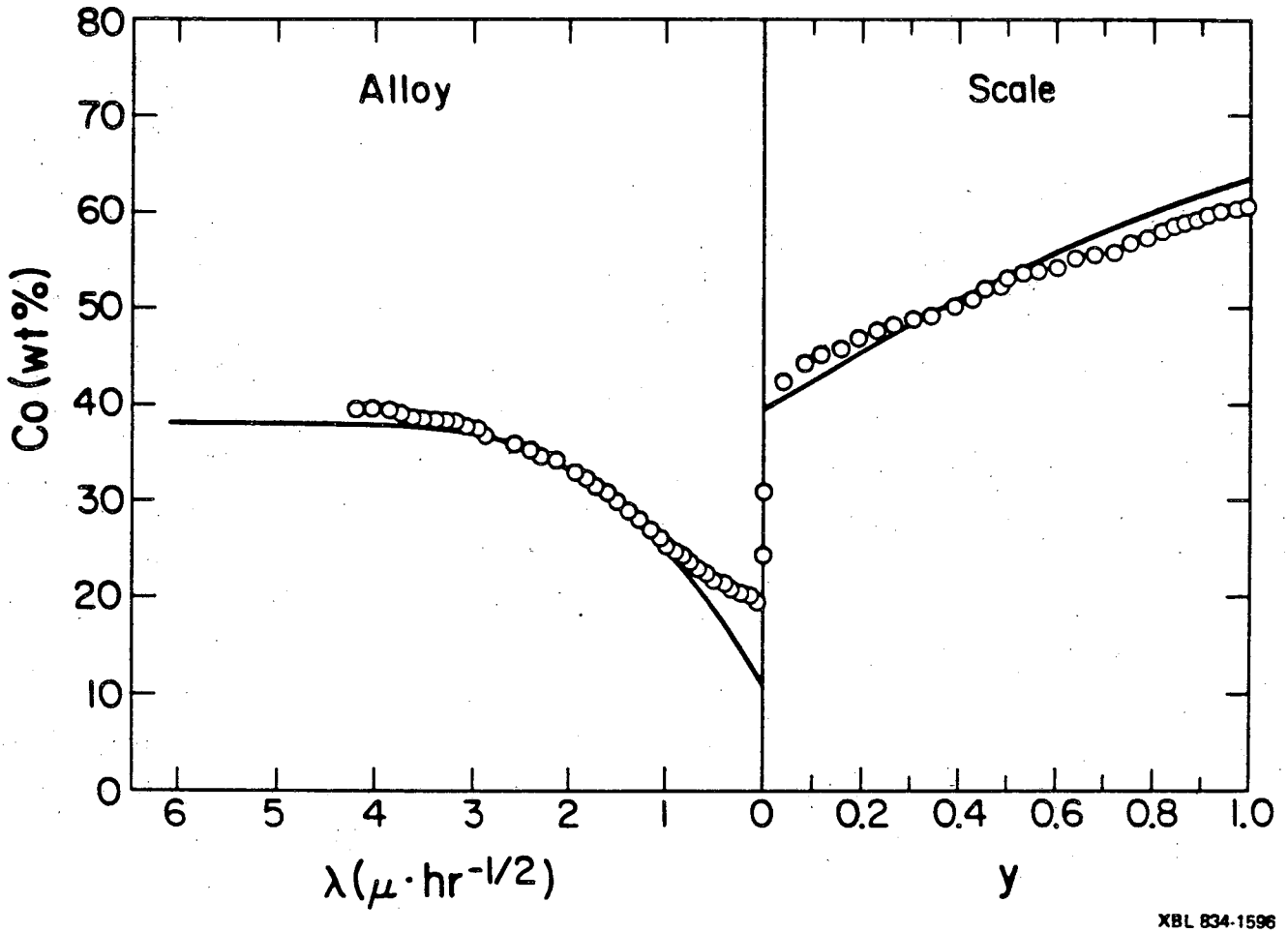

Figure 36 - Comparison between experimental and theoretical Co concentration profiles through a Ni-38%Co alloy oxidized at 6×10^{-9} atm. P_{O_2}, while allowing for the calculated oxygen activity at the scale-alloy interface to be one order of magnitude higher than its equilibrium value.

TECHNICAL INFORMATION DEPARTMENT
LAWRENCE BERKELEY LABORATORY
UNIVERSITY OF CALIFORNIA
BERKELEY, CALIFORNIA 94720